INVESTIGATION OF STRONGLY CORRELATED RUTHENATES THROUGH NEUTRON SCATTERING

विधारत्नम् महद्धनम्

Thesis submitted in partial fulfilment

for the Award of Degree

Doctor of Philosophy

by

Ekta Kushwaha

Department of Energy & Human Sciences

RAJIV GANDHI INSTITUTE OF PETROLEUM TECHNOLOGY

JAIS, INDIA - 229304

22BS0002 **2026**

CERTIFICATE

It is to certified that the work contained in the thesis titled **"Investigation of Strongly Correlated Ruthenates through Neutron Scattering"** by **Ekta Kushwaha** has been carried out under my supervision and that this work has not been submitted elsewhere for a degree.

It is further certified that the student has fulfilled all the requirements of Comprehensive, Candidacy and SOTA.

Dr. Tathamay Basu
Department of Energy and Human Sciences
Rajiv Gandhi Institute of Petroleum Technology
Jais-229304, U.P., India

DECLARATION BY THE CANDIDATE

I, **Ekta Kushwaha**, certify that the work embodied in this thesis is my own bona fide work and carried out by me under the supervision of **Dr.Tathamay Basu** from **August, 2022** to **January, 2026** at the Rajiv Gandhi Institute of Petroleum Technology, Jais, India. The matter embodied in this thesis has not been submitted for the award of any other degree. I declare that I have faithfully acknowledged and given credits to the research workers wherever their works have been cited in my work in this thesis. I further declare that I have not willfully copied any other's work, paragraphs, text, data, results, etc., reported in journals, books, magazines, reports dissertations, theses, etc., or available at websites and have not included them in this thesis and have not cited as my own work.

Date:
Place: Ekta Kushwaha

CERTIFICATE BY THE SUPERVISOR

It is certified that the above statement made by the student is correct to the best of our knowledge.

Dr. Tathamay Basu
Department of Energy and Human Science
Rajiv Gandhi Institute of Petroleum Technology
Jais-229304, U.P., India

Head of Department
Energy and Human Sciences

CERTIFICATE

CERTIFIED that the work contained in the thesis titled ***Investigation of Strongly Correlated Ruthenates through Neutron Scattering*** by **Ekta Kushwaha** has been carried out under my supervision. It is also certified that he fulfilled the mandatory requirement of TWO quality publications arose out of his thesis work.

It is further certified that the three publications (copies enclosed) of the aforesaid **Ms.Ekta Kushwaha** have been published in the Journals indexed by:

(a) SCI

(b) SCI Extended

(c) SCOPUS

Dr. Tathamay Basu
Supervisor

Dr. Omvir Singh
Convener, DPGC

COPYRIGHT TRANSFER CERTIFICATE

Title of the Thesis: Investigation of Strongly Correlated Ruthenates through Neutron Scattering
Name of the Student: Ekta Kushwaha

Copyright Transfer

The undersigned hereby assigns to the Rajiv Gandhi Institute of Petroleum Technology, Jais, India, all rights under copyright that may exist in and for the above thesis submitted for the award of the "Doctor of Philosophy".

Date:
Place: Ekta Kushwaha

Acknowledgements

The journey of completing this thesis has been both intellectually demanding and deeply transformative. As I reflect on these years, I realize that this work is far from an individual achievement it is the outcome of continuous guidance, encouragement, collaboration, and unconditional support from many people who shaped my academic and personal growth. I take this opportunity to express my heartfelt gratitude to all those who have directly or indirectly contributed to this journey.

First and foremost, I would like to express my deepest gratitude to my supervisor, Dr. Tathamay Basu, whose constant guidance, encouragement, and unwavering belief in my abilities sustained me throughout this research journey. He consistently challenged me to move beyond my comfort zone, to think more deeply, work more efficiently, and refine my ideas with greater clarity. Although I did not always fully understand these expectations at the time, reflection has shown me that each such push was essential for my growth. These experiences instilled discipline, sharpened my clarity of thought, and gave me the confidence to rise above my own limitations.

I am sincerely grateful for the opportunity to have grown academically under his mentorship. His high standards, combined with his genuine commitment to my progress, played a pivotal role in shaping my scientific maturity and in preparing me for an independent research career.

I sincerely acknowledge the Department of Energy and Human Sciences (E&HS) and my institute Rajiv Gandhi Institute of Petroleum Technology (RGIPT) for providing an intellectually stimulating and supportive academic environment throughout my doctoral studies. I express my sincere gratitude to the past and present Directors; the Deans of Academic Affairs, Research and Development, and Student Affairs; and the Heads of the Department of E&HS, Conveners and Committee members of Departmental Postgraduate Committee (DPGC) at RGIPT for their constant support. I also express my gratitude to my RPEC members Prof. Atul Sharma and Dr. Karan Malik, for their encouragement and suggestions. I sincerely thank all the faculty members of RGIPT, specially, the faculties of Physics, for their continued academic support from the first day in this 3.5 years journey at RGIPT. This work greatly benefited from collaborations and discussions with researchers across institutions. I sincerely thank Prof. Jhuma Sannigrahi (IIT Goa, India) from whom I learned the SpinW simulations. I am grateful to Dr. Antonio M. Santos (ORNL, USA) for many fruitful discussions and help in neutron diffraction experiments, and to

Dr. M. Stone (ORNL, USA) for insightful inputs on machine-learning force-field–based phonon calculations and help in INS measurements. I also thank Dr. D. T. Adroja and Dr. M. D. Lee (ISIS Facility, STFC, UK) for support during INS measurements and scientific discussions. I acknowledge CRISMAT Lab, CNRS,France and specially, Prof. V. Caignaert and Dr. W. Prellier, for fruitful collaborations. I greatly acknowledge Dr. S. D. Kaushik (UGC-DAE CSR, Mumbai, India) and Prof. M. N. Rao (BARC, Mumbai, India) for assistance in neutron diffraction and INS experiments.

I would like to thank Gourab, Mohit, and Sayan, my lab mates, for their enthusiasm, discussions, and consistent support in day-to-day research activities. Their curiosity and dedication made the lab environment lively and intellectually engaging. A special acknowledgment goes to Sayan, who has been not only a colleague but also a close friend. His constant companionship, shared discussions, and mutual encouragement made the research journey both productive and memorable, and our friendship is something I deeply value. I also like to acknowledge the undergraduate students Swarnava Bhattacharjee.

I would like to sincerely acknowledge Prof. K. K. Tiwari and Dr. Atul Gupta for their guidance during my undergraduate and postgraduate studies, which laid a strong foundation for my academic path. I am especially grateful to Ashwani Sir, Om prakash Sir and Anoop sir for always taking care of me and patiently helping me during physics practical work.

Research is not only about experiments and calculations, but also about shared experiences and collective growth. I sincerely thank my PhD friends and colleagues Saurabh Sir, Renna ma'am, Swati, Pooja, Poulami ma'am, Aditya, Alok, Saurabh sir (CBE) and Himanshu Jaiswal for their unwavering support, encouragement, and willingness to help whenever needed. Their presence made the journey lighter and more meaningful. I am deeply thankful to my roommate Shikha, who took care of me like an elder sister. Her kindness, concern, and habit of bringing food whenever I returned late made my life during PhD both easier and warmer. I would also like to thank my senior Sudeep Sir for his guidance, encouragement, and constructive discussions.

Above all, I express my deepest gratitude to my parents, whose unconditional love, sacrifices, patience, and belief in me have been the foundation of my strength and perseverance. This thesis would not have been possible without their constant support. I am equally thankful to my sister Soumya for her care, encouragement, and emotional support during difficult times. I also thank my brother Shobhit, whose quiet support and faith in me always motivated me to move forward. I acknowledge my both mama (Vinay and

Ajay) for supporting me throughout.

I extend my heartfelt appreciation to my closest friends Sandhya, Monu, Shreya, and Mohit, and to the brothers I gained during my graduation years Sachin, Shivam, Rajat Sir, and Kartikey who stood by me like family. Their presence brought joy, strength, and moments of relief from the pressures of PhD life.

Finally, I express my deepest gratitude to Sirji, who has been an unwavering pillar of strength in my life for the past ten years. His constant belief, patience, and encouragement guided me through the most challenging phases and celebrated every success with equal sincerity.

I acknowledge the national and international large-scale facilities (BARC-India, ORNL-USA, ISIS-UK, KEK-Japan) where I have performed all the high-level experiments. I also acknowledge Department of Science and Technology (DST), India and UGC-DAE CSR, India for providing me the opportunity (funding through supervisor's external project) of hands-on experience of X-ray and Neutron scattering.

At the end, I humbly thank God for giving me the strength, resilience, and guidance to walk this path, and for surrounding me with people who made this journey meaningful and fulfilling.

Ekta Kushwaha...

Dedicated To

Mumma, Papa & Somya

For their endless blessings, support, and love.

Contents

List of Symbols and Abbreviations

List of Symbols

U	On-site Coulomb interaction
W	Electronic bandwidth
J_{H}	Hund's coupling
E	Energy Transfer
$F(\lvert\mathbf{Q}\rvert)$	Magnetic form factor
$\lvert\mathbf{Q}\rvert$	Momentum Transfer
T_{N}	Néel temperature
T_{P}	Peak temperature
T_{C}	Curie temperature
$\mathbf{k}$	Magnetic propagation vector
J_{ij}	Exchange interaction between spins at sites i and j
θ_{CW}	Curie–Weiss temperature
D	Anisotropy constant
ε'	Real part of dielectric constant
ε''	Imaginary part of dielectric constant
ν	Frequency

E_a	Activation energy
χ'	Real part of magnetic susceptibility
χ''	Imaginary part of magnetic susceptibility
$M(H)$	Isothermal magnetization
G	Gibbs free energy
V	Lattice volume
ω	Raman shift
ω_0	Uncoupled phonon frequency
ω_ph	Phonon frequency

List of Abbreviations

TMOs	Transition Metal Oxides
CEF	Crystal Electric Field
SOC	Spin-Orbit Coupling
D-M	Dzyaloshinskii-Moriya Interaction
XRD	X-ray Diffraction
HRXRD	High-Resolution X-ray Diffraction
NPD	Neutron Powder Diffraction
TOF	Time-of-Flight
INS	Inelastic Neutron Scattering
MLFF	Machine Learning Force Field
DFT	Density Functional Theory
CIF	Crystallographic Information File
ME	Magnetoelectric

MDE	Magnetodielectric
PUND	Positive-Up-Negative-Down
ZFC	Zero-Field-Cooled
FC	Field-Cooled
PPMS	Physical Property Measurement System
SQUID	Superconducting Quantum Interference Device
SEM	Scanning Electron Microscopy
EDS	Energy Dispersive X-ray Spectroscopy
HAADF-STEM	High-Angle Annular Dark-Field Scanning Transmission Electron Microscopy
XPS	X-ray Photoelectron Spectroscopy

List of Figures

List of Tables

Abstract

The study of strongly correlated electron systems is in current focus in the field of condensed matter physics, in particular, $4d/5d$-transition-metal oxides, where strong spin-orbit coupling (SOC), electron-electron coulomb repulsion, and large crystal-electric-field (CEF) effects compete with each other and exhibit a versatile exotic ground state. Among them the ruthenates represent a unique platform to explore emergent phenomena such as spin frustration, superconductivity, metal-insulator transition, magnetoelectric coupling. While the intrinsic physics of ruthenates alone is remarkably rich, incorporating the rare-earth elements introduces additional $4f$ moments that couple with Ru($4d$) electrons. This d-f coupling can further tune the magnetic ground state, controlling the functional properties of the systems. However, the research on ruthenates ($4d$) and especially $4d$-$4f$ systems is limited.

The thesis work is focused on unraveling the interplay between crystal and magnetic structure, spin dynamics, and electronic correlations in Ru-based oxides, focusing on the trimer compound $Ba_5Ru_3O_{12}$ and the $4d$-$4f$ coupled perovskite series $Ba_3RRu_2O_9$ (R = Ho, Tb, Sm). The high-level microscopic techniques, such as, high-resolution synchrotron X-ray diffraction, time-of-flight neutron diffraction, and inelastic neutron scattering (INS) experiments were carried out together with spin-wave simulations and theoretical calculations to study the magnetic structure, exchange interactions, spin excitations, and the nature of the unconventional ground states.

This thesis explores the unique magnetic ground state of $Ba_5Ru_3O_{12}$, which consists of isolated Ru_3O_{12} trimers. Inelastic neutron scattering measurements, spin-wave simulation and machine-learned force field calculation reveal complex and competing magnetic exchange interactions, strong electronic correlations, magnetic anisotropy, and possible spin-phonon coupling in this system. These results shows that how ruthenium-based systems host diverse emergent phenomena and explains how their ground state (and thus physical properties) can be tuned by structural motifs.

The role of $4d$-$4f$ coupling is also explored in this thesis work. A key result of this work is the experimental demonstration of spin-driven ferroelectricity in $Ba_3HoRu_2O_9$, that originates from inverse Dzyaloshinskii-Moriya (D-M) interactions between magnetic moments originated from two non-equivalent magnetic atoms, that is, Ru ($4d$) and Ho ($4f$). This result shows that strong $4d$-$4f$ coupling alone can break inversion symmetry and induce ferroelectric polarization, providing a new microscopic pathway to multiferroicity. The compound $Ba_3TbRu_2O_9$ exhibits an unconventional Tb^{4+} valence state with a spin-only configuration and a highly unusual cooperative Ru-Tb magnetic ordering which is different from other rare-earth members of the same family. Furthermore, temperature-dependent structural studies on $Ba_3SmRu_2O_9$ uncover a symmetry-lowering structural transition at low temperatures, likely associated with lattice instabilities, underscoring the sensitivity of Ru-based systems to rare-earth chemistry.

Chapter 1: Introduction

This chapter provides the fundamental background required to understand the physics explored in this thesis. It introduces the concept of strongly correlated electron systems, emphasizing why conventional band theory fails when electron-electron interactions become comparable to the electronic bandwidth. The discussion highlights transition-metal oxides, where the interplay of Coulomb interaction, bandwidth, Hund's coupling, crystal-field effects, and spin-orbit coupling gives rise to unconventional ground states.

We have provided a brief overview of past literature and discussed the research on $3d$, $4d$ and $5d$ transition-metal oxides, explaining how increased orbital and spin-orbit coupling modify electronic correlations. Considering this, ruthenium-based oxides are identified as ideal systems lying in an intermediate-correlation regime. In this chapter we have briefly discusses the motivation of choosing ruthenates, their historical background, $4d$-$4f$ coupling, and sets the conceptual foundation for exploring their complex magnetic, dynamical, and magnetoelectric properties in later chapters.

Chapter 2: Experimental Techniques and Methodology

This chapter describes the experimental methods and analysis techniques which are employed throughout the thesis. The details of sample preparation, and their structural characterization through powder X-ray diffraction using Rietveld refinement method have been discussed.

The chapter provides a detailed explanation of neutron scattering techniques, highlighting their importance in probing both crystal and magnetic structures as well as spin dynamics. Powder neutron diffraction is discussed as a key tool for determining magnetic ordering, while inelastic neutron scattering (INS) is introduced as a powerful technique to study magnetic excitations and spin-wave spectra.

The principles of data analysis, including Rietveld refinement, representation analysis for magnetic structures, and spin-wave modeling using SpinW software, are explained. The machine-learning framework used to produce the phonon spectra has been discussed.

This chapter establishes the technical backbone of the thesis and ensures that the experimental results presented in later chapters are well-grounded and reproducible.

Chapter 3: Interplay between trimer structure and magnetic ground state in $Ba_5Ru_3O_{12}$ probed by Inelastic Neutron Scattering, spin-wave theory and Machine-learning framework

This chapter focuses on the investigation of $Ba_5Ru_3O_{12}$ system, where inelastic neutron scattering revealed spin-wave excitations and magnon-phonon coupling, indicative of competing exchange interactions, spin frustration, and magnetic anisotropy. The detailed nearest and next-nearest magnetic exchange interactions are estimated through SpinW (MATLAB) simulation on experimental INS spectra, maintaining the non-colinear spin structure consistent with the experiment. Our combined theoretical calculations and experimental spectra have interpreted the spin-excitation and depicted the ground state of the Ru-trimer.

In this chapter, the magnetic ground state and spin dynamics of the trimer ruthenate $Ba_5Ru_3O_{12}$ are investigated using inelastic neutron scattering (INS) techniques. This compound exhibits long-range antiferromagnetic ordering below $T_N = 60$ K. INS data analysis along with SpinW simulations and machine-learned force-field calculations suggest that this system hosts a frustrated magnetic ground state, which arises from competing nearest- and next-nearest-neighbor exchange interactions, exchange anisotropy, and strong spin-orbit coupling, which together stabilize a non-collinear spin structure. This

behavior is markedly different from other ruthenate trimer systems that typically exhibit collinear magnetism. μSR measurements further support this by revealing a gradual loss of initial asymmetry across the magnetic transition, consistent with dynamic magnetic behavior. The μSR results indicate that the magnetic order remains partially dynamic due to local anisotropy arising from structural distortions and varying hybridization within the Ru_3O_{12} trimer.

Chapter 4: Ground state of 6H perovskite $Ba_3HoRu_2O_9$, Origin of spin-driven ferroelectricity, spin and CEF excitations

In this chapter, the magnetic and multiferroic properties of the 6H-perovskite compound $Ba_3HoRu_2O_9$ are investigated. The compound undergoes magnetic ordering at $T_{N1} = 50$ K, followed by a second and more complex magnetic phase transition at $T_{N2} = 10.2$ K. The low-temperature phase is characterized by the coexistence of two competing magnetic ground states associated with different propagation vectors, K_1 (0.5 0 0) and K_2 (0.25 0.25 0).

We studied this system using time-of-flight neutron diffraction with large Q-range, high-resolution synchrotron X-ray diffraction, AC susceptibility, frequency-dependent dielectric spectroscopy, and DC magnetization under external pressure. This chapter presents the mechanism of spin-driven ferroelectricity in the $Ba_3HoRu_2O_9$ system. Our results demonstrate that the non-collinear magnetic structure involving both Ru($4d$) and Ho($4f$) moments breaks spatial inversion symmetry through an inverse Dzyaloshinskii-Moriya interaction driven by strong $4d$-$4f$ magnetic correlations. This interaction induces shifts of oxygen atoms, leading to a finite electric polarization. Such spin-driven ferroelectricity arising from inverse D-M interaction between two different magnetic ions is rare and highlights the important role of enhanced spin-orbit coupling associated with the $4d$ orbitals. A careful analysis of the peak-shape of Bragg diffraction using time-of-flight Neutron diffraction reveals that the second magnetic phase associated with K_2 exhibits a shorter coherence length, indicating the formation of magnetoelectric domains rather than true long-range ferroelectric order. This explains the earlier report of experimentally observed low value of ferroelectric polarization. Temperature-dependent synchrotron X-ray diffraction shows a clear anomaly in lattice parameters and unit-cell volume at T_{N2}, consistent with a ferroelectric transition and suggesting a non-centrosymmetric $P6\bar{2}c$ space group.

Furthermore, external pressure is found to enhance the magnetic ordering temperature, indicating that pressure stabilizes the magnetic ground state associated with the second magnetic phase.

Further, the magnetic and lattice excitations of the multiferroic 6H-perovskite $Ba_3HoRu_2O_9$ are investigated using high-level inelastic neutron scattering, Raman spectroscopy, spin-wave modeling, and machine-learned force-field phonon calculations.

Inelastic neutron scattering reveals a broad low-energy magnetic excitation that appears only below T_{N2}. Spin-wave analysis shows that this excitation corresponds to a collective magnon mode stabilized by strong antiferromagnetic Ru-Ru intradimer exchange together with significant Ru-Ho coupling, indicating that the low-energy dynamics cannot be described by isolated Ru_2O_9 dimers alone. At higher energies, several excitations are observed. In which excitations near 12 meV and 40 meV are attributed to crystal electric field excitations of Ho^{3+} ions.

Machine-learned force-field phonon calculations performed on this system reveal overlap between phonon modes and Ho^{3+} crystal-field energies, confirming the presence of crystal-field-phonon coupling. These results highlight strong spin-orbit-entangled $4d$-$4f$ lattice interactions in $Ba_3HoRu_2O_9$ and establish this system as a suitable platform for studying hybrid magnetic and lattice excitations in correlated multiferroic materials.

Chapter 5: Magnetic structure, cooperative Ru($4d$)-Tb($4f$) spin-ordering and unconventional S-orbital state of Tb in $Ba_3TbRu_2O_9$

This chapter focuses on $Ba_3TbRu_2O_9$. Our combined bulk and microscopic studies show that Tb^{4+} adopts a spin-only electronic configuration with $S = 7/2$ and a quenched orbital moment ($L = 0$), while Ru^{4+} also exhibits a spin-only magnetic moment with $S = 1$, despite the presence of strong spin-lattice coupling.

A cooperative magnetic ordering of Ru($4d$) and Tb($4f$) moments is observed below the Néel temperature $T_N = 9.5$ K, indicating strong Ru-Tb correlations. The Tb moments order antiferromagnetically within the *bc*-plane, whereas the Ru moments align antiferromagnetically along the *b*-axis. In contrast to other related compounds such as the Ho- and Nd-based members, the Ru_2O_9 dimers in $Ba_3TbRu_2O_9$ exhibit a collinear antiferromagnetic spin arrangement throughout the structure.

Chapter 6: Investigation of temperature dependent crystal and magnetic structure of $Ba_3SmRu_2O_9$

In this chapter, the structural and magnetic properties of $Ba_3SmRu_2O_9$ are examined using temperature-dependent synchrotrons XRD and ND. Temperature-dependent synchrotron XRD data of $Ba_3SmRu_2O_9$ suggest lowering symmetry from a hexagonal structure ($P6_3/mmc$) to a monoclinic structure ($C2/c$ space group, which further reduced to $P2/c$ space group) below 80 K, which can be due to presence of Jahn-Teller distortion that influences the Ru-O-Ru bond angles. We have carried out neutron diffraction on this magnetic system. The results reveal the possible spin-structure and suggest a very small magnetic moment of Sm.

Outcome Of the thesis

This thesis provides a comprehensive understanding of magnetism, spin dynamics, and spin-phonon coupling in strongly correlated ruthenium-based oxides, with particular emphasis on dimer and trimer ruthenates and Ru($4d$)-R($4f$) coupled systems (R = rare-earth).

The main outcomes of this thesis are summarized as follows:

- We established the existence of cooperative $4d$-$4f$ magnetic ordering in heavy rare-earth members of the $Ba_3RRu_2O_9$ family (R = Ho and Tb), demonstrating a rare and robust interplay between itinerant Ru($4d$) and localized rare-earth $4f$ moments.
- We provided the experimental demonstration of spin-driven ferroelectricity in $Ba_3RRu_2O_9$, that originates from inverse Dzyaloshinskii-Moriya interactions between Ru ($4d$) and Ho ($4f$) magnetic moments, unlike only from spin-pattern of transition metal ions-a phenomenon rarely reported. This results further provide a pathway to study $4d$-$4f$ systems from magnetoelectric aspects.
- We also show that external pressure can act as a very effective control parameter for magnetic ground-state and proved that pressure can induce stable competing phases and can also enhance magnetic ordering temperatures in $4d$-$4f$ coupled systems.
- Our investigations on trimer ruthenate systems demonstrate a complex magnetic ground state of $Ba_5Ru_3O_{12}$ compared to that of other nearly isostructural ruthen-

ate trimer. The investigation reveals that small structural change in same family can produce versatile magnetic ground state due to different degrees of hybridizations, which cause verities of physical properties, such as metal-insulator transitions, metal-metal bonding similar to molecular hybridizations.

- We have explored and validated a machine-learned force-field framework that successfully reproduces experimentally measured INS phonon spectra. This represents a significant methodological advance and provides a new route for exploring lattice dynamics in complex correlated materials. This work will further motivate in exploring the various properties in materials employing machine-learning approaches.

Chapter 1

INTRODUCTION

1.1 Strongly Correlated Electron Systems- General Background

In most traditional models of solids, the kinetic energy of electrons in a periodic crystal potential is considered to be the dominant contribution while electron-electron interactions are treated as a secondary effect. On the basis of that theoretical descriptions of the free-electron theory, band theory, and Landau's Fermi-liquid theory have been developed. These approaches are well suited for simple metals and semiconductors, where coulomb interactions are efficiently damped by mobile charge carriers. In such systems, the low-energy excitations behave like well-defined quasiparticles with long lifetimes [1]. However,

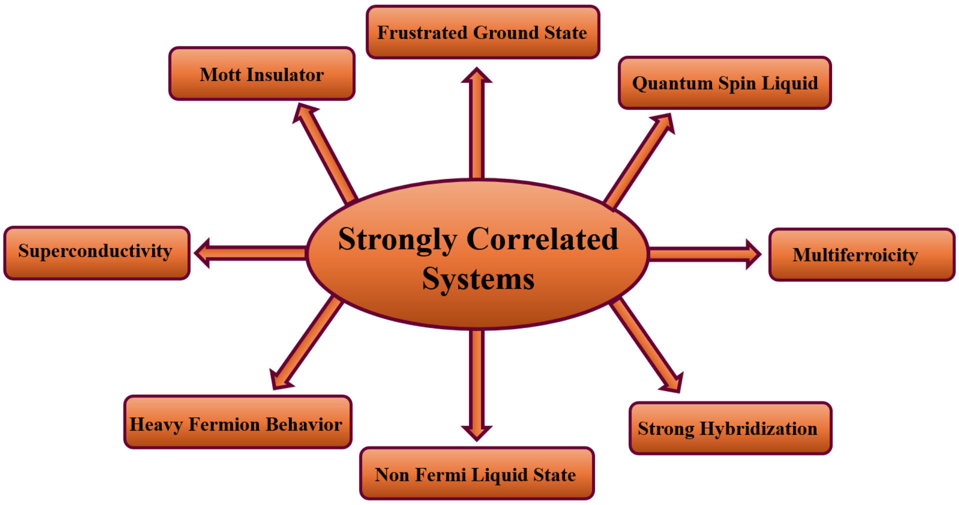

Figure 1.1: Overview of emergent phases in strongly correlated electron systems

this independent-particle approach, is no longer valid when interaction energy scales are comparable to the electronic bandwidth. In many transition-metal compounds, the on-site coulomb repulsion U, bandwidth W, and Hund's coupling J_H are of similar magnitude. When $U \sim W$, electron motion is strongly constrained by correlations, and the electronic structure can no longer be described in terms of weakly renormalized bands. Materials in this regime are referred to as strongly correlated electron systems [2, 3].The broad range of unconventional ground states that emerge when electron-electron interactions dominate, including Mott insulating behavior, unconventional superconductivity, multiferroicity, and quantum spin liquids, is summarized schematically in Fig. 1.1.

A clear consequence of strong correlations is the failure of conventional band theory to predict the correct ground state. According to conventional band theory, a material with a partially filled band should always be metallic. Contrary to this prediction, many transition metal oxides (TMOs) are insulating despite having an odd number of electrons per unit cell. Mott demonstrated that strong on-site coulomb repulsion can localize electrons and drive an interaction-induced insulating state, now referred to as a Mott insulator [4, 5]. This insight established electronic correlations as a central concept in solid-state physics. To describe the fundamental physics of correlated electrons, Hubbard introduced a minimal microscopic model that balances electron hopping with on-site coulomb repulsion [6]. Although the Hubbard model is conceptually simple, it has not been solved exactly in more than one dimension and has become a central framework for understanding strongly correlated electron systems. In this simplified form, it exhibits a wide range of emergent phenomena such as metal-insulator transitions, and deviations from conventional Fermi-liquid behavior that highlight the inherent complexity of interacting many-electron systems. Further insight into the limitations of weakly correlated theories comes from studies of magnetic impurities and heavy-fermion materials, where strong electron-electron interactions lead to collective behavior that cannot be explained within simple band-like descriptions. The Kondo effect leads to many-body singlet formation between localized moments and conduction electrons, causing anomalous low-temperature behavior [7, 8]. In heavy-fermion compounds, a lattice of such moments produces quasiparticles with strongly enhanced effective masses [9], showing how strong correlations can drastically alter the behavior of a metallic system. The discovery of high-temperature superconductivity in copper-oxide materials further emphasized the crucial role of strong electron correlations [10]. The rich and complex phase diagrams of these systems, marked by competing magnetic and electronic phases, clearly demonstrate that electron -electron interactions play a dominant role in determining their physical properties. This perspective forms the essential background for the studies presented in this thesis.

1.2 Strongly Correlated Transition Metal Oxides

TMOs are one of the most widely studied strongly correlated materials because of the extraordinary diversity of their physical and chemical properties. Their structural and chemical complexity can be readily tuned by varying composition, crystal structure, or external parameters such as temperature, pressure, strain, and applied fields which makes them ideal for exploring correlation-driven phenomena [2]. As a result, TMOs exhibit a wide range of emergent phenomena, including superconductivity, multiferrocity, metal-insulator transitions, unconventional magnetic ground state and complex excitation spectra [9, 11, 12, 13, 14, 15]. In these materials, transition metal ions are typically coordinated by oxygen ligands and most commonly form octahedral or tetrahedral environments. The electrostatic potential generated by the surrounding oxygen ions lifts the degeneracy of the atomic d orbitals through crystal-field splitting as shown in Fig. 1.2(a) [16]. In an octahedral environment, this splitting separates the d states into lower-energy t_{2g} and

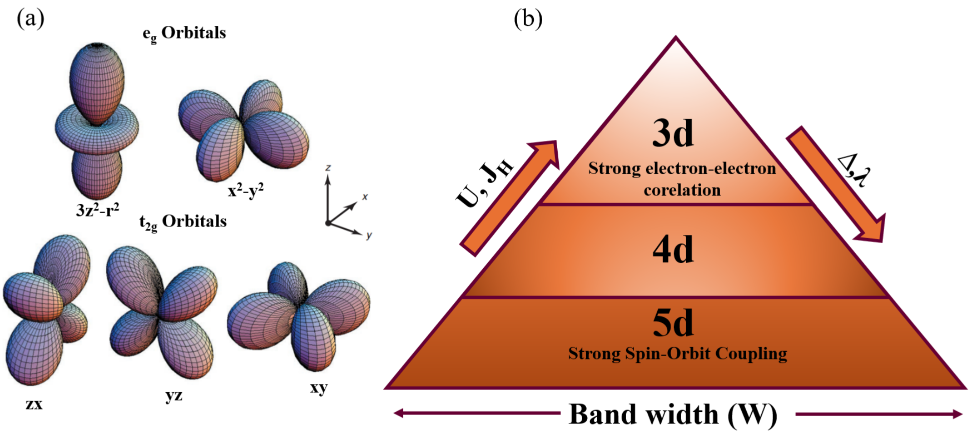

Figure 1.2: (a) Crystal-field splitting of $4d$ orbitals into t_{2g} and e_g manifolds in an octahedral environment. (b) Schematic comparison of $3d$, $4d$, and $5d$ transition-metal oxides in terms of key energy scales. From $3d$ to $5d$ systems, the bandwidth W increases, while the relative strengths of the coulomb interaction U, Hund's coupling J_H, and SOC λ evolve. As a result, $4d$ systems such as ruthenates occupy an intermediate regime where these interactions are comparable.

higher-energy e_g manifolds, with the exact energy hierarchy depending on local symmetry and distortions [17, 18, 19]. Crystal-field effects (CEF) play a central role in determining orbital occupancy, magnetic moment formation, and the low-energy electronic structure of these compounds [18, 19]. Because the bandwidth varies from p-d hybridization is often comparable to the on-site coulomb repulsion U, many TMOs lie near the boundary between itinerant and localized electronic behavior. This delicate balance explains why small perturbations can drive dramatic changes, such as metal-insulator transitions or switches between different magnetic ground states.

Magnetism in TMOs naturally emerges from partially filled d shells in the presence of strong coulomb interactions. Local magnetic moments form on transition metal sites, while superexchange interactions mediated by oxygen ions couple these moments across the lattice [17, 20]. Although TMOs share common structural motifs, their electronic and magnetic properties evolve systematically across the $3d$, $4d$, and $5d$ series due to changes in the radial extent of the d orbitals and the relative strength of key energy scales.

In $3d$ TMOs, such as compounds based on vanadium, manganese, or copper, the d orbitals are relatively localized due to their smaller spatial extent. This leads to narrow electronic bandwidths and strong coulomb repulsion. As a result, many $3d$ oxides are well described as Mott insulators, characterized by robust local magnetic moments and strong antiferromagnetic superexchange interactions [17, 20, 21]. This strong tendency toward local-moment magnetism also provides the microscopic foundation for spin driven ferroelectricity in several $3d$-based multiferroic oxides. In well-known systems such as $RMnO_3$ and RMn_2O_5 (where R is a rare-earth ion), electric polarization originates directly from the magnetic ordering of the $3d$ transition-metal sublattice [22, 23, 24, 25, 26, 27, 28, 29, 30, 31]. Depending on the magnetic structure, polarization is generated either by non-collinear (canted) spin configurations through the inverse Dzyaloshinskii-Moriya (D-M) interaction, or by collinear spin arrangements via the exchange-striction mechanism, illustrating the coupling between magnetism and ferroelectricity in strongly correlated $3d$ oxides [11, 32, 33]. In contrast, $4d$ TMOs possess more spatially extended d orbitals, which enhance orbital overlap and result in broader electronic bands. As a result, many 4d oxides exhibit correlated metallic behavior rather than conventional Mott insulating states [3, 34]. Hund's coupling further enhances correlation effects in many $4d$ systems. It suppresses inter-orbital charge fluctuations and lowers the coherence scale of itinerant electrons, giving rise to strongly correlated metallic states even when the on-site coulomb interaction alone is insufficient to localize electrons

[3]. This mechanism distinguishes many 4d oxides from both the strongly localized 3d systems and the more relativistic 5d compounds. In 5d TMOs, the d orbitals are even more spatially extended, leading to large bandwidths and relatively weaker coulomb interactions. However, in the case of 5d elements, its heavier atomic mass yields strong spin-orbit coupling (SOC), which may become comparable or even exceed crystal-field splitting and exchange interactions [2, 35]. Such strong SOC entangles spin and orbital degrees of freedom and thus stabilizes novel relativistic electronic and magnetic states. Iridates such as $\mathrm{Sr_2IrO_4}$ are well-known examples of this class of materials [35]. The systematic evolution of the key energy scales across the 3d, 4d, and 5d transition-metal series are illustrated in Fig. 1.2(b). Considering this, 4d transition-metal oxides occupy a unique intermediate position between the localized-electron physics of 3d compounds and the spin-orbit-dominated behavior of 5d systems. In these materials, the energy scales U, W, J_H and λ are often comparable, making their electronic and magnetic properties highly sensitive to lattice distortions, pressure, and chemical substitution. As a result, relatively small perturbations can induce significant changes in physical behavior.

In this context we can say ruthenium-based oxides represent a particularly important class of 4d materials by providing a fertile ground for studying unconventional correlated states.

1.3 Ruthenium-Based Oxides:Motivation and Background

Ruthenium-based oxides occupy a distinctive position among correlated electron materials. Unlike many 3d oxides, they are not well described by purely localized spin models, yet they also deviate strongly from weakly correlated itinerant metals. Instead, ruthenates reside in an intermediate regime where electronic correlations, orbital degrees of freedom, and lattice effects must all be considered on an equal footing. This intermediate characteristic of ruthenium-based oxides make it an ideal for investigating correlated electronic states that evolve between localized and itinerant limits. In particular, the interplay between oxidation state, Hund's coupling, orbital physics, and crystal structure provides a natural setting for the emergence of unconventional magnetic states, cluster-based magnetism, and strongly renormalized metallic behavior, which forms the central focus of the present thesis.

1.3.1 Role of Ru Oxidation States and Electronic Configurations

The physical properties of ruthenium oxides can change substantially even with small variations in electronic structure. As a result, compounds that are structurally very similar may exhibit very different properties ranging from correlated metallic states to insulating and magnetically ordered phases. This complexity arises primarily from the ability of ruthenium to stabilize multiple oxidation states in oxides, most commonly Ru^{3+} ($4d^5$), Ru^{4+} ($4d^4$), and Ru^{5+} ($4d^3$). Each electronic configuration leads to distinct orbital filling, correlation strength, and magnetic ground state that make ruthenates an ideal platform for systematically exploring how electronic degrees of freedom evolve across different regimes.

1.3.2 Historical Perspective

Early research on ruthenium oxides began with simple binary compounds like RuO_2, which were long regarded as conventional itinerant metals exhibiting Pauli paramagnetism and well-defined Fermi surfaces. These observations led to the early perception that Ru $4d$ electrons favor delocalized, weakly correlated behavior.One of the characteristic features of ruthenium oxides is that their physical properties are sensitive to even a small change in chemical structure. Even compounds with closely related crystal structures can exhibit very different behavior, ranging from correlated metallic states to insulating and magnetically ordered phases. Due to this sensitive nature, ruthenates form a suitable platform for studying correlation-driven phenomena. This view was reinforced by studies on perovskite ruthenates such as $SrRuO_3$ and $CaRuO_3$, which display metallic conductivity along with itinerant ferromagnetism or strong paramagnetic fluctuations [34]. However, experimental and theoretical work suggest that these systems show substantial mass renormalization and strongly enhanced electronic correlations, ruling out the description of ruthenium oxides as conventional band metals. The discovery of unconventional superconductivity in Sr_2RuO_4 further highlighted the importance of spin fluctuations, orbital-selective correlations, and enhanced SOC in ruthenates [14, 15]. Sr_2RuO_4 showed that strong dynamical correlations can be significant even in the absence of long-range magnetic order, which motivated the study of a broader class of ruthenium-based oxides with different crystal structures and magnetic properties [14, 15]. This sensitivity is well illustrated by systems such as Ca_2RO_4, which is a Mott insulator at low temperature but undergoes a structural transition that strongly reduces the insulating gap and pushes the system toward metallic behavior [36]. Such structure-controlled electronic transitions are a recurring feature in ruthenates [37]. Even richer physics emerges in rare-earth ruthenates, where Ru 4d electrons interact with localized 4f moments. In the pyrochlore compounds $R_2Ru_2O_7$ (R = Dy, Ho, Tb, etc.), the Ru sublattice orders magnetically at relatively high temperatures, producing a strong internal field that acts on the rare-earth ions [38, 39, 40, 41, 41, 42, 43, 44]. This interaction modifies the crystal-field states of the 4f moments and suppresses or alters the spin-ice and spin-liquid behavior typical of rare-earth pyrochlores. For example, in $Ho_2Ru_2O_7$ the Ru-Ho exchange leads to an unusual partially ordered Ho state, highlighting the importance of 4d-4f coupling [38, 39].

A similar interplay is found in the double-perovskite ruthenates Ba_2LnRuO_6, where both the alkaline-earth ion A and the rare-earth ion Ln strongly influence the crystal symmetry and magnetic interactions [45, 46]. These compounds display a remarkable diversity of magnetic ground states arising from geometric frustration, SOC, and competing exchange interactions that can be tuned by both the A-site and Ln-site cations. For example, Sr_2LnRuO_6 (Ln = Dy, Ho, Er) crystallizes in a low-symmetry monoclinic structure and exhibits two magnetic phase transitions as well as exchange-bias effects, likely driven by antisymmetric exchange (D-M) interactions enabled by the reduced lattice symmetry [47, 48, 49, 50, 51]. In contrast, replacing the magnetic rare-earth ion by nonmagnetic Y^{3+} in Sr_2YRuO_6 preserves the same crystal symmetry but leads to planar antiferromagnetic correlations and a partially ordered frustrated state, emphasizing the crucial role of magnetic 4f moments [52].

1.3.3 Intermediate Coupling, Hund's Physics, and Orbital Effects

The intermediate correlation strength in ruthenates arises from the spatial extent of Ru 4d orbitals, which increases overlap with oxygen 2p states and widens the electronic bands. Although this suppresses electron localization, the coulomb interaction is still sufficient to strongly renormalize the electronic states, leading to correlated metallic or weakly insulating behaviour [2].

Hund's coupling plays a central role in this regime by aligning spins across partially filled t_{2g} orbitals and suppressing inter-orbital charge fluctuations. Many ruthenates are therefore understood as Hund's metals, where strong correlations arise from Hund's-rule physics rather than proximity to a Mott transition [3]. The multi-orbital nature of the Ru t_{2g} manifold further enables orbital differentiation, which strongly influences magnetism and excitation spectra.

1.4 Structural Diversity and Structural Tunability in Ruthenium-Based Oxides

Ruthenium oxides show a wide range of physical properties because of their structural variety. Unlike many transition-metal oxides, which usually form a single type of crystal structure, ruthenates can adopt many different structures, including perovskite, layered perovskite, pyrochlore, double perovskite, hexagonal and cluster-based forms as shown in Fig. 1.3 [44, 45, 53, 54, 55]. This flexibility in structure allows researchers to tune properties such as electronic bandwidth, orbital overlap, and dimensionality, all within chemically similar compounds. As a result, ruthenates are especially useful for studying how changes in structure affect electronic and magnetic behavior in correlated electron systems. Most of the ruthenium oxides are made up of RuO_6 octahedra. Small rotations and tilts of these octahedra change the Ru-O-Ru bond angles, which directly influences electron hopping,bandwidth and exchange interaction. This thesis focused on two types of Ruthenium base compounds in which one is 6H perovskite $Ba_3RRu_2O_9$ compounds and other is barium ruthenate trimer system. The representation of face shared dimer and trimer made of RuO_6 octahedra is shown in Fig. 1.4. Hexagonal ruthenates, particularly the $6H$ perovskite, are characterized by the presence of face-sharing RuO_6 octahedra. In these structures, Ru ions form dimers with significantly reduced Ru-Ru distances compared to corner-sharing networks. A prominent example is the $Ba_3RRu_2O_9$ family (R = rare-earth or non-magnetic ions), where alternating Ru_2O_9 dimers and RO_6 octahedra create a reduced-dimensional lattice that strongly affects electronic and magnetic behavior. These systems provide an excellent platform to study cluster-based magnetism, $4d$-$4f$ interactions, and the interplay between structure, orbital occupancy, and electron correlations.

In ruthenium trimer-based systems, three face-sharing RuO_6 octahedra combine to form Ru_3O_{12} trimers, within which strong intratrimer interactions dominate.

In ruthenium oxides, the way RuO_6 octahedra are linked plays a decisive role in determining whether electrons act as localized moments or as more itinerant, delocalized carriers. In corner-sharing networks, wider electronic bandwidths promote correlated metallic behavior, whereas face-sharing or cluster-based arrangements increase direct Ru-Ru interactions and favor molecular-orbital formation. This structural flexibility is a key reason for the remarkable variety of electronic and magnetic ground states seen in ruthenates. It also offers a straightforward way to tune correlated behavior through small

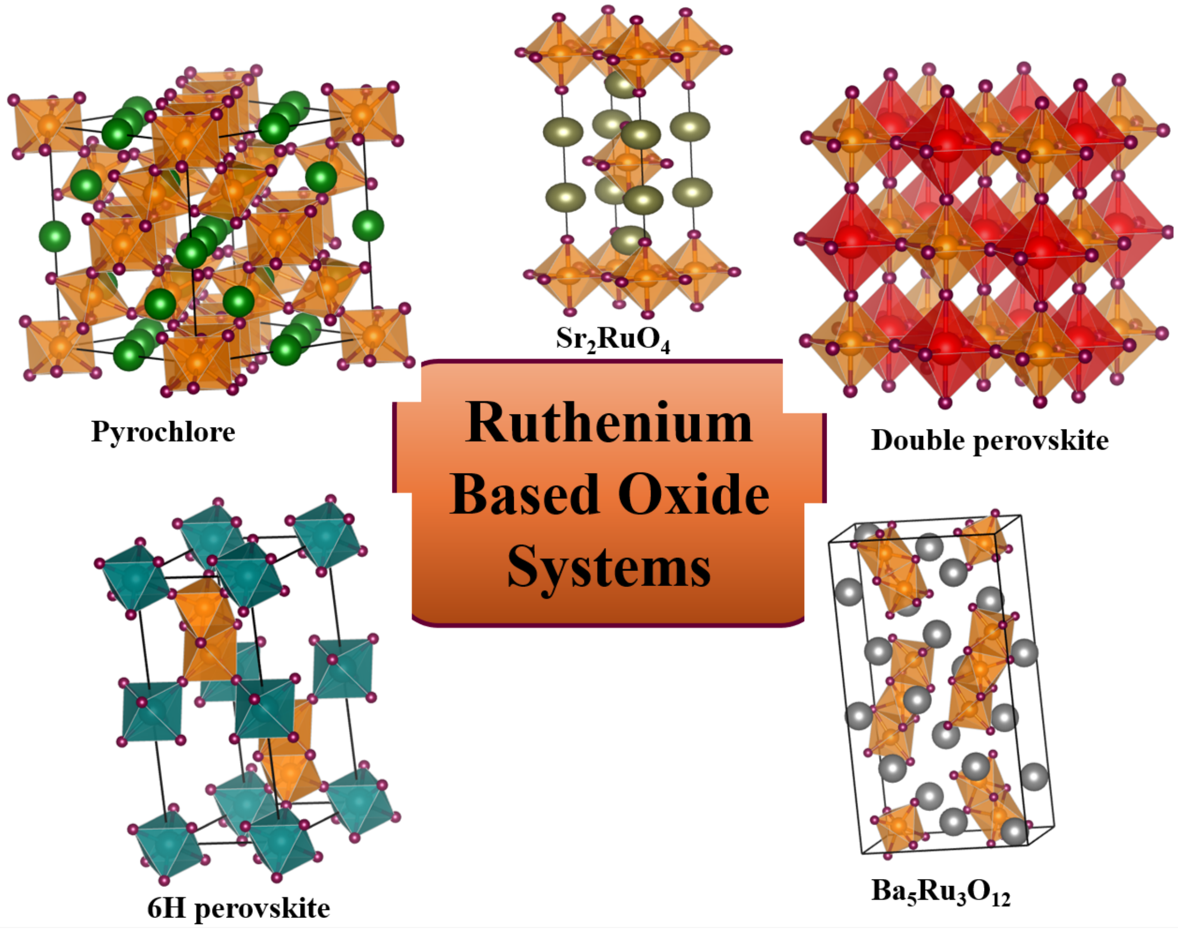

Figure 1.3: Representative crystal structures of ruthenium-based oxides, including pyrochlore, 6H perovskite, layered perovskite , double perovskite, and trimer systems, highlighting the structural diversity that gives rise to a wide range of electronic and magnetic ground states.

changes in the crystal structure.

1.5 Cluster Magnetism in Ruthenium-Based Oxides: Dimers and Trimers

A defining feature of many ruthenium-based oxides is that magnetism does not originate from isolated Ru ions but instead emerges from small clusters of Ru atoms formed through specific structure. In compounds containing face-sharing RuO_6 octahedra, the Ru-Ru distance is significantly reduced, leading to strong direct overlap between Ru $(4d)$ orbitals. This overlap promotes partial electron delocalization over multiple Ru sites

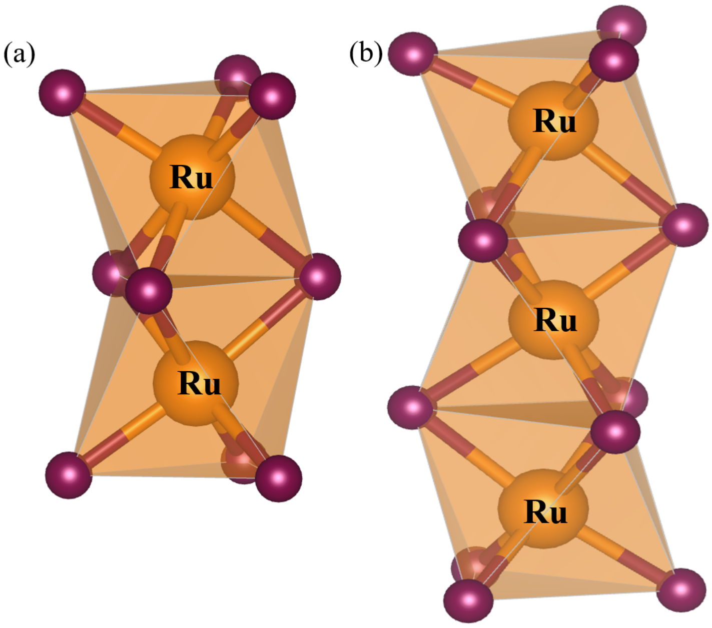

Figure 1.4: Representation of (a) Ru dimer (b) Ru trimer formed by face sharing RuO_6 octahedra

and gives rise to cluster-based magnetism, in which dimers or trimers act as the fundamental magnetic units. Such cluster magnetism is not well described by conventional localized-spin and instead reflects the intermediate-coupling nature of Ru $4d$ electrons. The magnetic properties of these systems are therefore governed by a balance between intracluster interactions, weaker intercluster coupling, and the overall lattice geometry.

1.5.1 Ru-Dimer Magnetism in 6H Perovskite Ruthenates

In $6H$ hexagonal perovskite ruthenates of the form $Ba_3RRu_2O_9$, the crystal structure consists of alternating layers of face-sharing Ru_2O_9 dimers and corner-sharing RuO_6 octahedra. For trivalent rare-earth ions, charge neutrality enforces an average Ru valence close to +4.5, resulting in mixed Ru^{4+}/Ru^{5+} configurations within each dimer [46].

As a consequence of the face-sharing geometry described above, the Ru_2O_9 dimer behaves as a collective magnetic unit, leading to partial electron delocalization across the two Ru sites. Due to this the magnetic moment is distributed over the dimer rather than localized on individual Ru ions. In many cases, the Ru_2O_9 dimers behaves as a single magnetic unit with a reduced effective moment [56, 57].

The magnetic behavior of these dimer systems is further influenced by the nature of the rare-earth ion for example light rare earth ions show dimer ordering while in heavy rare earth ions show cooperative ordering of R and Ru. when the R site is occupied by a non-magnetic ion (such as Y^{3+}, La^{3+}, or Lu^{3+}), it plays an important but indirect role in determining the magnetic ground state of the system [58, 59, 60, 61]. Although R^{3+} does not contribute a magnetic moment, it strongly influences the crystal structure by controlling lattice parameters, Ru-O bond lengths, and Ru-O-Ru bond angles within the Ru_2O_9 dimers. These structural parameters govern the balance between intra-dimer exchange, inter-dimer coupling, and electron hopping between Ru ions, thereby tuning the degree of electron localization and magnetic frustration. As a result, the magnetic behavior in non-magnetic R compounds is dominated by the Ru sublattice, often stabilizing singlet, weakly magnetic, or dimer-driven ground states rather than long-range magnetic order. In contract to this when R carries a magnetic moment, additional $4d$-$4f$ exchange interactions come into play, leading to more complex magnetic behavior that reflects the interplay between Ru dimer magnetism and rare-earth anisotropy. In compounds like $Ba_3NdRu_2O_9$ and $Ba_3HoRu_2O_9$, several magnetic transitions are observed, indicating an interplay between the magnetic ordering of the Ru dimers and that of the rare-earth moments [58, 62].

1.5.2 Ru-Trimer Magnetism and Molecular-Orbital Formation

In ruthenium oxides containing Ru_3O_{12} trimers, cluster magnetism is strongly enhanced by the presence of three face-sharing RuO_6 octahedra. The short Ru-Ru separations within these trimers drive strong intratrimer hybridization, leading to molecular-orbital-like electronic states delocalized over the trimer. Because of this strong hybridization, the three Ru sites within a trimer are often magnetically inequivalent. In some compounds, the central Ru ion experiences stronger orbital overlap and becomes magnetically inactive, while the outer Ru ions carry most of the magnetic moment. In other systems, all three Ru ions contribute to magnetism, but with unequal moment sizes. The resulting magnetic ground state is therefore a collective property of the trimer rather than a simple sum of individual Ru moments.

The average Ru oxidation state is a key parameter in determining the magnetic ground state of the Ru_3O_{12} trimer. In mixed-valence trimers, the total electron count within the Ru_3O_{12} trimer is fixed by the valence distribution, which in turn determines the effective spin state of the trimers. Depending on the number of electrons and the interactions between trimers, the ground state may be a low-spin state. This is usually accompanied by weaker ordered moments and stronger magnetic fluctuations.

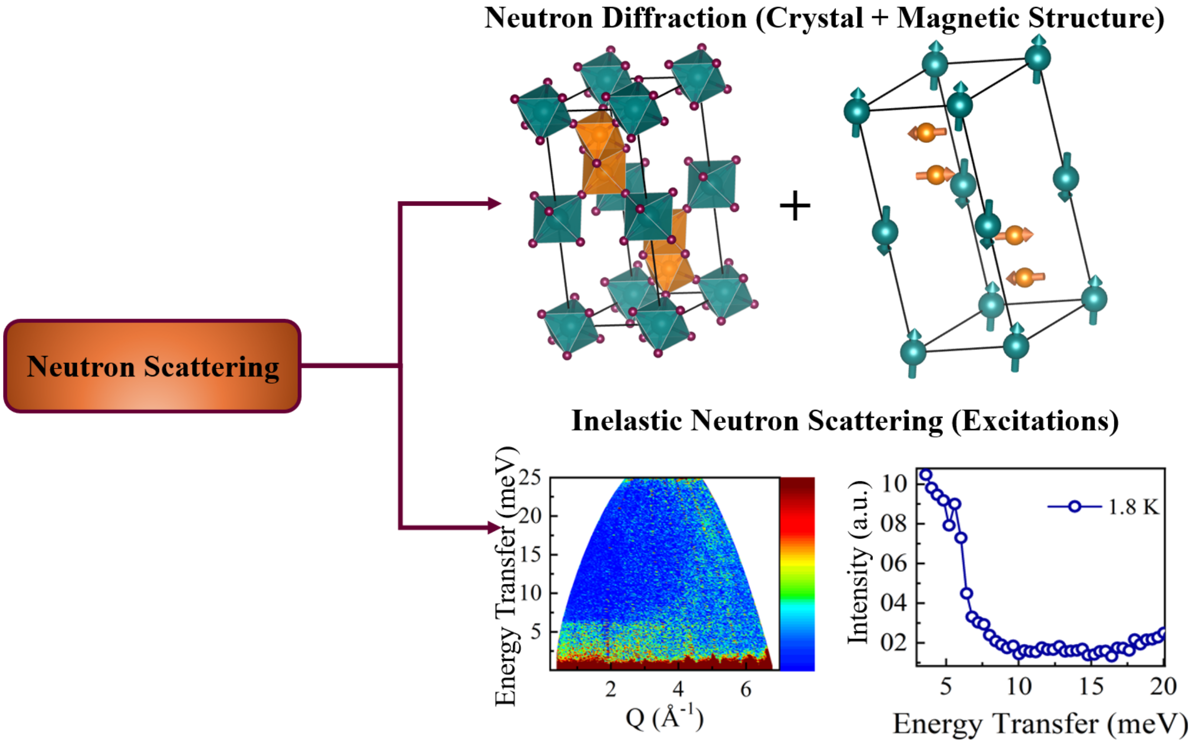

Figure 1.5: Schematic of neutron-scattering probes used to study correlated materials. Elastic neutron diffraction determines the crystal and magnetic structures, while inelastic neutron scattering measures magnetic and lattice excitations, providing access to low-energy collective modes and correlation effects.

1.6 Scope of the Thesis

This thesis provides a microscopic understanding of the electronic and magnetic correlations in ruthenates using neutron scattering. The thesis focuses on ruthenium-based oxides in which RuO_6 octahedra are connected through face-sharing geometries and form Ru dimers and trimers that act as the fundamental magnetic and electronic building blocks. These systems are ideal for uncovering electron correlations, exchange interaction and SOC that govern unconventional magnetism. Within this scope, neutron diffraction is employed to resolve the crystal and magnetic structures, determine ordered moment sizes, and identify the presence of long-range and short-range magnetic correlations and how subtle lattice distortions, bond lengths, and octahedral connectivity within Ru dimers/trimers influence the stability of the magnetic ground states. This allows a direct link to be established between structural motifs and the emergence of reduced magnetic moments. Inelastic neutron scattering is used to probe the low-energy and high-energy magnetic excitations associated with Ru dimers and trimers. The neutron-scattering techniques employed in this thesis, including elastic neutron diffraction for determining crystal and magnetic structures and inelastic neutron scattering for probing magnetic and lattice excitations, are schematically illustrated in Fig. 1.5. These measurements provide access to the characteristic energy scales of intra-dimer/trimer and inter- dimer/trimer exchange interactions, anisotropy, SOC, magnon phonon coupling and CEF Phonon coupling. By analyzing the momentum and energy dependence of the spectra, the thesis elucidates how magnetic correlations evolve from localized dimer/trimer excitations to collective magnetic excitation due to presence of other magnetic atoms. By integrating elastic and inelastic neutron data with complementary structural information, this work aims to construct a unified, microscopic understanding of magnetism in dimer and trimer based ruthenate oxide systems. The scope therefore goes beyond describing individual materials and instead seeks to identify general principles governing how electronic correlations, reduced dimensionality, and molecular-orbital formation control magnetic ground states and excitations in $4d$ transition-metal oxides. In this thesis, neutron diffraction and INS are employed as the primary experimental techniques to investigate both static and dynamic magnetic properties of selected ruthenium oxides.

Chapter 2

EXPERIMENTAL DETAILS

This chapter provides an overview of the sample preparation methods, and the detailed working principles of the experimental techniques employed in this thesis work. The synthesized samples were polycrystalline and prepared using the solid-state reaction method. Confirmation of phase purity and basic structural characterization were conducted using laboratory-based Cu Kα X-ray diffractometer and Scanning-electron Microscope (SEM). I have thoroughly investigated the crystal and magnetic structure employing neutron diffractometer at national and international large-scale facilities. The X-ray and neutron diffraction data were analyzed with the FULLPROF suite and SARAh (Simulated Annealing and Representation Analysis) software [63, 64]. Further, I have carried out inelastic neutron scattering (INS) measurements to explore the magnetic ground states and spin-excitations. I have analyzed the INS data using MantidPlot and DAVE software packages [65, 66]. I have performed Spin-wave simulations using the “SpinW” software to extract the spin Hamiltonian parameters, such as, various magnetic exchange interactions and anisotropy [67]. To calculated the phonon excitations I have performed the machine learned force field (MLFF) calculation using INSPIRED software [68, 69]

2.1 Sample Preparation:Solid State Reaction Method

All the samples are prepared by using the Solid-State Reaction Method. The solid-state reaction method is a conventional and widely used technique for synthesizing polycrystalline materials. It involves forming a new compound through atomic diffusion in the solid state, typically at high temperatures. The schematic illustration of the solid-state reaction method is shown in Fig. 2.1. This method is particularly effective for creating complex oxides and ceramics. Stoichiometric amounts of high purity starting materials, such as oxides, carbonates, nitrates, or elemental powders, are selected based on the desired product. The reactants are finely ground and mixed to ensure uniform distribution and atomic-level homogeneity, using a mortar and pestle. The mixed powders are pressed into pellets applying a pressure of 1-5 Ton using an hydrostatic pressure cell to improve contact between the reactants and minimize loss during heating.

Figure 2.1: Schematic illustration of the solid-state reaction method

The mixture is then sintered at high temperatures in a furnace. The process may involve multiple heating cycles with intermediate grinding to enhance homogeneity. This provides sufficient thermal energy for ions to diffuse and react, forming the desired compound.The sample preparation of specific sample is described in the respective chapter.

2.2 Sample Characterization:X-Ray Diffraction

We use powder X-ray diffraction (XRD) to check the purity of the samples and confirm the desired crystal structure. The XRD profiles for all samples are collected at room temperature using monochromatized Cu Kα_1 radiation ($\lambda = 1.54059$ Å). The diffraction patterns cover from $2\theta = 40°$ to $90°$ with the step size of 0.001. We have analyzed the XRD pattern with Rietveld Refinement using FullProf Suite softwear [63].

The XRD follows the Bragg's law (presented schematically in Fig. 2.2),

$$2d\sin\theta = n\lambda \tag{2.2.1}$$

where θ is the angle between the incident beam and the crystal surface, n is an integer, λ is the wavelength, and d is the spacing between atomic layers. In XRD, the Scattering cross section depends on various factors which can be understood by the following equation:

$$\frac{d\sigma}{d\Omega} = \left| \sum_j f_j(Q)\, e^{-2\pi(hx_j+ky_j+lz_j)}\, e^{-B(\sin\theta/\lambda)^2} \right|^2 \tag{2.2.2}$$

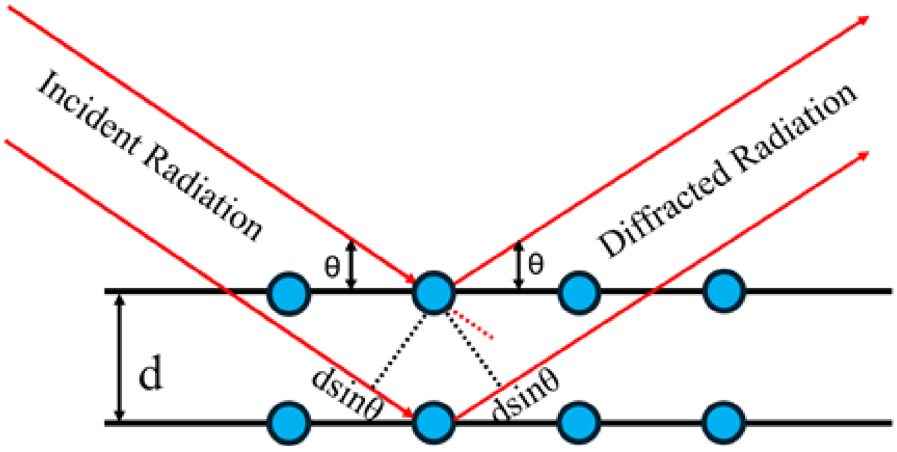

Figure 2.2: Bragg Diffraction. Two beams with identical wavelength and phase approach a crystalline solid and are scattered of two atoms within it.

Here, (h, k, l) are the Miller indices, and (x, y, z) are the fractional atomic coordinates of the j_{th} atom. This equation shows that the diffraction peak broadened and its intensity decreases with increasing temperature due to atomic thermal vibrations. The detailed analysis of the XRD pattern gives an clear idea about, structure, spatial symmetry, atomic arrangement and defect, homogeneity, an estimate of sample dimension, etc. The analysis of XRD data is discussed in later section.

2.3 Synchrotron XRD

To obtain detailed structural information as a function of temperature we use high-resolution synchrotron X-ray diffraction (HRXRD) source. Unlike conventional laboratory XRD, which uses fixed-energy X-ray sources, HRXRD employs highly intense and tunable X-rays generated at synchrotron facilities, providing much higher resolution and sensitivity. The high photon flux of synchrotron radiation allows rapid data collection and the detection of weak diffraction features. This makes HRXRD particularly suitable for studying subtle structural changes, such as phase transitions, lattice strain, and thermal evolution of the crystal structure. The excellent angular resolution further enables accurate analysis of complex and nano-crystalline materials. Compared to laboratory-based XRD, HRXRD offers significantly higher intensity, tuneable X-ray energy, and superior time and spatial resolution. These advantages allow us to monitor temperature-dependent structural evolution and capture transient structural changes that are not accessible using conventional XRD methods. In this thesis work, HRXRD measurements were performed at the SOLEIL Synchrotron to investigate the detailed crystal structure and its temperature-dependent evolution. The use of synchrotron radiation provides high photon flux and excellent angular resolution, enabling precise structural analysis beyond the capability of conventional laboratory XRD.

2.4 Neutron Scattering

Neutron scattering is a powerful technique used to probe the atomic and magnetic structure of materials as neutrons have spin which interacts with the nucleus. It involves directing a beam of neutrons at a sample and analyzing the scattered neutrons to gather information about the sample's properties. A nuclear physicist, J. Chadwick discovered the neutron in 1932 and in 1935 he received a Nobel Prize for his discovery. Neutron has no charge which gives zero electric dipole moment due to this it penetrates deeper into nuclei rather than an electron cloud. In 1994 Brockhouse and Shull were honored with the Nobel Prize in physics for developing neutron scattering techniques for studying condensed matter. In addition to being complementary to XRD, neutron powder diffraction is also often used in conjunction with other neutron scattering techniques. These include single crystal neutron diffraction in crystal structure and magnetic structure studies; small angle neutron scattering in microstructural studies; diffuse scattering in crystallization studies; and INS in the study of phase transformations and critical phenomena [70, 71, 72, 73, 74]. The reason we are using neutron diffraction is given below:

1. We need a sort of radiation which interacts weakly with matter, so that we are able to treat the scattering in Born approximation or in other words: we want to see the creation of one excitation and no multiple scattering.

2. The energy E_0 and momentum k of the desired radiation should be of the order of the energies and momenta of the excitations to be studied. In other words: the wavelength. should be comparable to the atomic distance, the energy E_0 should be comparable to thermal energies (a few meV to 0.5 eV).

3. For the study of magnetic properties, we need an interaction of our magic radiation with electronic spins. All these demands are rather well fulfilled by neutrons. Looking for alternatives there are charged particles like protons or electrons. Because of the strong Coulomb-interaction both cannot penetrate deeply into a target. One only sees surface effects.

4. Furthermore, the neutron's wavelength ($\lambda_n \sim$ 1-5 Å) is close to interatomic distances and its energy is comparable with those of many excitations in condensed matter, which means that neutron scattering also has a spectroscopic function.

5. Neutrons interact with matter primarily through nuclear forces rather than electric forces. Therefore, the interaction cross-section depends on the internal structure of the nuclei in the sample being studied, rather than on the atoms' mass or electric charge. This characteristic allows neutrons to be equally sensitive to both heavy and light atoms. It is possible to find out oxygen deficiency in an oxide using Neutron diffraction, which is not possible through XRD.

Neutrons are produced in two primary ways: through nuclear reactors and spallation sources. Nuclear reactors use a fission process to produce neutrons, while spallation process implies high-energy protons striking a solid target.

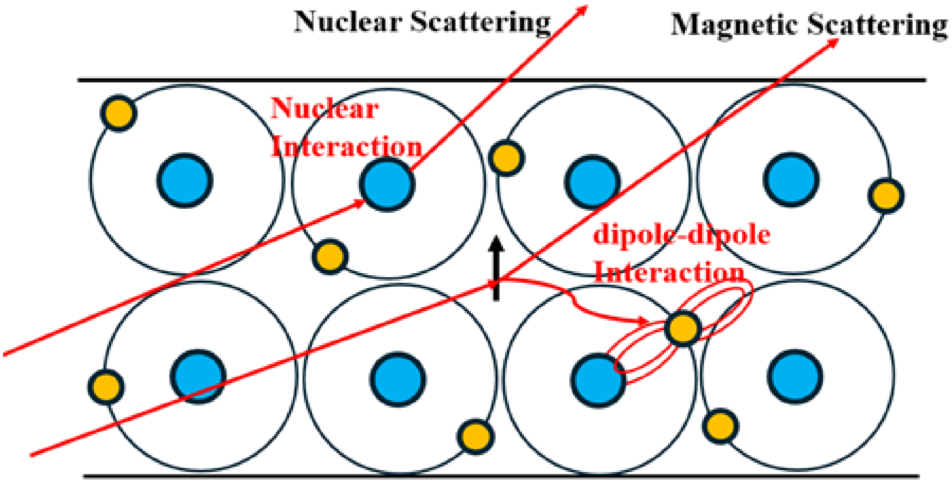

Figure 2.3: Schematic diagram of Neuclear and Magnetic Scattering

2.4.1 Nuclear Scattering for Structural Characterization

Nuclear scattering constitutes the dominant contribution to the partial differential scattering cross-section. The nuclear scattering potential is short-ranged and depends on the positions of the nuclei. It also depends on the nature of the nucleus, including the isotope and the relative orientation of the nuclear and neutron spins. In this process, the incident neutron interacts directly with the nucleus, as illustrated in Fig. 2.3. Nuclear scattering consists of two components which is coherent scattering and incoherent scattering as mention in equation. 2.4.3

$$\frac{d^2\sigma}{dE_f\,d\Omega} = \left(\frac{d^2\sigma}{dE_f\,d\Omega}\right)_{\text{coherent}} + \left(\frac{d^2\sigma}{dE_f\,d\Omega}\right)_{\text{incoherent}} \tag{2.4.3}$$

The coherent scattering is a result of coherent interference from the nuclei in the sample whereas the incoherent scattering is due to the variance in scattering lengths and creates an isotropic background. The incoherent cross section is

$$\sigma_{\text{inc}} = 4\pi\left(\overline{b^2} - \bar{b}^2\right). \tag{2.4.4}$$

The partial differential cross-section for nuclear scattering is:

$$\left(\frac{d^2\sigma}{dE_f\,d\Omega}\right)_{\text{coherent}} = \frac{k_f}{k_i}\,S(Q,\omega) \tag{2.4.5}$$

$$\left(\frac{d^2\sigma}{dE_f\,d\Omega}\right)_{\text{incoherent}} = \frac{k_f}{k_i}\,S_{\text{inc}}(Q,\omega) \tag{2.4.6}$$

2.4.2 Magnetic Scattering: Scattering cross section and structure factor

Magnetic scattering results from the interaction of the neutron with the electromagnetic field of the unpaired electrons and from the orbital momentum of the unpaired electrons of the ions in the sample as shown in Fig. 2.3 . The magnetic dipole moment of the neutron, $\boldsymbol{\sigma}$, interacts with this electromagnetic field. Due to quantum nature, a neutron beam can be described with a complex plane wave function

$$\Psi(\mathbf{r}) = A\exp(i\mathbf{k}\cdot\mathbf{r}), \tag{2.4.7}$$

with $\mathbf{k}$ the neutron wavevector, $\mathbf{r}$ the spatial coordinate, and A normalization factor. After the scattering process and near a scattering centre (nucleus), the wavefronts can be described as spherical waves

$$\Psi_{\text{sc}}(\mathbf{r}) = -\frac{Ab}{r}\exp(ikr), \tag{2.4.8}$$

However, far from the scattering centre, where neutrons are detected, they can be described as planar waves. Here we have introduced b, the scattering length, expressing the strength of the interaction between the neutron and the nucleus. In a neutron scattering experiment incident neutrons, with wave vector k_i, are scattered at an angle θ with a wave vector k_f. If energy is transferred to the sample the neutron energy change is following Fermi-Golden rule:

$$\hbar\omega = E_i - E_f = \frac{\hbar^2 k_i^2}{2m_n} - \frac{\hbar^2 k_f^2}{2m_n} \tag{2.4.9}$$

where m_n is the mass of the neutron and $\hbar = h/2\pi$, h is Plank's constant. Momentum is also transferred to the sample and the neutron momentum change is $-\hbar Q$. The wave vector transfer, Q is calculated as

$$Q = k_i^2 + k_f^2 - 2k_i k_f \cos\theta = \frac{m_n}{\hbar^2}\left(2E_i - \hbar\omega - 2\sqrt{E_i(E_i - \hbar\omega)}\cos\theta\right) \tag{2.4.10}$$

The weak scattering which occurs can be well approximated by the first-order perturbation theory of the Born approximation, which assumes that incident and scattered neutron beams are plane waves. The measured quantity in a neutron scattering experiment is the differential scattering cross section, denoted $(d^2\sigma)/(d\Omega dE_f)$. This quantity is proportional to the number of neutrons scattered per second in a solid angle Ω oriented in each direction, with a final energy between E_f and $E_f + dE_f$:

$$\frac{d^2\sigma_f}{d\Omega dE_f} = \frac{k_f}{k_i}\frac{1}{2\pi\hbar}\sum_{j,k}\overline{(b_k b_j)}\int_{-\infty}^{\infty}\langle \exp(-i\mathbf{Q}\cdot\mathbf{r}_j(0))\exp(i\mathbf{Q}\cdot\mathbf{r}_k(t))\rangle \exp(-i\omega t)\,dt \tag{2.4.11}$$

Or

$$\frac{d^2\sigma_f}{d\Omega dE_f} = \frac{k_f}{k_i}S(Q,\omega) \tag{2.4.12}$$

Here $S(Q,\omega)$ is called the dynamical structure factor, and is usually the quantity of interest in a neutron experiment because it is ideally independent of the instrument geometry and the incident neutron wavelength. Essentially, $S(Q,\omega)$ is a response function (in the sense that it is the response to the perturbation introduced in the scattering system by the neutron), which measures space- and time-correlations and represents the spontaneous fluctuations of atomic positions in the system. k_i is the incident wave vector, $\overline{b_j}$ refers to the scattering length of the atom j (the bar represents an isotope and spin average), $r_j(t)$ is the position in space of the atom j at time t, and $\langle\ldots\rangle$ represents a thermal average.

2.4.3 Neutron Powder Diffraction (NPD) to investigate crystal and magnetic structure

To investigate the crystal and magnetic structure of the sample NPD measurement is performed. In this case incident neutron get diffracted from the sample without changing their energy or momentum ie elastic scattering. For this, since $\hbar\omega = 0$, then $k_i = k_f$ and so Q is dependent on the scattering angle, θ, only. shows the elastic scattering triangle for two different Q vectors but for the same incident wave vector length k_i. Time-of-flight (TOF) neutron diffraction was employed to extend the NPD measurements by providing high-resolution structural and magnetic information over a broad range of momentum transfer. In this technique, a pulsed polychromatic neutron beam is used, and the wavelength of each detected neutron is determined from the time it takes to travel from the source to the detector, allowing diffraction patterns to be recorded simultaneously for many wavelengths at a fixed scattering angle. This enables efficient coverage of a wide Q range in a single measurement, which is particularly advantageous for resolving overlapping Bragg peaks and separating nuclear and magnetic contributions. The TOF method also offers excellent peak resolution at both low and high d-spacings, making it well suited for accurately refining lattice parameters, atomic positions, and long-range magnetic order. In the present work, TOF neutron diffraction was therefore used to complement the conventional NPD data and to provide a more reliable and comprehensive description of the structural and magnetic properties of the system.

In this thesis work, Neutron Powder diffraction patterns were collected at PD3 in BARC, Mumbai and Neutron TOF data is collected at SNAP, a time-of-flight diffractometer dedicated to high pressure research at Spallation Neutron Source (SNS), Oak Ridge laboratory, USA.

2.4.4 Inelastic Neutron Scattering

INS is a spectroscopic technique used to investigate the vibrational and magnetic properties of materials. Neutrons are ideal for inelastic scattering experiments because they possess both wave-like and particle-like characteristics. When neutrons interact with the atomic nuclei in a sample, they can transfer energy to or absorb energy from the nuclei, leading to changes in neutron energy and momentum. These energy transfers correspond to various excitations within the material, such as vibrations of the atomic lattice or magnetic interactions. In a typical neutron scattering experiment, an incident neutron beam k_i is pointed toward the sample, and the scattered neutron k_f is detected at various angles from the incident direction. The scattering vector is defined as: $Q = k_i - k_f$ and, if there is a change in energy between the incident and scattered neutrons then equation 2.4.9 get changed. For inelastic scattering, $\hbar\omega \neq 0$, and so $k_i \neq k_f$ and a range of Q values are achieved over a range of scattering angles by using equation 2.4.10. The change in neutron energy is given by,

$$\Delta E = E_i - E_f = \frac{\hbar^2}{2m_n}\left(k_i^2 - k_f^2\right) \tag{2.4.13}$$

The excitation energy, ΔE is the amount of energy ($\hbar\omega$) transferred to the sample with wave vector q, and can be expressed as,

$$\Delta E = E_i - E_f = \hbar\omega \tag{2.4.14}$$

and

$$k_i = k_f + q + G \tag{2.4.15}$$

where, G denotes the reciprocal lattice vector. Thus, by knowing k_i, k_f, E_i and E_f we can determine ω and q, and hence the spin wave dispersions.

In this thesis work, INS measurements were carried out on the fine-resolution Fermi-chopper spectrometer SEQUOIA at the Spallation Neutron Source (SNS) at Oak Ridge National Laboratory (ORNL), US.

2.5 Analysis Techniques of diffraction and Inelastic Neutron Scattering Data

The diffraction data were analysed by employing “Rietveld refinement” (FULLPROF program) to determine the crystal/magnetic structure. The INS data were analysed by employing “Mantid/plot” to visualize the INS spectra, “SpinW” program to determine the spin-Hamiltonian. The details of the analysis techniques are discussed briefly one after other below.

Rietveld Refinement

The Rietveld refinement method, developed by Hugo Rietveld, is a widely used technique for determining and analyzing crystal structures. This method employs a least-squares refinement approach, where initial approximate structural parameters are provided as starting values. During refinement, various crystal structural parameters, including lattice constants, atomic positions, site occupancies, instrumental factors, peak shape factors, temperature factors, anisotropy parameters, preferred orientation, and background, are iteratively adjusted to minimize the difference between observed and calculated diffraction patterns for nuclear structures. For magnetic structures, parameters such as the magnetic moment are also refined. The Rietveld refinement technique is implemented in the FULLPROF software suite [63]. Magnetic structure determination often incorporates representation theory analysis, which can be performed using tools such as BASIREPS and SARAh (Simulated Annealing and Representation Analysis) [63, 64]. These methods ensure an accurate determination of both nuclear and magnetic structural parameters.

INS Data Analysis

The INS data was plotted and analyzed by the Mslice program implemented in the MantidPlot software package [65]. Constant-energy and constant-Q cuts were generated by integrating the scattering intensity over selected ranges of momentum and energy transfer. The resulting spectra were corrected for non-magnetic background contributions and further processed by applying Bose population factor corrections to account for the thermal occupation of excitations. In particular, Bose-factor convolution and subtraction procedures were employed to separate intrinsic magnetic scattering from temperature-dependent phonon and background contributions, thereby enhancing the magnetic signal. Additional analysis, including detailed visualization, peak fitting, and the extraction of characteristic excitation energies and linewidths, was performed using the DAVE(Data Analysis and Visualization Environment) software package [65, 66]. The combined use of MANTID/MSLICE and DAVE enabled a comprehensive and quantitative analysis of the magnetic excitation spectrum and its evolution with momentum transfer and temperature.

2.6 SpinW simulation

The spin-wave simulations were performed to model the experimentally observed INS spectra by using the "SpinW" program [67]. The spin wave simulations using the "SpinW" program allows to solve the spin Hamiltonian given as

$$H = \sum_{ij} (\mathbf{S}_i J_{ij} \mathbf{S}_i) + \sum_{i} \left(\mathbf{S}_i A_{(i)} \mathbf{S}_i\right) + B \sum_{i} (g_i \mathbf{S}_i) \tag{2.6.16}$$

where, S_i are the spin operators, and J_{ij} are the exchange interactions between the spins represented by 3×3 matrices, B is the external applied magnetic field and g_i is the g-tensor. "SpinW" program is based on linear spin wave theory. The spin operators (S_i) in the spin Hamiltonian are expressed by the ladder operators (S_i^+, S_i^-, S_i^z). The ladder operators are mapped to bosonic annihilation or creation. The Hamiltonian is transformed by Holstein-Primakoff transformation and then expressed by the series expansion of the powers of a^+ and a. As per the linear spin wave theory, the terms proportional to the to a^+ and a, are only considered for the calculation. The diagonalization of the Fourier transform of the Hamiltonian gives the required solution. The “SpinW” program solves the spin Hamiltonian for magnetic systems using classical and linear spin wave theory. SpinW can calculate spin wave dispersion, spin-spin correlation functions, and neutron scattering cross sections for both unpolarized and polarized neutrons [67]. It employs the Holstein-Primakoff transformation to express spin operators in terms of bosonic creation and annihilation operators, and diagonalizes the resulting Hamiltonian in momentum space to obtain the excitation spectrum. The software is particularly suited for complex magnetic crystals with arbitrary exchange interactions and anisotropies. The calculated spin wave spectra can be directly compared with experimental INS data.

2.7 Machine Learned Force-Field (MLFF) calculation

A force-field calculation is a computational approach used in atomistic simulations to determine the forces acting on atoms based on their positions. It defines how the total energy of a system changes with atomic coordinates using mathematical functions that describe interatomic interactions. Once the forces are known, the time evolution of atomic motion can be simulated using molecular dynamics. These forces can accurately obtain using Density Functional Theory (DFT), which is based on quantum mechanics. However, this is very expensive and takes lots of time. To overcome this, we have used MLFFs, which is trained using DFT energies and forces and can reproduce near-DFT accuracy at a much lower computational cost. This allows us to perform large-scale and long-time simulations while maintaining high accuracy [68, 69]. We have performed the MLFF calculation to generate the phonon excitation using Inspired software which is shown in Fig. 2.4. MLFFs have shown that they can accurately reproduce phonon spectra at the DFT level while naturally including temperature effects. By running molecular dynamics simulations with MLFFs and analyzing the velocity autocorrelation functions, we can obtain vibrational densities of states and phonon spectra. This approach captures important temperature effects, such as phonon softening and spectral broadening. This is especially useful for studying vibrational properties related to thermal transport, neutron scattering, and phase stability. Compared to conventional ab initio lattice dynamics, MLFF-based methods go beyond the harmonic approximation and avoid issues such as imaginary phonon modes in systems that are stable only at finite temperatures.

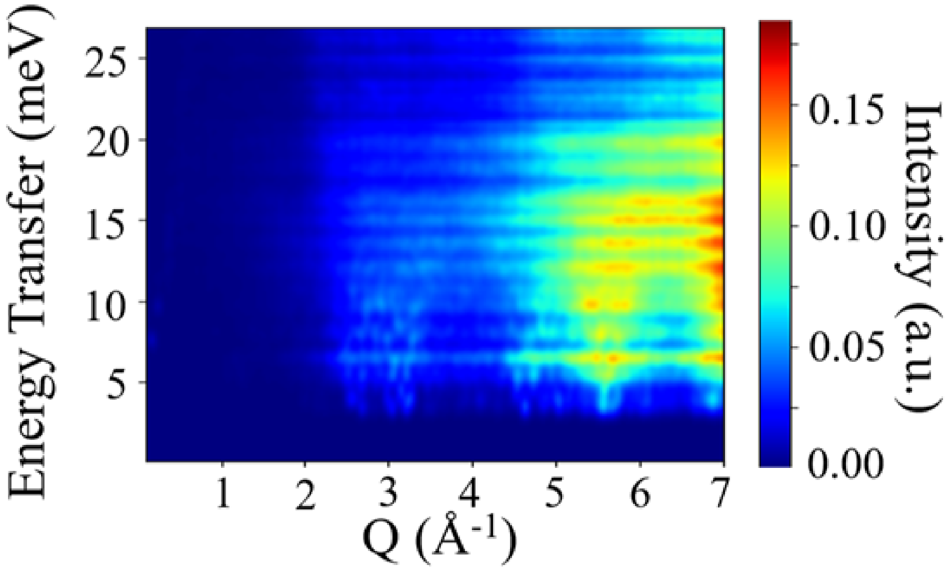

Figure 2.4: MLFFs calculated Phonon Excitation present at high Q

2.8 Raman Spectroscopy

A powerful, non-destructive physical method of examining the dynamics of a crystal lattice by means of its interaction with electromagnetic radiation is Raman spectroscopy. A typical experiment using Raman Spectroscopy will consist of direct laser illumination (monochromatic) of a sample and analysis of the spectrum of the light that has been diffracted elastically from the sample. While a very small fraction of the total number of photons that are diffracted from the sample experience an energy change due to either the creation or destruction of phonons (lattice vibrations), the resultant energy change manifests itself as a Raman shift. Identifying both Stokes and anti-Stokes scattering are a key aspect of Raman Spectroscopy. The Raman shift then enables determination of the lateral distribution, distance, frequency, and lifetime of phonon modes within the crystal lattice. From a physics perspective, Using Raman spectroscopy one can explore the detailed phonon spectra, lattice symmetry, and spin-lattice or electron-phonon interactions. The Changes in phonon frequencies, linewidths, or intensities can reveal structural distortions, phase transitions, anharmonic effects, and coupling between lattice and magnetic or electronic degrees of freedom. In the present work, Raman spectroscopy is used to identify zone-center optical phonon modes. The observed phonon frequencies are converted into energy units to systematically compared with inelastic neutron scattering (INS) results that provide a complementary understanding of lattice dynamics across different regions of the Brillouin zone and provide consistency between optical and neutron-based probes of phonon excitations.

In this work the room temperature Raman Spectroscopy is performed at the Central Instrumentation Facility (CIF) at Rajiv Gandhi Institute of Petroleum Technology (RGIPT) using a 532 nm excitation laser with a 1200 grooves/mm grating, accumulating 100 scans over a spectral range of 200-2000 cm^{-1} at a spectral resolution of 1 cm^{-1}

Chapter 3

Interplay between trimer structure and magnetic ground state in $Ba_5Ru_3O_{12}$ probed by Inelastic Neutron Scattering, spin-wave theory and Machine-learning framework

3.1 Motivation

$Ba_5Ru_3O_{12}$ is a unique member of the barium ruthenate family, as its RuO_6 octahedra form isolated face-sharing Ru_3O_{12} trimers that are separated by nonmagnetic Ba^{2+} ions. Unlike other trimer-based ruthenates where the trimers are connected through corner- or edge-sharing networks, In this system the trimers are isolated that makes it different from other ruthenates trimer and an ideal system for studying the intrinsic electronic and magnetic properties of an individual Ru trimer. Interestingly, despite this isolated trimer structure, magnetic susceptibility measurements indicate the development of long range antiferromagnetic ordering in this system. This behavior is unexpected in a system in the absence of direct magnetic exchange pathways between neighboring trimers and suggests that unconventional magnetic interactions originate within the trimer unit itself. The presence of crystallographically inequivalent Ru sites and the face-sharing geometry are therefore expected to play a crucial role, possibly leading to competing intra- and inter trimer exchange interactions and magnetic frustration.

A detailed investigation of $Ba_5Ru_3O_{12}$ is thus strongly motivated, as it provides an opportunity to understand how Ru-Ru interactions, molecular-orbital formation, and local symmetry effects control magnetism in an isolated $4d$ transition-metal trimer. Such insight is essential for establishing a broader understanding of cluster-based magnetism in ruthenium oxides.

3.2 Introduction: A overview of Barium Ruthenate Trimer Systems

Ruthenium trimer-based oxides have many complex and unusual magnetic ground states, giving rise to a wide variety of interesting physical phenomena for e.g. metal to insulator transition and multiferroicity [75, 76, 77, 78, 79, 80]. These diverse properties arise due to the extended nature of Ru ($4d$) orbitals, CEF, and strong SOC. Even small changes in the local crystallographic environment can lead to substantial changes in the competing exchange interactions, leading to distinct magnetic and electronic ground states. Depending on the synthesis conditions, $BaRuO_3$ crystallizes in different structures (9R,6H,3c and 4H), where variations in the stacking of RuO_6 octahedra give rise to corner-sharing, dimer, or trimer Ru units, as shown in Fig.3.1. In 9R-$BaRuO_3$ (space group $R\bar{3}m$) metal-insulator-type transition is observed without the development of long-range magnetic order, consistent with a nonmagnetic Ru^{4+} ($4d^4$) ground state stabilized by strong CEF splitting and SOC [55]. On the other hand for $Ba_4Ru_3O_{10}$, which also show metal insulator transition no structural change is observed. This compound exhibits antiferromagnetic ordering and crystallizes in the orthorhombic Cmca structure that consists of zig-zag chains of Ru_3O_{10} trimers. Neutron and spectroscopic studies show that the central Ru ion becomes nonmagnetic due to strong Ru-Ru hybridization, while the two outer Ru ions form magnetic units that couple into spin dimers, leading to a gapped magnetic excitation spectrum [75, 76]. Further complexity emerges in $Ba_4LnRu_3O_{12}$, which is isostructural to 9R-$BaRuO_3$ but in this compound Ru_3O_{12} trimers are connected through LnO_6 octahedra. When the rare-earth ion is tetravalent (Ln = Ce, Pr, Tb), all Ru ions remain in the Ru^{4+} ($4d^4$) state, and strong Ru-Ru molecular-orbital formation accommodates all 12 d electrons per trimer, resulting in a nonmagnetic ground state with no Ru

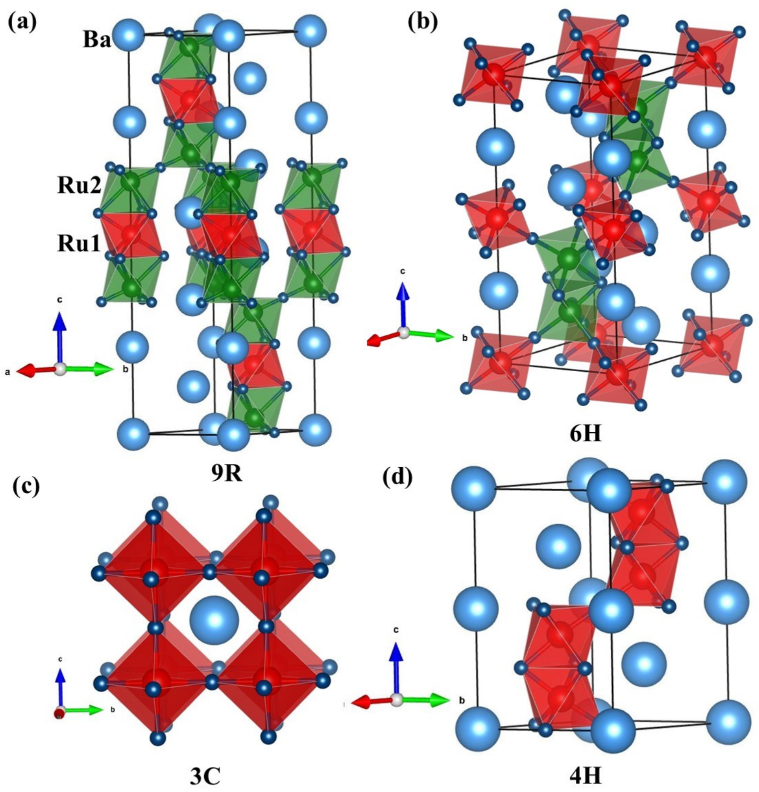

Figure 3.1: Crystal structures of $BaRuO_3$ in different polytypes showing the stacking of RuO_6 octahedra along the c axis: (a) 9R (rhombohedral), (b) 6H (Hexagonal), (c) 3C (cubic), and (d) 4H (Hexagonal).

contribution to the magnetic susceptibility [53, 55]. In contrast, for trivalent rare-earth ions (Ln = La, Nd, Sm-Lu), charge neutrality enforces a mixed Ru valence of approximately +4.33, corresponding to 13 d electrons per Ru_3O_{12} trimer. The additional electron occupies a delocalized trimer molecular orbital, stabilizing an effective $S = 1/2$ trimer ground state and leading to long-range magnetic ordering at low temperatures [53, 55]. Similar physics is observed in $Ba_4NbRu_3O_{12}$, where the average Ru valence is reduced to approximately +3.67. In this case, enhanced Ru-Ru hybridization and odd electron filling stabilize an effective $S = 1/2$ ground state accompanied by strong geometrical frustration and low-temperature magnetic ordering [77].

Together, these trimer-based ruthenates demonstrate that the electron count of the Ru_3O_{12} trimer and the local bonding environment decisively control the magnetic ground state. Integer electron filling leads to nonmagnetic molecular-orbital states, while mixed valence or odd electron count stabilizes effective spin-1/2 trimers. This framework provides a unified basis for understanding the diverse electronic and magnetic behavior ob-

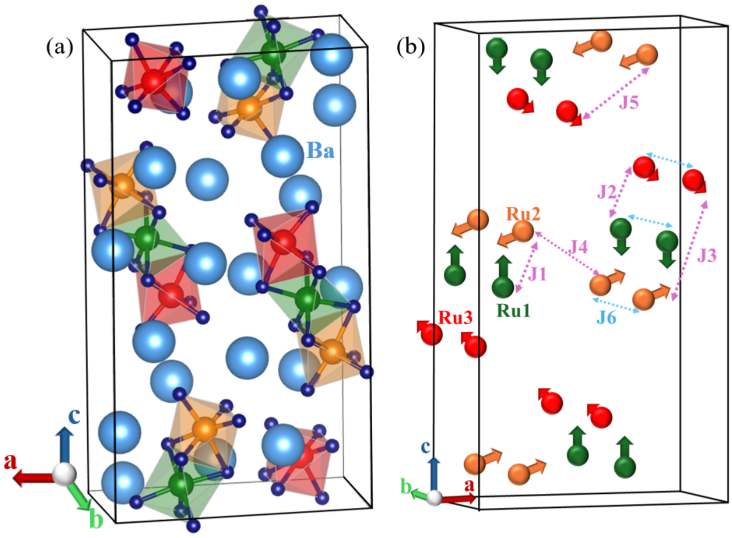

Figure 3.2: (a) Crystal structure and (b) Magnetic Structure of $Ba_5Ru_3O_{12}$.

served in ruthenium-based trimer systems.

3.3 A Overview of $Ba_5Ru_3O_{12}$ Systems

The title compound $Ba_5Ru_3O_{12}$, with an average Ru valence state of +4.67, crystallizes in the Pnma space group and consists of isolated Ru_3O_{12} trimers. Each trimer is formed by three face-sharing RuO6 octahedra. Unlike other barium ruthenates where Ru trimers are connected, In this system Ru_3O_{12} trimers are isolated.The crystal and magnetic structure of $Ba_5Ru_3O_{12}$ is shown in Fig. 3.2.

In the previous study basic magnetic, thermodynamic, and transport properties are studied in this compound. From the magnetic susceptibility long range antiferromagnetic ordering is observed below 60 K while curie weiss fit deviates below 120 K that suggest the development of short range correlation far above the ordering temperature.Also from the fitting large negative Curie-Weiss temperature ($\Theta_{CW} \approx -118$ K) and an effective magnetic moment of about 4.42 μ_B per formula unit is observed, pointing to dominant antiferromagnetic interactions and moderate magnetic frustration. Isothermal magnetization below the ordering temperature shows a linear field dependence, consistent with antiferromagnetic behavior. Heat-capacity measurements reported earlier show a clear anomaly at the magnetic ordering temperature, confirming the bulk nature of the transition. Electrical resistivity measurements performed in this compound reveal insulating behavior with an activation energy of about 0.05 eV and no evidence of a metal-insulator transition. Neutron diffraction studies further revealed that the antiferromagnetic ordering involves three crystallographically nonequivalent Ru sites and a complex non-collinear spin structure, without any accompanying structural phase transition.

To gain deeper insight into the magnetic ground state, we have carried out inelastic neutron scattering (INS) measurements to investigate the magnetic excitations and exchange interactions in $Ba_5Ru_3O_{12}$. The INS spectra were analyzed using SpinW simulations and linear spin-wave theory.

3.4 Experimental details

A polycrystalline sample of $Ba_5Ru_3O_{12}$ was synthesized using a solid-state reaction method by mixing high-quality (>99.9%) chemicals of $BaCO_3$ and RuO_2. A stoichiometric mixture of the raw materials was thoroughly ground, pressed into pellets, and sintered in air at 600 °C for 24 h. The pellets were then reground, and this process was repeated for three cycles. Finally, the powder was pressed again into pellets and sintered at 1200 °C for 24 h [76]. INS experiments were carried out on the fine-resolution Fermi-chopper SEQUOIA spectrometer at the Spallation Neutron Source (SNS) at Oak Ridge National Laboratory (ORNL). Samples were loaded under an atmosphere of helium gas in aluminium cylindrical cans and measured at several temperatures from 4-280 K with incident energy $E_i =$ 30 meV. An empty sample can was measured under identical conditions, and these data have been subtracted from the sample measurements. We have performed the simulation of spin wave using SpinW software to understand the intra- and inter-trimer exchange interactions and exchange anisotropy in the title compound [67]. We have analyzed INS data using Mantid software which used standard Mantid scripts to convert our neutron scattering measurements to standard histograms in energy and detector space [65]. We have used DAVE software for generating scattering intensity and normalized scattering intensity as a function of momentum transfer, |Q|, and energy transfer [66]. Calculations were performed employing the INSPIRED software using pre-trained machine learning force fields (MLFFs) based upon the MatterSim modelling package to calculate the optimized structure and calculate the momentum dependent phonon modes [68, 69].

3.5 Results and Discussions

3.5.1 Inelastic Neutron Scattering: Spin-wave Excitations and Short-Range Spin-correlation

We have performed INS experiment on $Ba_5Ru_3O_{12}$ to investigate the spin wave excitations and short range correlation. The background-subtracted scattering intensity S (|Q|,E) of $Ba_5Ru_3O_{12}$ as a function of energy transfer (E) versus momentum transfer (|Q|) is shown in Fig. 3.3 for selective temperatures of T= 4, 30, 100, 200, and 280 K. A strong intense feature is observed around 10-15 meV in low-|Q| region (0.5 <|Q|< 1.5) below the magnetic ordering temperature(see Fig. 3.3(a-b) for 4 K and 30 K respectively). This intense feature is not observed at higher temperatures in the paramagnetic region (see Fig. 3.3(d-e) for 200 K and 280 K, respectively). A careful observation suggests the presence of a weak excitation around 5.6 meV at 4 K and 30 K which get suppressed at high temperatures in the paramagnetic region. These excitations are further confirmed in the one-dimensional energy cut obtained by integrating a fixed |Q| -region ranging from 0.5 to 1.5 $Å^{-1}$ (intensity versus energy transfer plot in Fig. 3.3(f)). Fig. 3.3(f) exhibits a broad, intense peak from 10-15 meV and a small peak around 5.6 meV at 4 K and 30 K. Both of these features become suppressed or highly damped at higher temperatures. The excitations in the low-|Q| region are considered to be of magnetic origin because the magnetic form factor of the scattering intensity decreases with increasing |Q|, whereas the phonon excitation is usually observed at higher |Q|-regions [22]. The absence of these features above the magnetic ordering temperature is also consistent with these features being associated with the magnetic moments. Hence, we characterize this feature as a spin-wave excitation. Interestingly, we observe a broad weak excitation at 100 K in a large energy range from 6-16 meV at low-|Q| region (see Fig. 3.3(c)), which is documented in the form of a broad low-intense peak in I vs E plot in Fig. 3.3(f). Such a broad and weak feature above T_N often arises from diffuse scattering which is attributable to short-range magnetic ordering from the Ru-trimers. The negative Curie-Weiss temperature (-118 K) is consistent with the presence of short-range spin correlation at 100 K [76] . To further confirm these features as being spin-excitations, we examine the Bose Factor normalized scattering intensity. This quantity is proportional to the dynamic susceptibility χ”(|Q|,E). We first extract the background subtracted (Can subtracted) and Bose factor normalized spectrum at each individual temperature. We then subtract

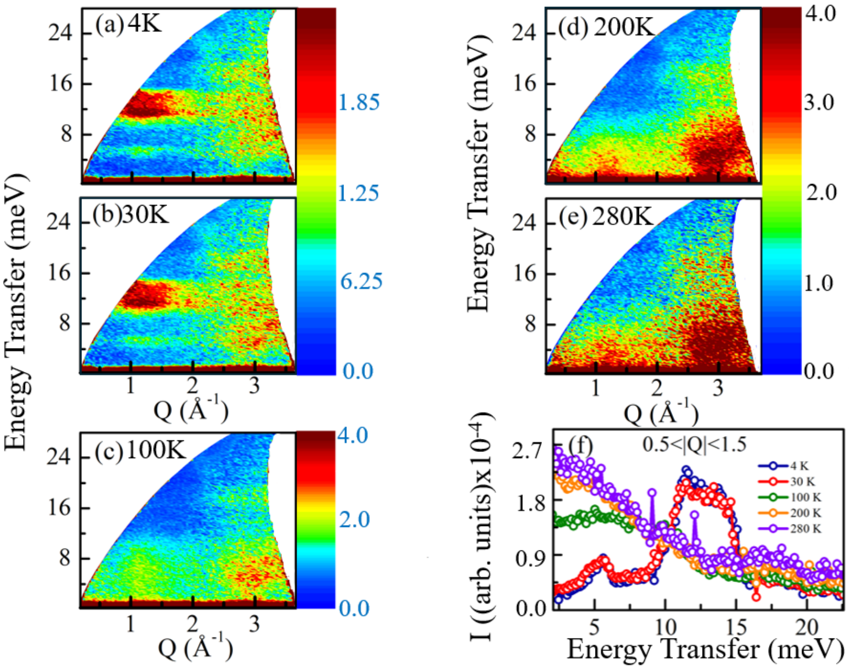

Figure 3.3: Color-coded contour maps of the measured scattering intensity as a function of energy and momentum transfer (|Q|) of $Ba_5Ru_3O_{12}$ using 30 meV incident energy neutrons (a) at 4 K, (b) at 30 K, (c) at 100 K, (d) at 200 K, (e) 280 K and (f) The |Q|-integrated, Intensity vs energy transfer for temperatures between 4 K and 280 K.

the treated data (Can subtracted and Bose factor normalized) at T = 280 K from the lower temperature data, which is referred as Bose factor correction. The result of this for T= 4 K and T= 100 K is shown in Fig. 3.4(a-b). This treatment of the data illustrates the well localized bands of magnetic scattering in the spectrum between 10 and 15 meV energy transfer and around 5.6 meV energy transfer. The difference in the dynamic susceptibility also shows how these features are damped and significantly broadened but are still present even at T= 100 K. The enlarged view of 5.6 meV feature is shown in Fig. 3.4(c) for the 4 K data. These excitations are observed for 30 K with a slightly reduced intensity, as expected for magnetic systems with increasing temperature. The broad weak feature in INS spectra at 100 K (Fig. 3.3(c)) still persists even after Bose factor correction (Fig. 3.4(d)), confirming the persistence of magnetic fluctuations for a range of temperatures greater than T_N. This spectral weight is not significant for T= 200 K as shown in the scattering intensity data of Fig. 3.3(d) as well as the Bose factor corrected data shown in Fig. 3.4(d). For temperatures greater than 100 K, it is likely that the magnetic fluctuations are within a paramagnetic regime and would be contributing to a broad diffuse scattering at and near zero energy transfer.

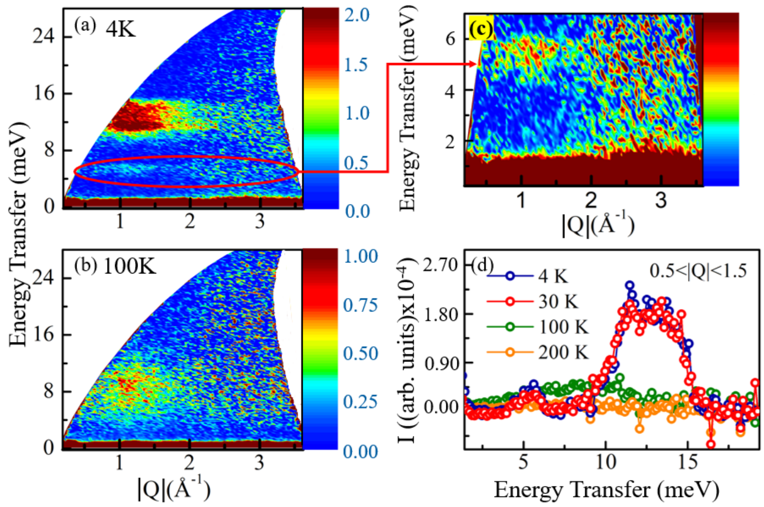

Figure 3.4: Bose factor corrected data (as described in text) of scattering intensity as a function of momentum transfer and energy transfer for $Ba_5Ru_3O_{12}$.The data is first Can subtracted and Bose factor normalized then subtracted from T= 280 K treated data from each data set shown in figure. Panels (a)-(c) are shown on the same color scale as indicated. (a) T= 4 K, (b) T= 100 K , (c) enlarged view of T= 4 K data with intensity scaled by factor of 2, (d) Bose factor corrected scattering intensity as a function of energy transfer, measured over the temperature range 4-200 K. The data are integrated over the momentum range 0.5<|Q|<1.5 Å^{-1}.

This compound has three inequivalent Ru-sites with different magnetic moments. This fact was confirmed in our earlier neutron diffraction results (see Ref.[76]). The 5.6 meV excitation is prominent around $|Q| \sim 1.1$ Å^{-1} which corresponds to the magnetic Bragg peak (010) has been observed in 10 K TOF neutron diffraction results as shown in Fig. 3.5 and Ref.[76]. We have checked that the intensity of (010) in neutron diffraction is only influenced by the magnetic moment of Ru1 atom, which is in the middle of the trimer (see Fig. 3.5). Hence, we conclude that this 5.6 meV spin-excitation is related to the Ru1-spin. The weak intensity of this spin-excitation might be due to the contribution of weak effective exchange interactions originating from various competing exchange interactions, J_1 (Ru1-Ru2) and J_2 (Ru1-Ru3). The broad, intense 10-15 meV peak could result from a combination of multiple peaks, governed by the combined dominant exchange interactions involving the Ru1, Ru2, and Ru3 magnetic atoms.

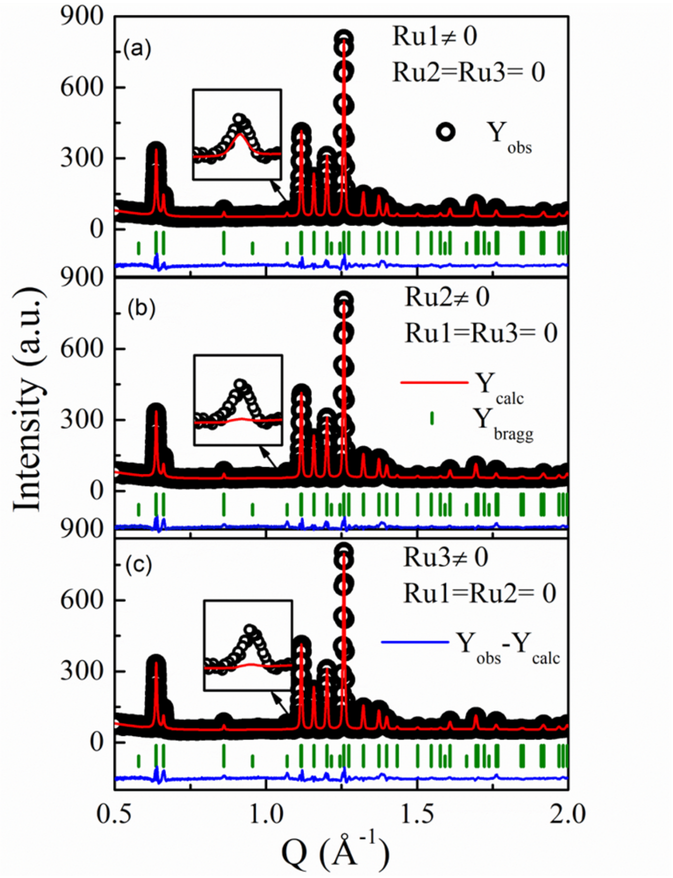

Figure 3.5: Time-of-flight neutron data at 10 K (a) Ru2 = Ru3 = 0, (b) Ru1 = Ru3 = 0 and (c) Ru1 = Ru2 = 0.

3.5.2 Complex Exchange-interaction and Ground State Calculations through SpinW Simulation

To determine the relevant exchange interactions, we have performed SpinW simulations to compare with the experimental INS spectra [67]. Neutron diffraction results suggest an anisotropy along the c-axis, where all the spins tend to align having Ru1, Ru2, and Ru3 ordered moments of 1.52 μ_B, 1.36 μ_B, and 0.91 μ_B respectively [76]. The Ru1 moments aligned exactly along the c-axis, while Ru2, and Ru3 moments are slightly canted with the c-axis in the ac-plane due to exchange frustration. The spin-Hamiltonian for this system, considering all these factors, is expressed as:

$$H = \sum_{i<j} \vec{S}_i^{\mathrm{T}} \mathbf{J}_{ij} \vec{S}_j + \sum_i \vec{S}_i^{\mathrm{T}} \mathbf{D} \vec{S}_i \tag{3.5.1}$$

Where

$$\vec{S}_i = \begin{pmatrix} S_i^x \\ S_i^y \\ S_i^z \end{pmatrix} \quad , \quad \mathbf{J}_{ij} = \begin{pmatrix} J_{ij}^{xx} & J_{ij}^{xy} & J_{ij}^{xz} \\ J_{ij}^{yx} & J_{ij}^{yy} & J_{ij}^{yz} \\ J_{ij}^{zx} & J_{ij}^{zy} & J_{ij}^{zz} \end{pmatrix} \quad \text{and}$$

$$\mathbf{D} = \begin{pmatrix} D^{xx} & D^{xy} & D^{xz} \\ D^{yx} & D^{yy} & D^{yz} \\ D^{zx} & D^{zy} & D^{zz} \end{pmatrix}$$

In the Hamiltonian $\mathbf{J}_{ij}$ is the 3×3 anisotropic exchange tensor, and $\mathbf{D}$ is the single-ion anisotropy tensor. All these interactions occur between two nearest neighbor Ru atoms. The exchange interactions are shown in Fig. 3.2(b) and also tabulated in Table 3.1. The anisotropy is uniaxial, with a non-zero component along the z-direction, $\mathbf{D}_{zz} = -2.1$ meV, while the components along the other directions are zero. The solution of the Hamiltonian with the simulated J-values reproduces a spin structure that closely agrees with the experimentally obtained magnetic structure from neutron diffraction [76]. The simulated spin-wave excitations from this Hamiltonian exactly mimic the experimental INS spectra, yielding a strong spin excitation around 10-15 meV and a weak spin excitation around 5.6 meV, shown in Fig. 3.6(a) (2D contour plot of intensity vs |Q|). The one-dimensional energy cut in (intensity vs. energy transfer) exactly replicates the two excitations with experimentally obtained features in Fig. 3.6(b).

We have checked all the possibilities by tuning the different parameters in the spinW simulations. The exchange anisotropy and J_4, J_5, J_6 is required to exactly replicate the experimentally obtained non-collinear spin-structure along with the intra trimer exchange interactions. Only by tuning intra-trimer exchange interactions (J_1, J_2, J_3), we did not obtain the desired spin-wave excitations, that is, one weak excitation at 5.6 meV and another broad intense excitation between 10-15 meV as observed in the INS experiment. However, 30% variations in J_4-J_6 do not significantly change the excitation energies, but do affect the stability of the magnetic structure which is obtained from experimental neutron diffraction data. The extracted exchange parameters from spinW simulations are summarized in Table 3.1, which reveals the dominant antiferromagnetic (AFM) interactions within the trimer units. The Ru1-Ru2 bond length (∼2.5 Å) is shorter than the typical metallic Ru-Ru distance (∼2.65 Å), suggesting enhanced orbital overlap and a dominant direct AFM exchange interaction ($J_1 = 4.2$ meV) between Ru1 and Ru2. The comparatively smaller value of the effective exchange interaction between Ru1 and Ru3

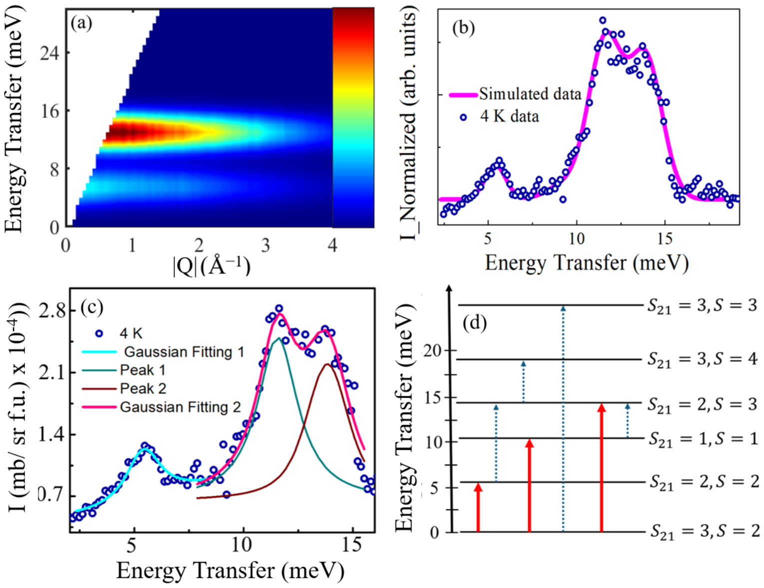

Figure 3.6: (a) Simulated color-coded contour map of the calculated spin-wave excitation spectrum as described in text as a function of momentum transfer $|Q|$ and energy transfer and (b) Intensity vs Energy transfer where line shows the simulated data Obtained from SpinW and open circles show the experimental data at 4 K for |Q|= 0.5 to 1.5 Å^{-1}.The solid line in (b) has been linearly scaled to match the background and scattering intensity of the measurement.(c) Gaussian fitting of 4 K Intensity vs Energy Transfer plot, (d) Theoretically predicted low-lying energy levels with an $S = 2$ ground state. Here, S_{12} indicates the coupling between S_1 and S_2, and S represents the total spin. We observed the three red-arrow transitions. A blue-arrow transition may exist, but we could not detect them at 60 K(ground state transition) as well as at high temperatures (excited state transitions).

(∼2.7 Å, $J_2 = 1.8$ meV) could result from an average value of competing direct exchange interaction and superexchange interaction. The significant AFM exchange interaction between Ru2 and Ru3 ($J_3 = 4.5$ meV) competes with both J_1 and J_2, which gives rise to a non-collinear AFM configuration in this trimer system. The large value of J_3 is attributed to a superexchange mechanism, likely due to favorable orbital overlap and bond angles that enhance hopping integrals via intervening anions. Such unconventional behavior where next-nearest-neighbor exchange interactions are stronger than effective nearest-neighbor interactions have been reported in several other complex systems with strong SOC [81, 82, 83, 84, 85]. We endorse a similar reason where the interplay between strong SOC and different degrees of hybridization for particular Ru-sites within the Ru-trimers is responsible for different competing exchange interactions. The weak but non-negligible inter-trimer exchange interactions (see Table 3.1) further support the development of long-range magnetic order. Overall, our findings emphasize that, in such correlated systems, competing exchange interactions, magnetic anisotropy, and SOC collectively play a decisive role in stabilizing non-collinear magnetic structures. To investigate the ground state of this compound we have fitted the experimental INS spectra using three Gaussian peaks, one Gaussian for the 5.6 meV excitation and two Gaussians for the broad excitation between 10-15 meV, as shown in Fig. 3.6(c). We assign these excitations as transitions from the ground state to excited states at ε_1,ε_2 and ε_3. Further, we have theoretically calculated the spin state and excitation energy by considering only dominant exchange interactions (J_1-J_3) observed in the SpinW models. While the uniaxial anisotropy term D_{zz}, having a magnitude comparable to J_1-J_3, was included in the full SpinW simulations to capture the detailed excitation spectrum, it has been excluded from this analytical model. The goal of presenting this Hamiltonian is to offer a qualitative understanding of the spin dynamics without adding the complexity of anisotropic interactions. A detailed theoretical DFT study may provide further insight into this complex system. A simplified form of the Hamiltonian for the Ru_3O_{12}-trimer is expressed below:

Table 3.1: Intra-trimer and inter-trimer anisotropic exchange interactions obtained from SpinW (negative values for FM and positive values for AFM). The distances are as depicted in Fig. 3.2(b).

Label	Component	Value (meV)
J_1 (intra)	J_{zz}	4.2
J_2 (intra)	J_{xz}	1.8
J_3 (intra)	J_{zx}	4.5
J_4 (inter)	J_{zx}	0.3
J_5 (inter)	J_{zx}	0.1
J_6 (inter)	J_{zx}	-0.06

$$H = J_1(\vec{S}_1 \cdot \vec{S}_2) + J_2(\vec{S}_1 \cdot \vec{S}_3) + J_3(\vec{S}_2 \cdot \vec{S}_3) \tag{3.5.2}$$

The eigenvalues corresponding to this trimer system are given by [86]:

$$\begin{aligned} E(S_{12},S) =& \frac{J_1}{2}\big[S_{12}(S_{12}+1) - S_2(S_2+1) - S_1(S_1+1)\big] \\ &+ \frac{J_2}{2}\big[S(S+1) - S_{12}(S_{12}+1) - S_3(S_3+1)\big] \\ &+ \frac{J_3}{2}\big[S(S+1) - S_2(S_2+1) - S_3(S_3+1)\big] \end{aligned} \tag{3.5.3}$$

Here, S_1, S_2, and S_3 denote the spin operators for Ru1, Ru2, and Ru3, respectively. The spin moments are $\frac{3}{2}$ for Ru1 and Ru2, and 1 for Ru3. Ru1 is located in the middle of the trimer.

To fully characterize the trimer states, we introduce additional quantum numbers, S_{12} and S, which are derived from the vector sums:

$$S_{12} = S_1 + S_2 \quad \text{and} \quad S = S_1 + S_2 + S_3,$$

with constraints:

$$0 \le S_{12} \le 2S_1 \quad \text{and} \quad |S_{12} - S_3| \le S \le S_{12} + S_3$$

The trimer states are defined by the wave functions $|S_{12}, S\rangle$, and their degeneracy is given by $(2S+1)$. By solving this, we get:

$$E(0,1) = -\frac{15J_1}{4} - \frac{15J_3}{8} \tag{3.5.4}$$

$$E(1,0) = -\frac{11J_1}{4} - 2J_2 - \frac{23J_3}{8} \tag{3.5.5}$$

$$E(1,1) = -\frac{11J_1}{4} + J_2 + \frac{J_3}{8} \tag{3.5.6}$$

$$E(1,2) = -11J_1 + J_2 + \frac{J_3}{8} \tag{3.5.7}$$

$$E(2,1) = -\frac{7J_1}{4} - 2J_2 - \frac{23J_3}{8} \tag{3.5.8}$$

$$E(2,2) = -3J_1 - J_2 + \frac{J_3}{8} \tag{3.5.9}$$

$$[E(2,3) = -\frac{7J_1}{4} + J_2 + \frac{J_3}{8}] \tag{3.5.10}$$

$$E(3,2) = -\frac{3J_1}{4} - 2J_2 - \frac{23J_3}{8} \tag{3.5.11}$$

$$E(3,3) = \frac{9J_1}{4} - J_2 + \frac{25J_3}{8} \tag{3.5.12}$$

$$E(3,4) = -\frac{3J_1}{4} + J_2 + \frac{J_3}{8} \tag{3.5.13}$$

We have considered $|3,2\rangle$ as a ground state and by solving the above equation by substituting the J values obtained from spinW, we get the following excited states:

First Excited State:

Transition from $|3,2\rangle \rightarrow |2,2\rangle$

$$\varepsilon_1 = E(2,2) - E(3,2)$$

$$\varepsilon_1 = \frac{7J_1}{4} + 2J_2 + \frac{23J_3}{8} - \left[\frac{3J_1}{4} + 2J_2 + \frac{23J_3}{8}\right]$$

$$\varepsilon_1 = 5.85\,\text{meV}$$

Second Excited State:

Transition from $|3,2\rangle \rightarrow |1,1\rangle$

$$\varepsilon_2 = E(1,1) - E(3,2)$$

$$\varepsilon_2 = 3J_1 + J_2 - \frac{J_3}{8} - \left[\frac{3J_1}{4} + 2J_2 + \frac{23J_3}{8}\right]$$

$$\varepsilon_2 = 10.5\,\text{meV}$$

Third Excited State:

Transition from $|3,2\rangle \rightarrow |2,3\rangle$

$$\varepsilon_3 = E(2,3) - E(3,2)$$

$$\varepsilon_3 = \frac{7J_1}{4} - J_2 - \frac{J_3}{8} - \left[\frac{3J_1}{4} + 2J_2 + \frac{23J_3}{8}\right]$$

$$\varepsilon_3 = 14.7\,\text{meV}$$

Therefore From above calculations, we find that the transition from $|3,2\rangle$ states to $|2,2\rangle$, $|3,2\rangle$ states to $|1,1\rangle$ and $|3,2\rangle$ states to $|2,3\rangle$ corresponds to an excitation energy of 5.85 meV, 10.5 meV and 14.7 meV respectively by following the selection rule $\Delta S = 0, \pm 1$, which is consistent with the observed excitations in the INS spectra depicted in Fig. 3.6(c). The energy level diagram for this trimer state is shown in Fig. 3.6(d) [87]. Hence, the trimer ground state should be characterized as $|3,2\rangle$. In $|3,2\rangle$, S=2 is the ground state of Ru-trimers, which represents the total spin moment of the Ru_3O_{12} trimers. Using this, we have calculated the magnetic moment $4\,\mu_B$ and the effective magnetic moment to be $4.89\,\mu_B$, which agrees with experimentally obtained magnetic moment from Neutron diffraction results and effective moment from magnetic susceptibility [76]. Therefore, we conclude that the observed spin-excitation is restricted to Ru_3O_{12} -trimers.

3.5.3 Origin of Excitation at High-|Q| region probed by INS and MLFF

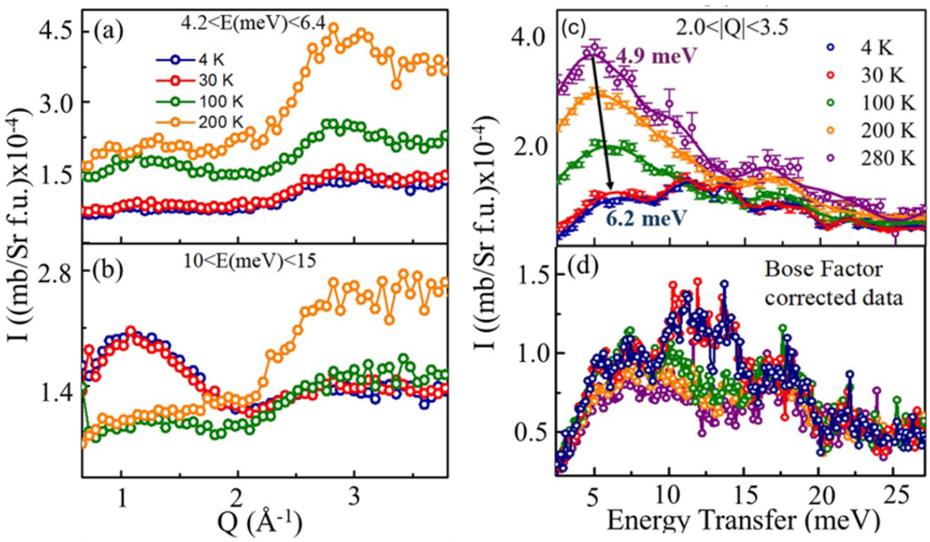

Figure 3.7: Intensity vs momentum transfer at Fixed Energy (a) E=10 - 15 meV (b) 4.2 - 6.4 meV and The |Q|- integrated, Intensity vs momentum transfer of (c) Raw data at 4 K - 280 K that shows the 5.6 meV peak shift with temperature, (d) Bose factor normalized data at 4 K - 280 K

Our earlier discussion primarily focused on the low-|Q| region, a closer inspection of the high-|Q| region in Fig. 3.3(a-e) reveals intriguing features. Notably, excitations at a similar energy range as the low-|Q| magnetic scattering are clearly visible even at high-|Q|. To explore this, we plotted the intensity vs |Q| across the full-|Q| range for two selected energy regions around 5.6 meV and between 10-15 meV shown in Fig. 3.7(a-b). At low |Q| (<1.5 Å^{-1}), the intensity decreases with increasing |Q|, which is consistent with magnetic excitations, as the magnetic form factor reduces with increasing |Q|. However, at higher |Q|, the scattering intensity increases proportional to Q^2, consistent with a phonon cross-section. This suggests that phonons begin to dominate for |Q|> 2 Å^{-1}.

In Fig. 3.7(c) energy cuts at high |Q| (2< |Q|< 3.5) has been shown across various temperatures that suggest the presence of 5.6 meV at high- |Q|. However, the temperature dependent scattering intensity is difficult to interpret. As seen in Fig. 3.7(c) the peak at larger momentum transfer softens as a function of temperature from 6.2 meV at 4K to 4.9 meV at 280 K. Such behavior could be attributed to phonon softening above the magnetic ordering temperature due to electron-phonon coupling, which might be influenced by changes in the electronic correlations around magnetic transition, or due to magnon-phonon coupling, as reported in many other systems, such as, $YMnO_3$, $Sr_{14}Cu_{24}O_{41}$ and $CaMn_7O_{12}$ compounds [23, 88, 89]. This phonon softening can be parameterized by the relation:

$$\omega_{\text{phonon}} = \omega_0 + \lambda S(Q,T) \tag{3.5.14}$$

where ω_{phonon} is the modified phonon frequency due to spin-phonon coupling, ω_0 is the uncoupled phonon frequency, λ is the spin-phonon coupling constant, and S(Q,T) is the spin correlation function, which depends on temperature and momentum. However, such a shift could also be a consequence of the change in spectrum due to thermal population effects over the large range of temperatures examined. To consider this, we have plotted the Bose factor normalized data in Fig. 3.7(d). We find that the spectral weight as shown in Fig. 3.7(d) does not shift significantly with temperature, excluding the possibility of magnon-phonon coupling being observed from these measurements.

To clarify the role of phonon, we have performed phonon calculations based on the published crystal structure [76]. The calculated phonon modes shown in Fig. 3.8 span up to approximately 22 THz (approximately 91 meV) with no indication of negative phonon energies. We have also used this calculated spectrum in the INSPIRED software to calculate the powder averaged neutron scattering intensity convolved with the instrumental energy and momentum resolution. This calculation also included multiple phonon processes and temperature dependent thermal population of phonon. We present these results in Fig. 3.9 for both scattering intensity and Bose factor normalized scattering intensity for T=4 K and T=280 K. These calculations provide a good characterization of the extent of the observed phonon scattering in the measurement. The range of momentum transfers

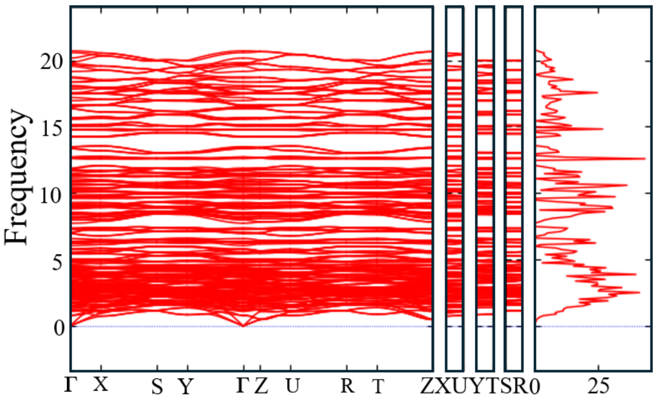

Figure 3.8: Calculated phonon modes for $Ba_5Ru_3O_{12}$ based upon pre-trained machine learning force fields as described in the main text. Vertical axis is the phonon energy in units of THz. (1 THz = 4.136 meV). Panels indicate wave-vector dependence in reciprocal space using standard reciprocal space coordinates for the orthorhombic crystal structure. The panel on the far right is the density of states (horizontal axis) as a function of energy transfer (vertical axis).

used to characterize magnetic scattering, $0.5 < |Q| < 1.5$ Å^{-1}, is shown to have a small phonon scattering contribution at high temperatures. Likewise, these calculations provide additional clarity regarding the relative scattering intensity and Bose factor normalized intensity of the phonon contribution as a function of momentum transfer in the range of larger momentum transfer, $2 < |Q| < 3.5$ Å^{-1}, which suggest the existance of phonon in the higher momentum transfer region that overlap significantly with the magnetic excitations we have characterized at smaller momentum transfer.

On the other hand, to gain further insight of magnon, we have plotted the Bose factor corrected intensity for the momentum transfer range of $0.5 < |Q| < 1.5$ Å^{-1} in Fig. 3.10(a) and $2 < |Q| < 3.5$ Å^{-1} in Fig. 3.10(b). This treatment of the data allows us to observe the proposed magnetic excitations around 10-15 meV for T= 4 K and 30 K at high-|Q| region of the spectrum (Fig. 3.10(b)).The low-energy (5.6 meV) excitation is weaker in intensity but clearly visible. The presence of magnetic scattering in this range of larger values of momentum transfer is likely due to the extended range of the Ru^{4+} magnetic form-factor. In order to investigate whether the high-|Q| excitations arise solely from phonons or include a magnetic contribution, we calculated the magnetic form factor for Ru as a function of momentum transfer using standard analytical expressions for $4d$ transition metals (see Fig. 3.10(c)) [90]. By comparing the intensity ratios between low and high |Q| regions in the Bose factor corrected data (See Fig. 3.10(a-b)), we find that

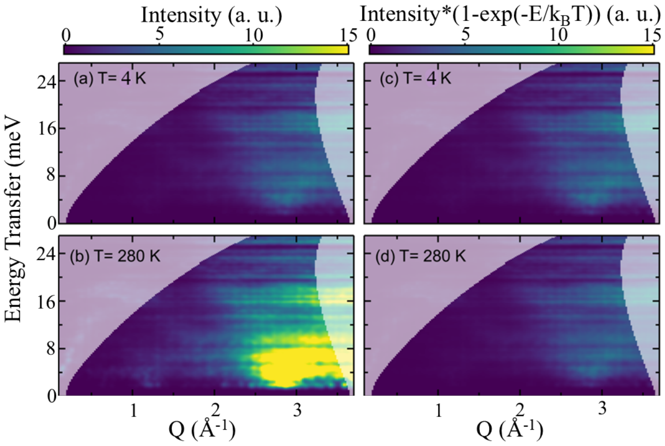

Figure 3.9: Calculated phonon scattering intensity (a)-(b) and Bose factor normalized scattering intensity (c)-(d) for $Ba_5Ru_3O_{12}$. The neutron scattering intensity was convolved with the calculated instrumental energy resolution for the E_i =30 meV measurements. The wave-vector resolution was determined from the width of the aluminum nuclear Bragg peaks measured in the empty can measurements. The calculation was also convolved with this determined wave-vector resolution. All panels are shown in the same intensity scale. The lightly shaded regions are outside of the measured range of energy and wave-vector transfer allowed from the kinematic constraints and the detector coverage of the instrument.

at $|Q| \approx 3.5$ Å^{-1}, only about $\sim 3.9\%$ of the magnetic form factor remains. To better understand this behavior, we have taken the average value of $|F(Q)|^2$ for low |Q| (0.5-1.5 Å^{-1}) and high |Q| (2< |Q|< 3.5) range, which is 0.7652 and 0.1944 respectively. Using this , we have estimated the expected magnetic intensity at high |Q|:

$$I_{\text{high}\,Q} = I_{\text{low}\,Q}\left(\frac{|F(Q)_{\text{high}_{\text{avg}}}|^2}{|F(Q)_{\text{low}_{\text{avg}}}|^2}\right) \tag{3.5.15}$$

Substituting the observed values (from Fig. 3.3(d) and Fig. 3.10(a)):

$$\begin{aligned} I_{\text{high}\,Q} &= 2.32 \times 10^{-4} \times \frac{0.1944}{0.7652} \\ &\approx 0.59 \times 10^{-4} \end{aligned} \tag{3.5.16}$$

This value nearly agrees with the experimental intensity of 0.67 x 10^{-4} observed for 10-15 meV excitation in Fig. 3.10(b) after Bose factor correction. This result supports that the high-|Q| feature at 10-15 meV is of magnetic origin, and likely due to the range of the magnetic form factor of the Ru ion.

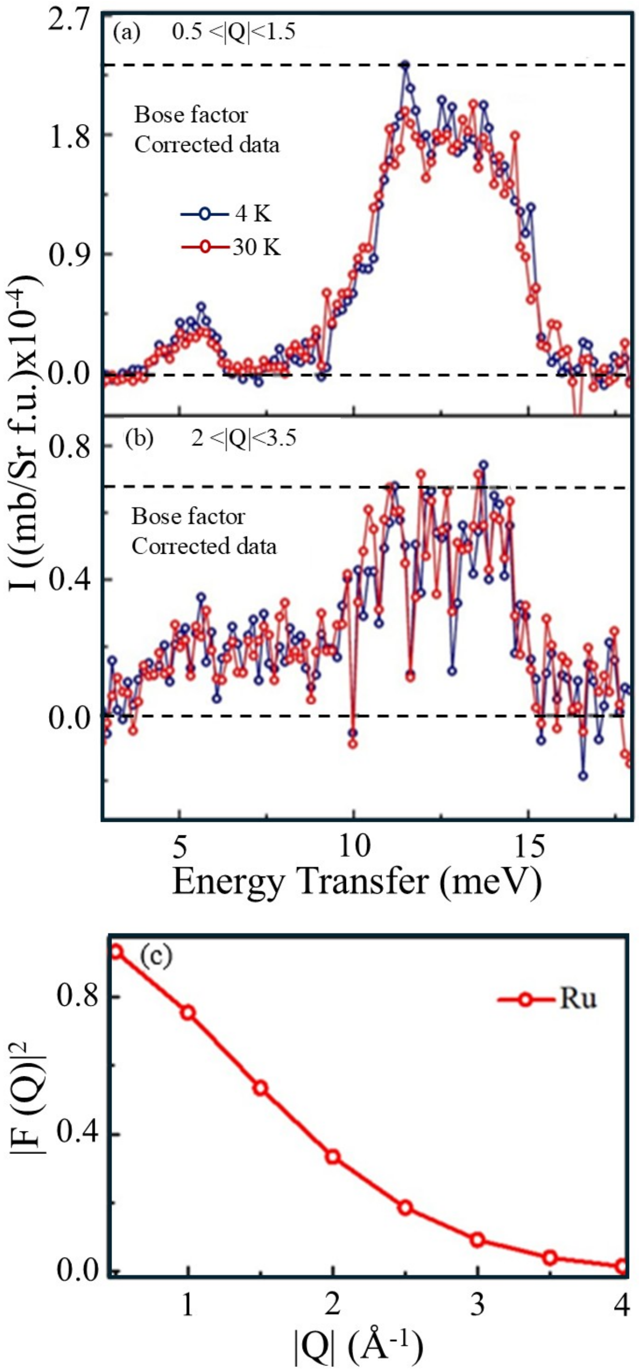

Figure 3.10: Bose factor corrected INS spectra (a) at low-|Q| range (0.5< |Q|< 1.5), showing strong magnetic excitation near 5-15 meV at 4 K and 30 K. The horizontal dashed line indicates the maximum intensity used for scaling to high-|Q|. (b)at high-|Q| range (2< |Q|< 3.5). The dashed line denotes the maximum magnetic intensity estimated by scaling the low-|Q| value. (c) Squared magnetic form factor $|F(Q)|^2$ for Ru as a function of momentum transfer |Q|, calculated using standard analytical expressions for $4d$transition metals.

We do note that our phonon calculations indicate the presence of a large phonon density of states in the vicinity of the higher energy magnetic mode. A thorough single crystal INS measurement along with additional phonon calculations to understand which modes involve the Ru-sites in the crystal structure would help to quantify any signature of spin-phonon coupling.

3.6 Conclusions

Here, we have documented the spin-wave excitation of the Ru-trimer system, $Ba_5Ru_3O_{12}$ through INS. The SpinW simulation replicates the experimental spin-structure and spin-excitations, revealing the various competing magnetic exchange interactions that play a decisive role in the magnetism of this trimer Ruthenate. Our results suggest a strong electronic correlation of Ru and possible spin-phonon coupling. The presence of INS spectra far above magnetic ordering manifests short-range correlation arising from isolated Ru-trimer. Finally, we conclude octahedral distortion and the exchange frustration govern a unique ground state for each Ru within the Ru-trimer and yield a non-collinear spin-structure, unlike all other Ruthenates belonging to nearly the same family. A small perturbation could tune the local structure and hybridization and control the magnetic ground state of ruthenium.

Chapter 4

Ground state of 6H perovskite $Ba_3HoRu_2O_9$, Origin of spin-driven ferroelectricity, spin and CEF excitations

4.1 Motivation

The spin-driven ferroelectricity and magneto(di)electric (MDE) coupling is mostly reported in $3d$-transition-metal-oxides where the spin-pattern of $3d$-metal ions is responsible to break the spatial inversion symmetry and create dielectric polarization. It is theoretically predicted that the strong spin-orbit coupling of larger d-orbital ($4d$/5d) might have pronounced effect on magnetoelectric (ME) coupling [12]. However, the experimental demonstration of ME coupling is rarely reported in any $4d$/5d-metal (magnetic) based compounds [91]. Very recent, MDE coupling and multiferroicity is reported in 6H-perovskite $Ba_3RRu_2O_9$where role of $4d$-$4f$ coupling is predicted [92]. Though, the mechanism of such coupling, and moreover, mechanism of spin-driven ferroelectricity in this system is not yet understood. Here, we aim to understand the mechanism of spin-driven ferroelectricity and role of $4d$-$4f$ coupling on it. The present Chapter deals with the detail understanding of the spin-driven ferroelectricity of a prototype $4d$-$4f$ compound $Ba_3HoRu_2O_9$. Here we present a systematic calculation of ferroelectric polarization employing inverse D-M interaction [$P_{ij} \propto \mathbf{e}_{ij} \times (\mathbf{S}_i \times \mathbf{S}_j)$] from our experimental results. We demonstrate that the non-colinear structure involving two different magnetic ions, Ru($4d$)

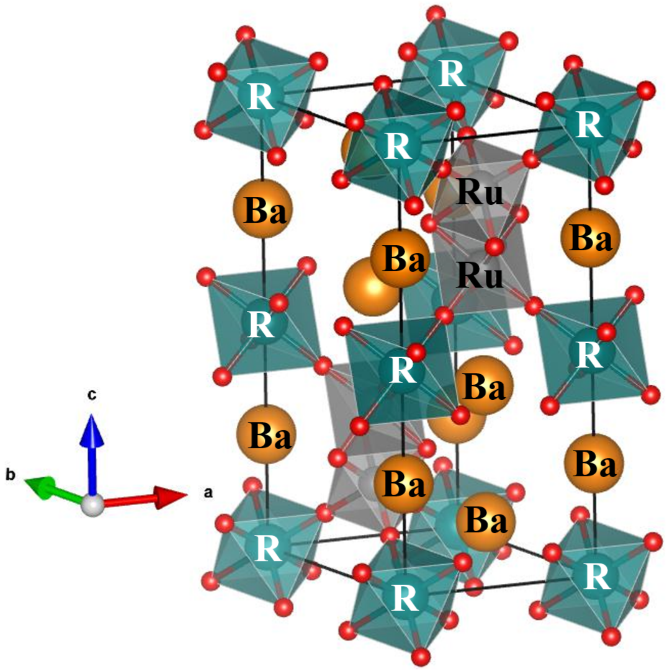

Figure 4.1: Crystal Structure of $Ba_3RRu_2O_9$.

and Ho(4*f*), breaks the spatial inversion symmetry due to off-centric displacement of oxygen atoms via inverse D-M interaction through strong 4*d*-4*f* magnetic correlation, which results in non-zero polarization. Such a mechanism is rarely reported in literature and opens a new direction to explore spin-driven ferroelectricity.

4.2 Introduction: A brief overview of 6H-perovskite $Ba_3RRu_2O_9$

The 6*H* perovskite oxide system, $Ba_3RRu_2O_9$ (M = Bi, 3*d*-transition metal, Y, La, rare-earth ion), crystallizing in a hexagonal structure (with space group $P6_3/mmc$, No. 194), is a current research focus due to its versatile magnetic ground state resulting from strong M-Ru correlations [46, 56, 57, 58, 59, 60, 61, 91, 92]. The crystal structure of the $Ba_3RRu_2O_9$ system is illustrated in Fig. 4.1.

In this crystal structure, two distorted face-sharing RuO_6 octahedra form a Ru_2O_9 dimer, which are connected through corner-sharing RO_6 octahedra. The magnetic behavior of the Ru_2O_9 dimer is of great interest due to the very short Ru-Ru distance (2.52 Å) within the dimer, which is expected to lead to strong magnetic interactions between the Ru ions, resulting in the formation of a magnetic dimer. For non-magnetic ions (e.g.

Bi, Zn, Y, La), the system is characterized as a magnetic dimer compound [59, 60, 61]. Replacing non-magnetic M-ion by a magnetic metal ion develops long-range magnetic ordering via the Ru($4d$)-O-M($3d$) super-exchange path. The valence state of Ru varies from +4 to +5 depending on the M-ion. The bivalent metal ion (e.g. Co^{2+}, Mn^{2+}, Ni^{2+}) yields a Ru^{3+} ($4d^3$) ground state. Interestingly, the compound $Ba_3BiRu_2O_9$ exhibits an unconventional Bi^{4+} valence state [93]. If the M-ion is replaced by $Y^{3+}/La^{3+}/R^{3+}$ (R = rare-earth ion), the Ru possesses an average +4 valance state within Ru_2O_9 dimer. A strong dimmer ordering is observed for the compound $Ba_3YRu_2O_9$ and $Ba_3LaRu_2O_9$, showing a broad hump in temperature dependent susceptibility around 200-300 K [59, 61].

Interestingly, even though the magnetic behavior is nearly the same in bulk susceptibility, INS studies on these two systems reveal different magnetic ground states of the ruthenium dimer. $Ba_3YRu_2O_9$ exhibits an $S = 1/2$ dimer state through strong metal-metal bonding of Ru, whereas the $Ba_3LaRu_2O_9$ compound (La has a larger radius than Y) yields an $S = 3/2$ ground state [59, 61]. The replacement of R^{3+} magnetic ions develops long-range ordering in this system at low temperatures around 10 K. The magnetic ground state is quite intriguing for different R-ions. For the compound $Ba_3NdRu_2O_9$, Nd moments order ferromagnetically at $\sim$ 24 K, followed by another magnetic phase transition where Ru moments order antiferromagnetically [58]. This is in sharp contrast with all other R members in this series, which order antiferromagnetically. Probably hybridization plays an important role in these systems. In this family, Ce and Tb show a +4 valence state yielding $Ru_2^{4+}O_9$ dimers, unlike other rare-earth members. A non-magnetic excited ground state and the possibility of molecular-type magnetism is predicted for the compound $Ba_3CeRu_2O_9$ [60]. The compound $Ba_3SmRu_2O_9$ shows a broad hump at $\sim$ 200 K as a characteristic of magnetic low-dimensional behavior similar to the La/Y members, followed by magnetic ordering at 10 K. The Gd, Tb, and Ho members are reported to exhibit two magnetic anomalies in some recent reports [56, 92], in contrast to earlier reports, although the nature of the magnetic ordering has not yet been revealed.

The introduction of rare-earth ions not only introduces long-range ordering but also enhances the insulating nature of this system due to the atomic nature of the R ions, which makes this system ideal for studying MDE coupling and multiferroicity. A preliminary study on this aspect revealed that this system is a good candidate to exhibit MDE coupling [91, 92]. A systematic investigation on $Ba_3RRu_2O_9$ (for R = Nd, Sm, Tb, Ho) confirms that MDE coupling enhances with increasing magnetic moment of the rare-earth ion [91, 92]. Therefore, the study reveals that the heavy rare-earth members in this family are good

Table 4.1: Valence state, ionic radius (r), effective magnetic moment, and ordering temperature (T_N or T_C) of rare-earth (R) ions in $Ba_3RRu_2O_9$.

R-ion	**Valence**	**r(Å)**	μ_{eff} (μ_B)	**T_N or T_C**
La	+3	-	0	-
Ce	+4	0.87	0	No
Pr	+4	1.13	2.54	10.5 K
Nd	+3	1.11	3.62	25 K and 17 K
Sm	+3	1.08	0.845	11 K
Eu	+3	1.07	0	8 K
Gd	+3	1.05	7.94	14.8 K
Tb	+4	0.90	7.94	9.5 K
Dy	+3	1.03	10.63	5.8 K
Ho	+3	1.02	10.6	10.2 K and 50 K
Er	+3	1.00	9.6	6 K
Tm	+3	-	7.57	-
Yb	+3	0.99	4.54	4.5 K

candidates for MDE coupling. A weak ferroelectricity is reported only for $Ba_3HoRu_2O_9$. However, no spin-driven ferroelectricity is documented for this compound.

The compelling effects of ionic radius (localization/hybridization), crystal-electric field, spin-orbit coupling, and magnetic moments play a crucial role in determining the magnetic and MDE behavior.

On the basis of the rare-earth element (R), the table for magnetic moment, ionic radius, ordering temperature, and their valence state is given below.

For Ru-O, there are two oxygen atoms present in the crystal structure of $Ba_3RRu_2O_9$. The first oxygen atoms (O1) are on the face-shared position in the Ru_2O_9 dimer, while the second oxygen atoms (O2) are on the top or bottom face of the Ru_2O_9 dimer (see Fig. 4.2). The bond length between Ru-O1 is 2.002-2.046 Å and Ru-O2 is 1.908-1.982 Å, indicating that the two octahedra in this Ru_2O_9 dimer are distorted. The Ru-O1 length increases with increasing the ionic radius of R-ion, while the Ru-O2 length decreases; such a tendency clearly indicates that the shape of Ru_2O_9 dimers becomes more distorted with increasing the ionic radius of R-ion.

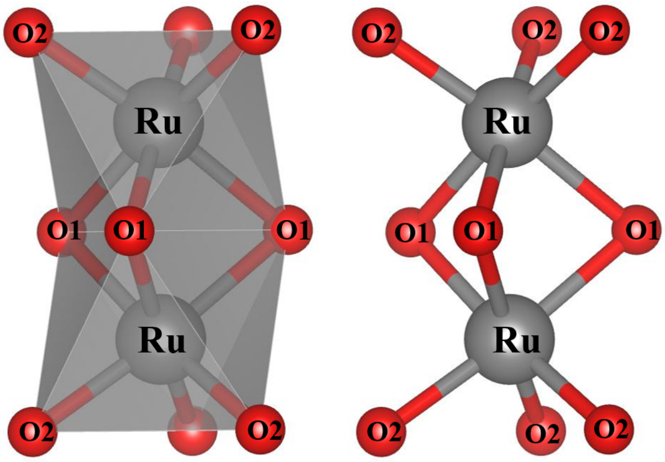

Figure 4.2: Ru_2O_9 dimers

4.3 An overview of $Ba_3HoRu_2O_9$

The compound $Ba_3HoRu_2O_9$ undergoes an antiferromagnetic ordering at $T_{N2} \sim 10.2$ K. The magnetic super-exchange interaction develops through the path "Ru-O-Ho-O-Ru" (Fig. 4.3). Among all the known compositions, $Ba_3HoRu_2O_9$ exhibits the strongest MDE coupling and shows ferroelectricity with a weak polarization value below the magnetic ordering (10.2 K) [92], Doi et al. Recent neutron diffraction studies [92] on this system reveal that the compound $Ba_3HoRu_2O_9$ magnetically orders at much higher temperature compared to the reported one, which is $T_{N1} = 50$ K, followed by another magnetic phase transition ~ 10.2 K (T_{N2}). It is also documented that both Ho and Ru-moments starts to orders below T_{N1}. In most of the d-f systems, it is observed that first spin-moments of d-orbital (delocalized orbital) orders and f-moments (f-orbitals are localized in nature) orders at further low temperature. Hence, $Ba_3HoRu_2O_9$ is considered to be a unique system where cooperative $4d$-$4f$ magnetic ordering is observed, probably resulting from strong $4d$-$4f$ coupling. The spin-arrangement below T_{N1} is associated with a propagation propagation vector of $K_1 = (0.5\ 0\ 0)$, whereas the spin-pattern below T_{N2} is more complex and associated with two magnetic propagation vector, $K_1 = (0.5\ 0\ 0)$ and $K_2 = (0.25\ 0.25\ 0)$. A gradual spin reorientation of Ho and Ru spin-moments are observed with decreasing temperature below T_{N1}[92]. The 2nd magnetic phase belwo T_{N2} is characterized by two competing magnetic ground state, one is canted spin-structure associated with K_1, and another is an up-up-down-down ($\uparrow\uparrow\downarrow\downarrow$) spin-structure of each Ru and Ho-spins in ab-plane. The compound exhibits a peak in the T-dependent complex dielectric constant at the onset of the 2nd magnetic phase transition (T_{N2}) which has a pronounced effect in the presence of a magnetic field, mimicking the magnetic feature observed in magnetic susceptibility and heat capacity [92]. Further, positive-up-negative-down (PUND) ferroelectric polarization measurements at 5 K (below T_{N2}) confirm the ferroelectricity characterizing this compound as multiferroic [92]. The precise mechanism, that is, how spin drives the ferroelectric polarization, remains unclear. We have elucidated the mechanism in detail through synchrotron XRD, time-of-flight neutron diffraction and theoretical calculations. The competing magnetic ground state often stabilizes under application of external parameters, such as, magnetic field, pressure. Here we have studied the magnetization and neutron diffraction under external magnetic field to understand the ground state of the system. In this work, we have also presented a detailed INS study of $Ba_3HoRu_2O_9$, Combining with SpinW simulation, Raman spectroscopy and Machine learned force field calculation, which enables a comprehensive understanding of microscopic origin of magnetic excitation, Ho^{3+} CEF and the role of exchange interaction, anisotropy, spin-lattice-orbital coupling in complex oxides that provide new insight into how molecular magnetism, rare-earth anisotropy, and lattice dynamics intertwine in $4d$-$4f$ oxides. This study is motivated by the absence of inelastic neutron scattering investigations on $4d$-$4f$ systems with a magnetic rare-earth ion, where strong $4d$-$4f$ coupling is expected to produce unconventional magnetic excitations that are not accessible in systems with nonmagnetic rare-earth counterparts.

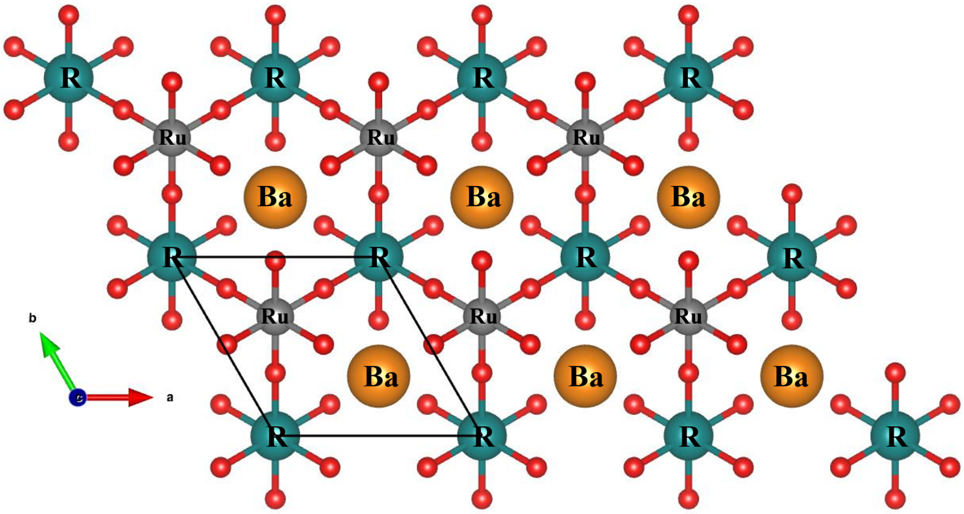

Figure 4.3: Ru-O-R-O-Ru super exchange path where R= Nd,Sm,Ho,Tb

4.4 Experimental Details

The powder sample $Ba_3HoRu_2O_9$ was synthesized by solid-state-reaction using high purity (>99.9%) precursors: $BaCO_3$, RuO_2, and Ho_2O_3. These precursors were thoroughly mixed in an agate mortar and pestle, pressed into pellets, and subjected to a multi-step heating process. Initially, the pellets were heated at 900°C for 12 hours, followed by repeated cycles of grinding, repalletizing, and heating first at 1000°C for 24 hours and then at 1150°C for 24 hours to ensure phase purity and homogeneity [56, 92]. The compound forms a single phase with P63/mmc space group as reported earlier[56, 92]. Temperature-dependent AC magnetic susceptibility measurements were carried out using a Quantum Design Superconducting Quantum Interference Device (SQUID). The high-pressure SQUID measurement was done using a beryllium copper homemade clamp-style cell in Oak Ridge National Laboratory (ORNL). The sample magnetization is calculated by subtracting the empty pressure cell data. The ambient pressure (standard sample loading) dc magnetization is conducted in the presence of 100 Oe-50 kOe magnetic field in zero-field-cooled (ZFC) mode (the sample is cooled under zero field from paramagnetic region to 2K and then the magnetic field is applied, the data has been taken during warming) and after that, the dc magnetization is taken under 10 kOe magnetic field applying different pressure (0-1.2 GPa) in the same ZFC mode. The complex dielectric measurements as a function of temperature, magnetic field, and frequency (1 V AC bias, 1-100 kHz) were performed using an LCR meter (Agilent 4284A). This measurement set-up is integrated into a Quantum Design Physical Properties Measurement System (PPMS). Silver paint was used to make parallel-plate capacitors of the pressed disc-like polycrystalline samples. Neutron Powder diffraction patterns were collected at the SNAP beamline, a time-of-flight diffractometer dedicated to high-pressure research at Spallation Neutron Source (SNS), Oak Ridge Laboratory, USA. To cover the regions of interest in reciprocal space the detector banks were placed at a central scattering angle of 50° and 65° about the sample in the scattering plane (each spanning a 45° range) and two central wavelengths selected were 2.4 Å and 6.4 Å, leading to an incident beam with usable wavelength spectra of 0.65 Å to 4.15 Å, and 4.65 Å to 8.15 Å (second frame). The resulting diffraction data covered a range, in momentum transfer q from 0.9 -10 $Å^{-1}$ or, in d spacing from $0.5 \text{ Å} < d < 7 \text{ Å}$. In the second frame, the corresponding ranges are momentum transfer q from 0.4-1.8 $Å^{-1}$ or, in d spacing from $3.5 \text{ Å} < d < 12 \text{ Å}$. The available low-$Q$ range in time-of-flight neutron diffraction measurement will be able to track any other magnetic peak (if appears) for both propagation vectors K_1 and K_2.

The sample was placed in a liquid He cooled wet "orange" cryostat and data were collected from room temperature down to 4 K. Two sets of measurements were attempted: one at ambient pressure where the sample was loaded on a thin walled 6 mm diameter vanadium can and another set using a high strength CuBe clamp pressure cell with 10 mm in diameter. Initial analysis indicated that the elevated background levels of the relatively smaller amounts of sample measured and the weak magnetic scattering in the pressure cell precluded the tracking of the magnetic phases with pressure. As such in the following, only the ambient pressure data is presented.

We have carried out the temperature dependence high-resolution X-ray diffraction (HRXRD) in CRISTAL beamline in SOLEIL synchrotron (France) with an X-ray source of wavelength $\lambda = 0.58182$ Å.

INS measurements were performed on the MARI time-of-flight spectrometer at the ISIS Neutron and Muon Source (UK) [69]. Approximately 3.8 g of powder sample was sealed in a thin-walled aluminium can and mounted in a closed-cycle refrigerator. Measurements were conducted using incident neutron energies $E_i = 11.7$, 29.7, and 180 meV to comprehensively cover low-energy magnetic excitations, crystal-field transitions, and lattice dynamics. Data were collected at temperatures of 1.8 K, 30 K, 100 K, and 300 K, spanning both magnetically ordered phases and the paramagnetic regime. Standard corrections for detector efficiency, background scattering, and Bose population factors were applied using the Mantid and DAVE software packages[94].

Raman spectroscopy measurements were carried out at room temperature using a 532 nm excitation source with a spectral resolution of 1 cm^{-1} at the Central Instrumentation Facility (CIF), RGIPT.

To interpret the magnetic excitation spectrum, linear spin-wave calculations were performed using the SpinW package [67]. The experimentally determined magnetic structures and crystallographic parameters were used as input, and symmetry-allowed exchange pathways were systematically explored to reproduce the observed INS spectra. Lattice dynamics were modeled using MLFF phonon calculations, enabling efficient computation of phonon dispersions and powder-averaged neutron scattering intensities for direct comparison with experiment [68, 69].

4.5 Result and Discussion

4.5.1 Investigation of magnetic ground state through TOF Neutron diffraction

We have performed the Time-of-flight neutron diffraction at SNAP for the two wavelength range 0.5–3.65 Å and 3.7–6.5 Å, which allow us to measure the wide-Q range to detect all the magnetic peaks. Fig. 4.4 presents the Time-of-Flight (TOF) data over a temperature range of 4–120 K in which suggest magnetic peaks become evident around 20 K, and as the temperature further decreases to 4 K, additional magnetic peaks are observed. Fig. 4.4(b) shows the neutron TOF data for the wavelength range 3.7-6.5 Å that corresponds to the low-|Q| region, where a large number of magnetic peaks are observed compared to Figure 4.4(a).

We have refined the 80 K data for both the wavelength range using the reported $P6_3$/mmc space group as shown in Figure 4.5(a-b), which confirm the single-phase of the material.

In Fig. 4.4(b) an extra magnetic peak is observed between the temperature range $T_{N2} < T < T_{N1}$ that corresponds to (0 0 2) Bragg's position. In previous NPD study of $Ba_3HoRu_2O_9$ the data is fitted using two wave vector, $K_1 = (0.5, 0, 0)$ for temperature range $T_{N2} < T < T_{N1}$ and below T_{N2} it is characterized by the $K_2 = (2.5, 2.5, 0)$ along with the K_1 propagation vector [62]. By performing K search we get the same propagation vector (0.5 0 0) for the intermediate temperatures.

In this system, there are two magnetic atoms, Ho and Ru, having Wyckoff positions $2a$ (0 0 0) and $4f$ (0.33333, 0.66667, 0.16250), respectively. We did the irreducible representational analysis through the SARAh program. The irreducible representations (I.R.) and basis vectors (B.V.) of the Ru spins for the $P6_3/mmc$ space group associated with the propagation vector are shown in Tables 4.2 and 4.3.

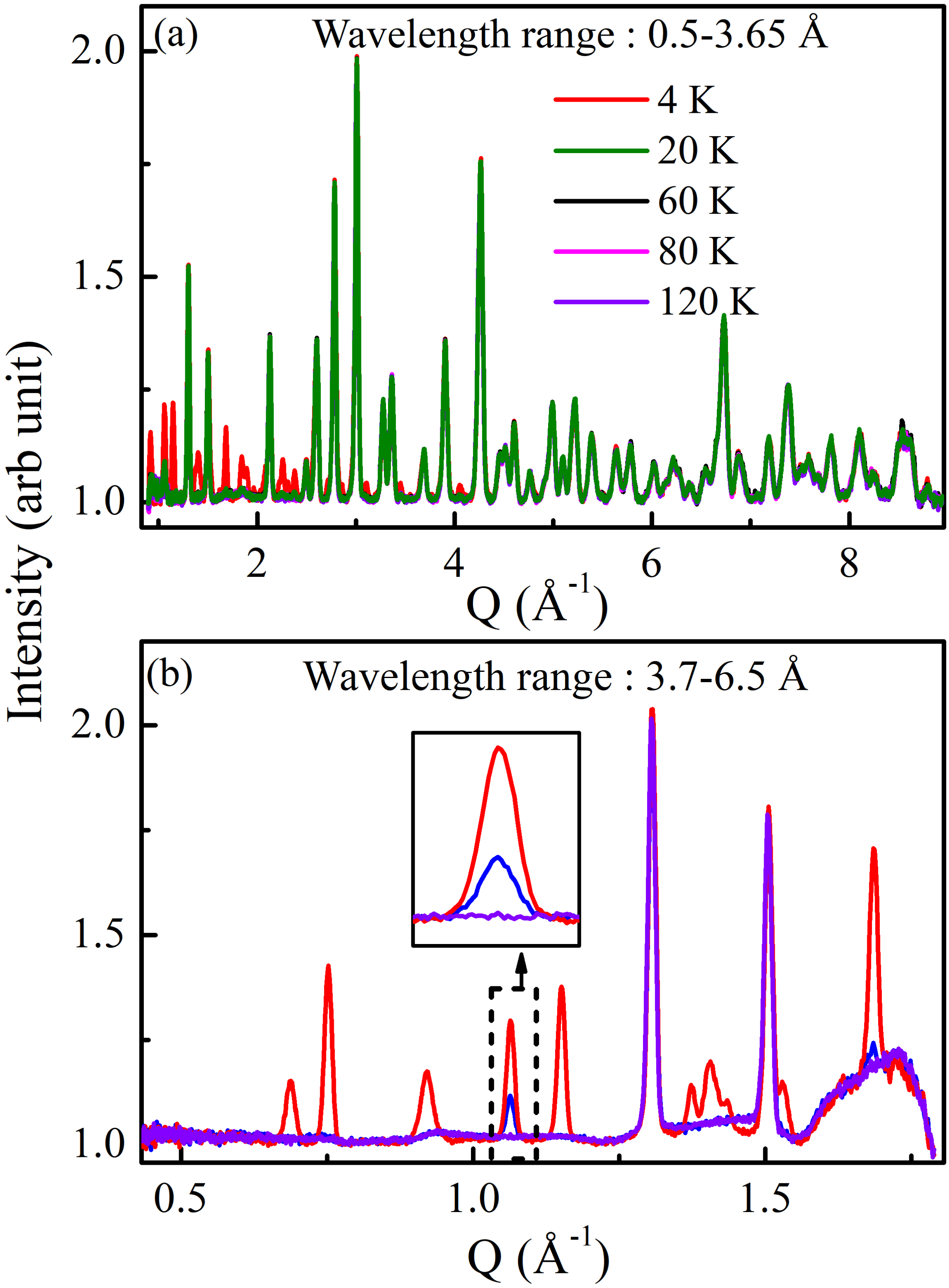

Figure 4.4: Neutron time-of-flight data over temperature range of 4 K-120 K having wavelength range (a) 0.5-3.65 Å and (b) 3.7-6.5 Å.

Table 4.2: Basis vectors for the space group $P6_3/mmc$ with propagation vector $\mathbf{K}$ = (0.5 0 0). Irreducible representations for the magnetic Ru site (0.66667 0.33333 0.16250) obtained using the SARAh program.

IR	**BV**	**Atom**	**BV components**					
			$m \parallel a$	$m \parallel b$	$m \parallel c$	$im \parallel a$	$im \parallel b$	$im \parallel c$
Γ_1	ψ_1	1	0	-1	0	0	0	0
		2	0	-1	0	0	0	0
		3	0	1	0	0	0	0
		4	0	1	0	0	0	0
Γ_2	ψ_2	1	2	1	0	0	0	0
		2	2	1	0	0	0	0
		3	2	1	0	0	0	0
		4	2	1	0	0	0	0
	ψ_3	1	0	0	2	0	0	0
		2	0	0	-2	0	0	0
		3	0	0	2	0	0	0
		4	0	0	-2	0	0	0
Γ_3	ψ_4	1	2	1	0	0	0	0
		2	2	1	0	0	0	0
		3	-2	-1	0	0	0	0
		4	-2	-1	0	0	0	0
	ψ_5	1	0	0	2	0	0	0
		2	0	0	-2	0	0	0
		3	0	0	-2	0	0	0
		4	0	0	2	0	0	0
	ψ_6	1	0	-1	0	0	0	0
		2	0	-1	0	0	0	0
		3	0	-1	0	0	0	0
		4	0	-1	0	0	0	0

IR	**BV**	**Atom**	**BV components**					
			$m \parallel a$	$m \parallel b$	$m \parallel c$	$im \parallel a$	$im \parallel b$	$im \parallel c$
Γ_4	ψ_7	1	0	1	0	0	0	0
		2	0	1	0	0	0	0
		3	0	-1	0	0	0	0
		4	0	-1	0	0	0	0
Γ_5	ψ_8	1	2	1	0	0	0	0
		2	-2	-1	0	0	0	0
		3	2	1	0	0	0	0
		4	-2	-1	0	0	0	0
Γ_6	ψ_9	1	0	0	2	0	0	0
		2	0	0	2	0	0	0
		3	0	0	2	0	0	0
		4	0	0	2	0	0	0
Γ_7	ψ_{10}	1	2	1	0	0	0	0
		2	-2	-1	0	0	0	0
		3	-2	-1	0	0	0	0
		4	2	1	0	0	0	0
	ψ_{11}	1	0	0	2	0	0	0
		2	0	0	2	0	0	0
		3	0	0	-2	0	0	0
		4	0	0	-2	0	0	0
Γ_8	ψ_{12}	1	0	-1	0	0	0	0
		2	0	1	0	0	0	0
		3	0	-1	0	0	0	0
		4	0	1	0	0	0	0

From Table 4.2 and 4.3 we can see that Ho and Ru atoms have have four and eight possible irreducible representations respectively, described as

Table 4.3: Basis vector for the space group $P6_3/mmc$ for $K = (0.5\ 0\ 0)$. The irreducible representation for magnetic site Ho (0 0 0), as obtained from SARAh program.

IR	BV	Atom	BV components					
			$m_{\parallel a}$	$m_{\parallel b}$	$m_{\parallel c}$	$im_{\parallel a}$	$im_{\parallel b}$	$im_{\parallel c}$
Γ_1	ψ_1	1	0	−2	0	0	0	0
		2	0	2	0	0	0	0
Γ_3	ψ_2	1	4	2	0	0	0	0
		2	−4	−2	0	0	0	0
	ψ_3	1	0	0	4	0	0	0
		2	0	0	4	0	0	0
Γ_5	ψ_4	1	0	−2	0	0	0	0
		2	0	−2	0	0	0	0
Γ_7	ψ_5	1	4	2	0	0	0	0
		2	4	2	0	0	0	0
	ψ_6	1	0	0	4	0	0	0
		2	0	0	−4	0	0	0

$$\Gamma_{\text{mag}}(\text{Ru}) = 1\Gamma_1^1 + 2\Gamma_2^1 + 2\Gamma_3^1 + 1\Gamma_4^1 + 1\Gamma_5^1 + 1\Gamma_6^1 + 2\Gamma_7^1 + 1\Gamma_8^1$$

$$\Gamma_{\text{mag}}(\text{Ho}) = 1\Gamma_1^1 + 2\Gamma_3^1 + 1\Gamma_5^1 + 2\Gamma_7^1$$

Since both Ho and Ru atoms exhibit magnetic ordering, their magnetic structures must be associated with one or a combination of the $\Gamma_1, \Gamma_3, \Gamma_5$ and Γ_7 representations. Among these, the Γ_7 provides the best agreement with the experimental data. Rietveld refinement of 20 K TOF data having K_1 propagation vector and both the wavelength range is shown in Fig. 4.5(c–d). Upon cooling below T_{N2}, the emergence of additional magnetic Bragg peaks suggests a more complex magnetic structure that corresponds to propagation vector K_2 (0.25 0.25 0) which coexist with K_1 = (0.5 0 0), indicating the presence of two distinct magnetic phases. The irreducible representations correspond to K_2 propagation vector are given in Table 4.4 and 4.5.

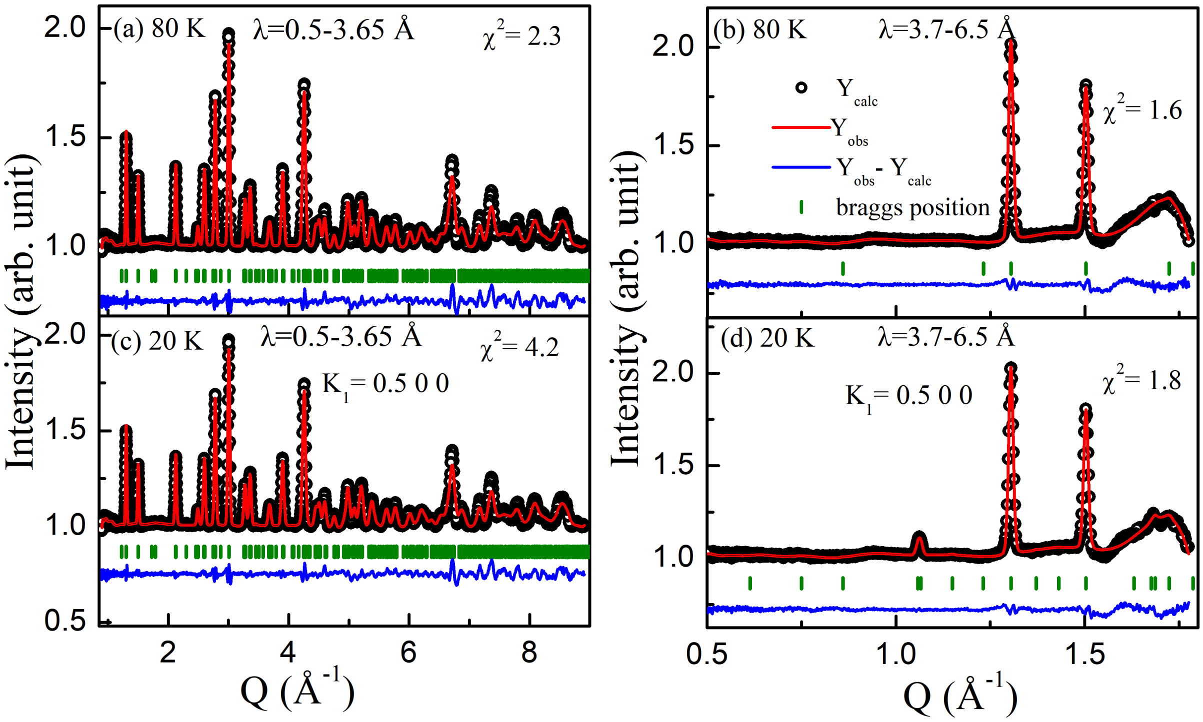

Figure 4.5: Rietveld refinement of TOF data at 80 K for wavelength ranges: (a) 0.5-3.65 Å^{-1} and (b) 3.7-6.5 Å^{-1}. At 20 K, refinement is shown for the $K = (0.5\ 0\ 0)$ propagation vector in wavelength ranges: (c) 0.5-3.65 Å^{-1} and (d) 3.7-6.5 Å^{-1}.

Table 4.4: Basis vectors for the space group $P6_3/mmc$ with propagation vector $\mathbf{K} = (0.25\ 0.25\ 0)$. Irreducible representations for the magnetic Ru site (0.66667 0.33333 0.16250) obtained using the SARAH program.

IR	BV	Atom	BV components					
			$m \parallel a$	$m \parallel b$	$m \parallel c$	$im \parallel a$	$im \parallel b$	$im \parallel c$
Γ_1	ψ_1	1	1	0	0	0	0	0
		2	0	1	0	0	0	0
		3	-1	0	0	0	0	0
		4	0	-1	0	0	0	0
Γ_1	ψ_2	1	0	1	0	0	0	0
		2	1	0	0	0	0	0
		3	0	-1	0	0	0	0
		4	-1	0	0	0	0	0

IR	**BV**	**Atom**	**BV components**					
			$m \parallel a$	$m \parallel b$	$m \parallel c$	$im \parallel a$	$im \parallel b$	$im \parallel c$
Γ_1	ψ_3	1	0	0	1	0	0	0
		2	0	0	-1	0	0	0
		3	0	0	1	0	0	0
		4	0	0	-1	0	0	0
Γ_2	ψ_4	1	1	0	0	0	0	0
		2	0	1	0	0	0	0
		3	1	0	0	0	0	0
		4	0	1	0	0	0	0
Γ_2	ψ_5	1	0	1	0	0	0	0
		2	1	0	0	0	0	0
		3	0	1	0	0	0	0
		4	1	0	0	0	0	0
Γ_2	ψ_6	1	0	0	1	0	0	0
		2	0	0	-1	0	0	0
		3	0	0	-1	0	0	0
		4	0	0	1	0	0	0
Γ_3	ψ_7	1	1	0	0	0	0	0
		2	0	-1	0	0	0	0
		3	-1	0	0	0	0	0
		4	0	1	0	0	0	0
Γ_3	ψ_8	1	0	1	0	0	0	0
		2	-1	0	0	0	0	0
		3	0	-1	0	0	0	0
		4	1	0	0	0	0	0
Γ_3	ψ_9	1	0	0	1	0	0	0
		2	0	0	1	0	0	0
		3	0	0	1	0	0	0
		4	0	0	1	0	0	0

IR	**BV**	**Atom**	**BV components**					
			$m \parallel a$	$m \parallel b$	$m \parallel c$	$im \parallel a$	$im \parallel b$	$im \parallel c$
Γ_4	ψ_{10}	1	1	0	0	0	0	0
		2	0	-1	0	0	0	0
		3	1	0	0	0	0	0
		4	0	-1	0	0	0	0
Γ_4	ψ_{11}	1	0	1	0	0	0	0
		2	-1	0	0	0	0	0
		3	0	1	0	0	0	0
		4	-1	0	0	0	0	0
Γ_4	ψ_{12}	1	0	0	1	0	0	0
		2	0	0	1	0	0	0
		3	0	0	-1	0	0	0
		4	0	0	-1	0	0	0

In this case the Ho and Ru both atoms have four irreducible representations, given by

$$\Gamma_{\text{mag}}(\text{Ho}) = 1\Gamma_1^1 + 1\Gamma_2^1 + 2\Gamma_3^1 + 3\Gamma_4^1$$

$$\Gamma_{\text{mag}}(\text{Ru}) = 3\Gamma_1^1 + \Gamma_2^1 + \Gamma_3^1 + 3\Gamma_4^1$$

We selected the wavelength range of 3.7–6.5 Å to determine the magnetic structure at 4 K because this wavelength range shows large no. of magnetic peaks below T_{N2} and corresponds to low Q region. The Rietveld refinement of 4 K data indicate that a combination of the Γ_1 representation for K_2 along with the Γ_7 representations for K_1 provides the best fit to the experimental data, shown in Fig. 4.6(a). This finding supports the coexistence of two distinct magnetic phases at low temperatures. The corresponding magnetic structures for K_1 (0.5 0 0) and K_2 (0.25 0.25 0) are depicted in Fig. 4.6(c–d). The magnetic structure associated with K_1 wave vector remains nearly unchanged across $T_{N2} < T < T_{N1}$. However, below T_{N2}, the Ho magnetic moment component (m_c) along the c-axis is significantly enhanced compared to the m_a and m_b components along the a- and b-axes. In contrast, the m_c component of the Ru magnetic moment is notably

Table 4.5: Basis vector for the space group $P6_3/mmc$ for $K = (0.25\ 0.25\ 0)$. The irreducible representation for magnetic site Ho (0 0 0), as obtained from SARAh program.

IR	BV	Atom	$m_{\parallel a}$	$m_{\parallel b}$	$m_{\parallel c}$	$im_{\parallel a}$	$im_{\parallel b}$	$im_{\parallel c}$
Γ_1	ψ_1	1	1	1	0	0	0	0
		2	-1	-1	0	0	0	0
Γ_2	ψ_2	1	1	1	0	0	0	0
		2	1	1	0	0	0	0
Γ_3	ψ_3	1	1	-1	0	0	0	0
		2	-1	1	0	0	0	0
	ψ_4	1	0	0	2	0	0	0
		2	0	0	2	0	0	0
Γ_4	ψ_5	1	1	-1	0	0	0	0
		2	1	-1	0	0	0	0
	ψ_6	1	0	0	2	0	0	0
		2	0	0	-2	0	0	0

reduced relative to m_a and m_b, differing from the scenario above T_{N2}. For the K_2 phase, the refined magnetic structure (Figure 4.6(d)) reveals that both Ho and Ru spins are confined to the *ab*-plane, forming an $\uparrow\uparrow\downarrow\downarrow$ antiferromagnetic spin-structure, while along the *c*-axis the spin structure is $\uparrow\downarrow\uparrow$. Notably, at $T = 4$ K, the total magnetic moment of the Ho atom is nearly saturated ($\sim$10.1 μ_B), while the Ru moment is $\sim$1.6 μ_B, consistent with previous reports [62].

4.5.2 Mechanism of Spin-driven ferroelectricity

Here, we will elucidate the mechanism of spin-driven polarization. The electric polarization in this system most likely may arise through inverse D-M interactions from non-collinear magnetic structure (spin-current model) or through exchange-striction from the collinear spin-structure. First, we have calculated inverse D-M interaction $[P_{ij} \propto \mathbf{e}_{ij} \times (\mathbf{S}_i \times \mathbf{S}_j)]$ between nearest Ru and Ho-spins (Ru-O-Ho configurations) of magnetic phase related to K_1-spin structure, shown in Fig. 4.6(c) for T = 4 K. This results in local polarization, however, the direction of the polarization of one Ru-O-Ho configuration is opposite to the neighboring configuration. Hence, the net polarization is canceled out in the whole magnetic unit cell (in macroscopic scale), as shown in Fig. 4.7(a). Therefore, the inverse D-M interaction associated with non-collinear K_1-spin structure cannot produce ferroelectric polarization. The system magnetically orders below 50 K (T_{N1}) associated with K_1-spin structure. The absence of ferroelectricity in $T_{N2} < T < T_{N1}$ agrees with the above conclusion. The clear peak in dielectric constant is observed at T_{N2} and ferroelectricity is observed below T_{N2}, where 2nd magnetic phase related to K_2-spin structure emerges. Initially, it was assumed that the spin-driven ferroelectricity might arise from exchange-striction of $\uparrow\uparrow\downarrow\downarrow$ spin-structure of Ho or Ru from 2nd-magnetic phase, similar to the observed in the Ca_3CoMnO_6 system [32]. In the exchange-striction mechanism, the symmetric exchange interaction between the parallel spins ($\uparrow\uparrow$ or $\downarrow\downarrow$) helps to make a shorter bond which moves the ion closer, subsequently, opposite (antiparallel) spins ($\uparrow\downarrow$) make the bond longer between these two ions, which creates a local polarization. Here, the exchange-interaction is mediated via oxygen ions. For $\uparrow\uparrow\downarrow\downarrow$-spin structure ($K_2$) in *ab*-plane of this compound, the Ho ions are connected to next Ho-ions via Ho-O-Ru-O-Ho exchange-path or via Ho-O-Ba-O-Ho path (see Fig. 4.3), there is no Ho-O-Ho path exists. Thus, the superexchange interaction between two nearest Ho-spins is not possible, the superexchange path should be via Ru. Hence, $\uparrow\uparrow\downarrow\downarrow$ Ho-spins cannot have such exchange-striction effect (negligible displacement) and such a configuration cannot produce any polarization. Similarly Ru-O-Ru super-exchange interaction is restricted in Ru_2O_9-dimers, as they are not directly interconnected (a clear view is shown in Fig. 4.1(a). Therefore the magnetic ordering is obtained via Ru-O-Ho exchange path only. Hence, the Exchange-striction mechanism in $\uparrow\uparrow\downarrow\downarrow$ spin-structure of only Ho or Ru-ions cannot produce dipole moment. In $\uparrow\uparrow\downarrow\downarrow$ (K_2)- spin-structure, the individual Ru-spins moments or individual Ho-spins moments are collinear in the *ab*-plane among themselves, nevertheless, the Ho and Ru spins are non-collinear to each other connected via Ru-O-Ho-O-Ru exchange path in *ab*-plane. The Ru-O-Ho-O-Ru super exchange paths are shown in Fig. 4.3 where Ho and Ru-ions are arranged in a zig-zag pattern. The presence of larger d-orbitals ($4d$) results in strong spin-orbit coupling in this system. Normally, stronger spin-orbit coupling may favor the D-M interaction, which may lead to a preference for non-collinear spin configurations of Ho and Ru via strong d-f coupling. In this study, we observe a low magnetic moment of the Ru atom, which is 1.1 μ_B compared to its average spin-only values in Ru^{4+} (d^4) and Ru^{5+} (d^3) states. This observation further suggests the possibility of electron itineracy with a larger extension of $4d$-orbital, or/and competing effects of crystal field effects and spin-orbit coupling of the Ru atom in this system. We have calculated the inverse D-M interaction between the nearest Ru and Ho (connected

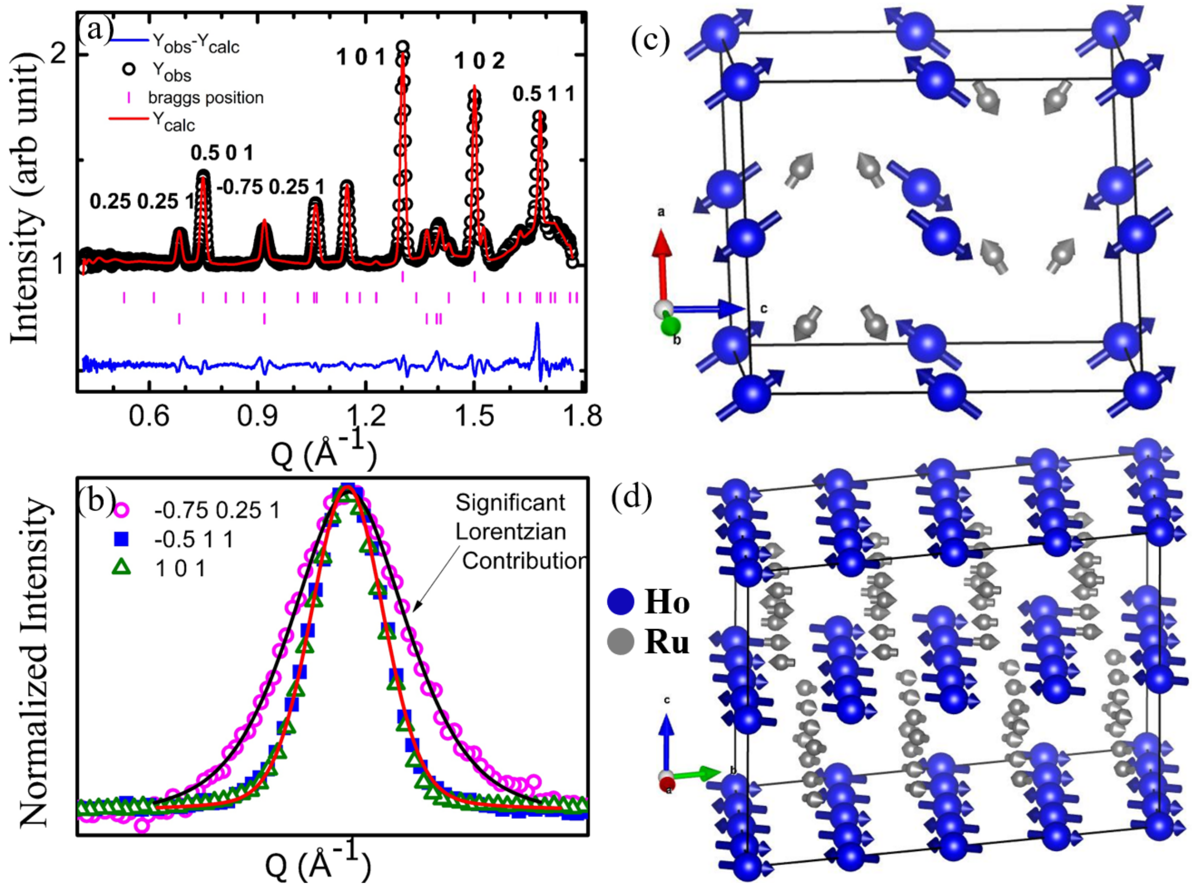

Figure 4.6: (a) Rietveld refinement of time-of-flight neutron diffraction data in the low-$|Q|$ regime at $T = 4$ K of $Ba_3HoRu_2O_9$. The open black circles represent the experimental data, while the red solid line shows the Rietveld fitting. The vertical bars display the Bragg peak positions: the upper vertical lines are Bragg lines for the crystal structure, followed by reflections associated with $K_1 = (0.5\ 0\ 0)$, and $K_2 = (0.25\ 0.25\ 0)$ respectively. The lower blue line is the difference between the experimental and calculated intensity. (b) Normalized peaks for lattice (1 0 1), K_1 (-0.5 1 1) & K_2 (-0.75 0.25 1) magnetic structure as discussed in the text. The value of the x-axis ($|Q|$) is shifted for each plot to place the peak at the same position to compare the peak shape directly. The solid red line is fitted with a Gaussian and the solid black line is fitted with Gaussian and Lorentzian parameters. Magnetic structure of (c) 1st magnetic phase (canted structure) associated with K_1 propagation vector, and (d) 2nd magnetic phase (up-up-down-down structure) associated with K_2 propagation vector at $T = 4$ K for $Ba_3HoRu_2O_9$.

via Ru-O-Ho path) of this (K_2)- spin-structure, which produces a non-zero value which shifts the oxygen atoms and thus, non-zero local polarization (see Fig. 4.7(b)). We have calculated the whole unit cell. We obtained that the local polarization does not cancel out in the whole unit cell and a non-zero resultant polarization is obtained in *ab*-plane (Fig. 4.7(b)). The inverse D-M interaction,

$$P_{ij} \propto \mathbf{e}_{ij} \times (\mathbf{S}_i \times \mathbf{S}_j),$$

is evaluated below for the nearest-neighbor Ho-Ru spin configuration.

We have

$$\vec{P}(\text{Ho1-Ru1}) \propto \vec{e}(\text{Ho1Ru1}) \times (\vec{S}_{\text{Ho1}} \times \vec{S}_{\text{Ru1}}),$$

where $\vec{e}(\text{Ho1Ru1})$ is the unit vector connecting Ho1 and Ru1, and $\vec{S}_{\text{Ho1}}$ and $\vec{S}_{\text{Ru1}}$ are the spin vectors of Ho1 and Ru1, respectively.

The relative position vector between Ho1 and Ru1 is $\vec{R}(\text{Ho1Ru1}) = \vec{R}_{\text{Ru1}} - \vec{R}_{\text{Ho1}}$, which evaluates to

$$\vec{R}(\text{Ho1Ru1}) = 2.9270\,\hat{a} + 1.6898\,\hat{b} - 2.3370\,\hat{c}.$$

The corresponding unit vector is

$$\vec{e}(\text{Ho1Ru1}) = 0.7123\,\hat{a} + 0.4112\,\hat{b} - 0.5687\,\hat{c}.$$

The cross product of the Ho and Ru spin vectors is

$$\begin{aligned}\vec{S}_{\text{Ho1}} \times \vec{S}_{\text{Ru1}} &= (-4.11528\,\hat{a} - 4.11528\,\hat{b} + 0\,\hat{c}) \\ &\quad \times (-1.24506\,\hat{a} - 0.86552\,\hat{b} + 0\,\hat{c}) \\ &= -1.5619133712\,\hat{c}.\end{aligned}$$

Therefore, the resulting local polarization vector is

$$\vec{P}(\text{Ho1-Ru1}) \propto 0.6423\,\hat{a} - 1.1126\,\hat{b} + 0\,\hat{c}.$$

All these values of positions and spins of Ho and Ru ions are taken from the magnetic structure obtained from neutron diffraction. Similarly, we have calculated the polarization for all other configurations in the magnetic cell.

$$\vec{P}(\text{Ru1-Ho2}) \propto (0.6423\,\hat{a} + 1.1126\,\hat{b} + 0\,\hat{c})$$
$$\vec{P}(\text{Ho2-Ru2}) \propto (0.6423\,\hat{a} - 1.1126\,\hat{b} + 0\,\hat{c})$$
$$\vec{P}(\text{Ru2-Ho3}) \propto (-0.6423\,\hat{a} - 1.1126\,\hat{b} + 0\,\hat{c})$$
$$\vec{P}(\text{Ho3-Ru3}) \propto (0.6423\,\hat{a} - 1.1126\,\hat{b} + 0\,\hat{c})$$
$$\vec{P}(\text{Ru3-Ho4}) \propto (0.6423\,\hat{a} + 1.1126\,\hat{b} + 0\,\hat{c})$$
$$\vec{P}(\text{Ho4-Ru4}) \propto (0.6423\,\hat{a} - 1.1126\,\hat{b} + 0\,\hat{c})$$
$$\vec{P}(\text{Ru4-Ho1}) \propto (-0.6423\,\hat{a} - 1.1126\,\hat{b} + 0\,\hat{c})$$

Both the results (peak shift & Inverse DM interaction) support that in this system spin-driven ferroelectric polarization arises from the K_2-spin structure, however, the net polarizations (of a domain) nearly cancel out due to random domain dynamics of ME domains in bulk macroscopic scale yielding very weak experimentally observed polarization. In this structure, the spins are oriented with $\uparrow\uparrow\downarrow\downarrow$-spin structure of Ho and Ru-spins individually and non-collinear between Ho and Ru-spins. A higher magnetic field may destabilize the spin-structure, where spins will try to reorient along the applied H. Eventually, a spin can be flipped ($\uparrow\uparrow\uparrow\downarrow$) by changing the whole spin structure, depending on the strength of the magnetic field. The H-induced magnetic transition $\sim$ 36 kOe and the $M(T)$ feature at a very high field (50 kOe) are consistent with such behavior [92]. If there is a change of spin-pattern, then definitely the canting angle of Ru and Ho spins will be different, therefore, the direction of the vector $[\mathbf{e}_{ij} \times (\mathbf{S}_i \times \mathbf{S}_j)]$ will be different. The relative spin-orientation between S_{Ru} and S_{Ho} under a high magnetic field is such that overall polarization may cancel out on a macroscopic scale. The shifting of the dielectric peak towards lower temperature with increasing magnetic field, and further the suppression (absence) of the dielectric feature under the high-magnetic field of 50 kOe is consistent with this (spin-driven) ferroelectric polarization model [92].

To date, there are mostly experimental reports of those multiferroic compounds where spin-pattern of $3d$-metal ion is responsible for spin-driven ferroelectricity, as discussed in the introduction. However, the experimental evidence of electric polarization as a result of inverse D-M interaction of non-collinear spin-moments occurring between two different atoms does not exist (to the best of our knowledge). The multiferroic $GdMn_2O_5$ compound exhibits the largest polarization among all multiferroic-II compounds (that is, multiferroic ME system where spin-drives the ferroelectricity). It is demonstrated that the exchange-striction mechanism between collinear spins of Gd($4f$) and Mn($3d$) contributed to a larger polarization of $GdMn_2O_5$ compound [29]. Here we observe that the spin-driven

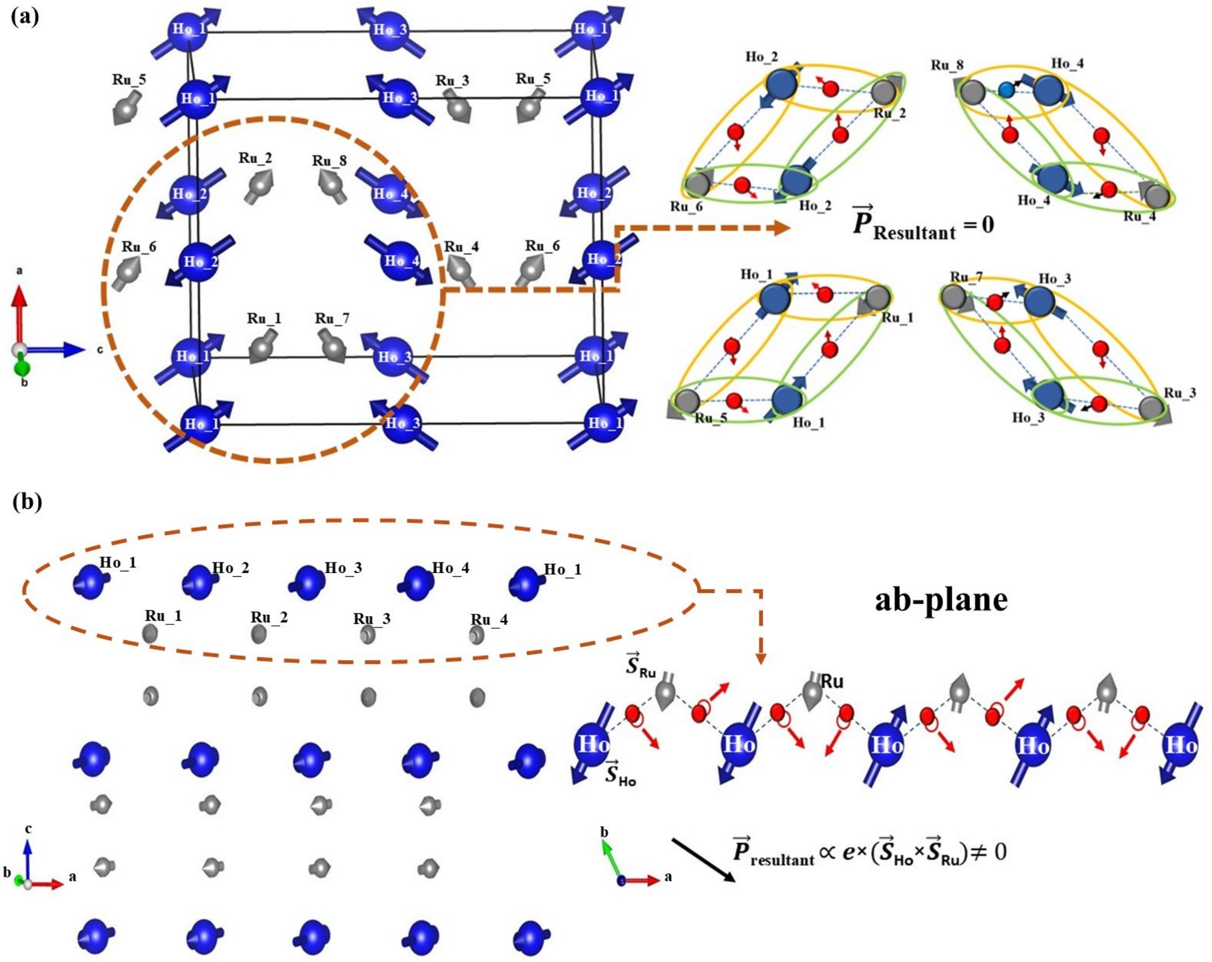

Figure 4.7: (a) and (b) (left) magnetic structure at 4 K for the 1st magnetic phase (canted structure) associated with the k_1 propagation vector and the 2nd magnetic phase (up-up-down-down structure) associated with the k_2 propagation vector, respectively. (Right) calculated inverse D-M interaction considering all neighboring Ru and Ho spins for each structure, respectively, as discussed in the text. The atoms are denoted in different colors as follows: blue (Ho), gray (Ru), and red (oxygen). The blue arrows on Ho and gray arrow on Ru atoms denote the spins of the respective atoms. The arrows on oxygen show the direction of local polarization, that is, the direction of inverse D-M interaction between related Ho and Ru spins of the corresponding Ho-O-Ru configuration. The large black arrow shows the direction of the resultant polarization. The resultant polarization is zero for (a) and non-zero for (b).

polarization is governed from non-collinear spin-structure of two different atoms, that is, Ho($4f$) and Ru($4d$) through inverse D-M interaction. This further supports strong $4d$-$4f$ correlation in this system. The stronger spin-orbit coupling in larger $4d$-orbital compared to that of $3d$-orbital might play a decisive role.

4.5.3 Magnetoelectric domain dynamics

We have measured the dielectric constant as a function of temperature in the absence magnetic field at various frequencies from ν = 1.1-120 kHz, which is shown in Fig. 4.8. The low-frequency data below 1 kHz could not be recorded due to the low signal-to-noise ratio. The real (ε') and imaginary (ε'') parts of the dielectric constant are presented in Fig. 4.8(a-b). The dielectric peak appears at the onset of magnetic ordering T_{N2} as a result of strong MDE coupling, as reported earlier [92]. Interestingly, the peak present in $\varepsilon'(T)$ and $\varepsilon''(T)$ exhibits a frequency-dependent behavior around T_{N2}. The peak temperature (T_P) of $\varepsilon'(T)$ and $\varepsilon''(T)$ shifts to a higher temperature with increasing frequency (ν). Fig. 4.8(c) shows the plot of ln(ν) versus the inverse of T_P (peak temperature extracted from ε''), showing it follows an Arrhenius relation ($\nu = \nu_0 \exp(E_a/k_B T_P)$, ν_0 = pre-exponential factor, E_a = activation energy), exhibits logarithmic relaxation behavior with $E_a \sim 574$ K. The frequency dependence behavior can be observed due to the presence of dipolar glass behavior or ferroelectric domain relaxation/ reorientation. The activation energy is related to the energy barriers associated with the ferroelectric domain reorientation. Very low polarization value in PUND measurement is consistent with the concept of finite-size ferroelectric (ME) domains instead of true long-range ordering. A similar effect was reported in the well-known multiferroic compound Ca_3CoMnO_6 where a low polarization value was experimentally obtained due to the finite-size domains instead of true long-range ordering [32]

The ac magnetization as a function of temperature is shown in Fig. 4.9 for different frequencies (1 Hz-1.3 kHz) which does not yield any frequency dependence behavior, in contrast with the dielectric constant. We propose this could be an artifact arising from a different frequency regime in which the finite-size magnetic domains respond to higher frequencies. Similar behavior is observed in the magnetism-driven ferroelectric system Dy_2BaNiO_5 where the frequency-dependent behavior is observed only in high-frequency regions ($>$ 10 kHz) [95] the response of the finite-size magnetic domains can be very weak for low-frequency regions which is consistent with the concept of ferroelectric (ME) domains instead of true long-range ordering. We have analyzed the peak shape in neutron

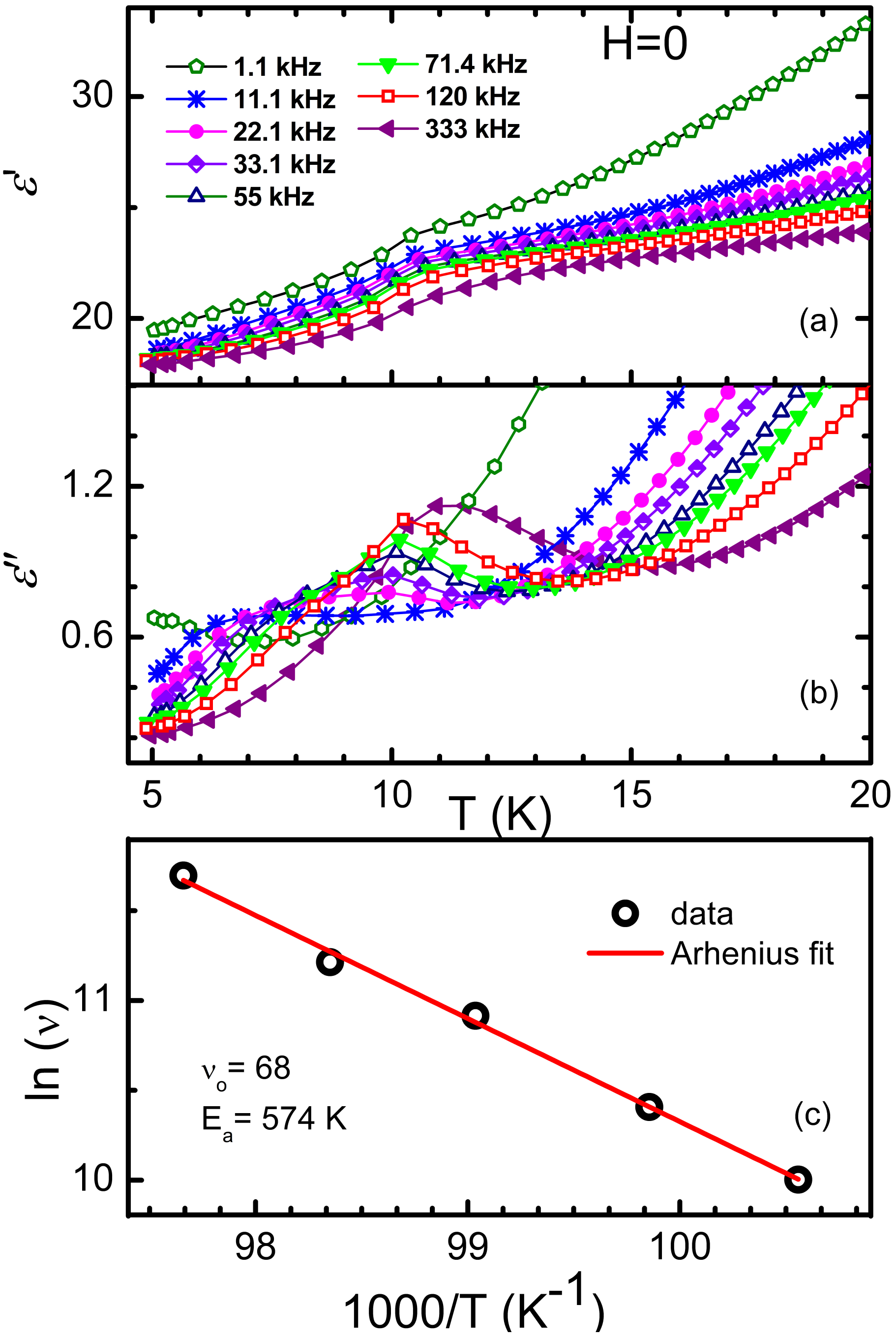

Figure 4.8: (a) The real and (b) imaginary part of dielectric constant as a function of temperature under various frequencies (1.1 -120 kHz). (c) Arrhenius plot ln(ν)versus inverse of T_p. The low frequencies data in (c) is not included either due to absence of the corresponding peak or very broad features.

diffraction to clearly resolve this issue. For this we have superimposed three normalized

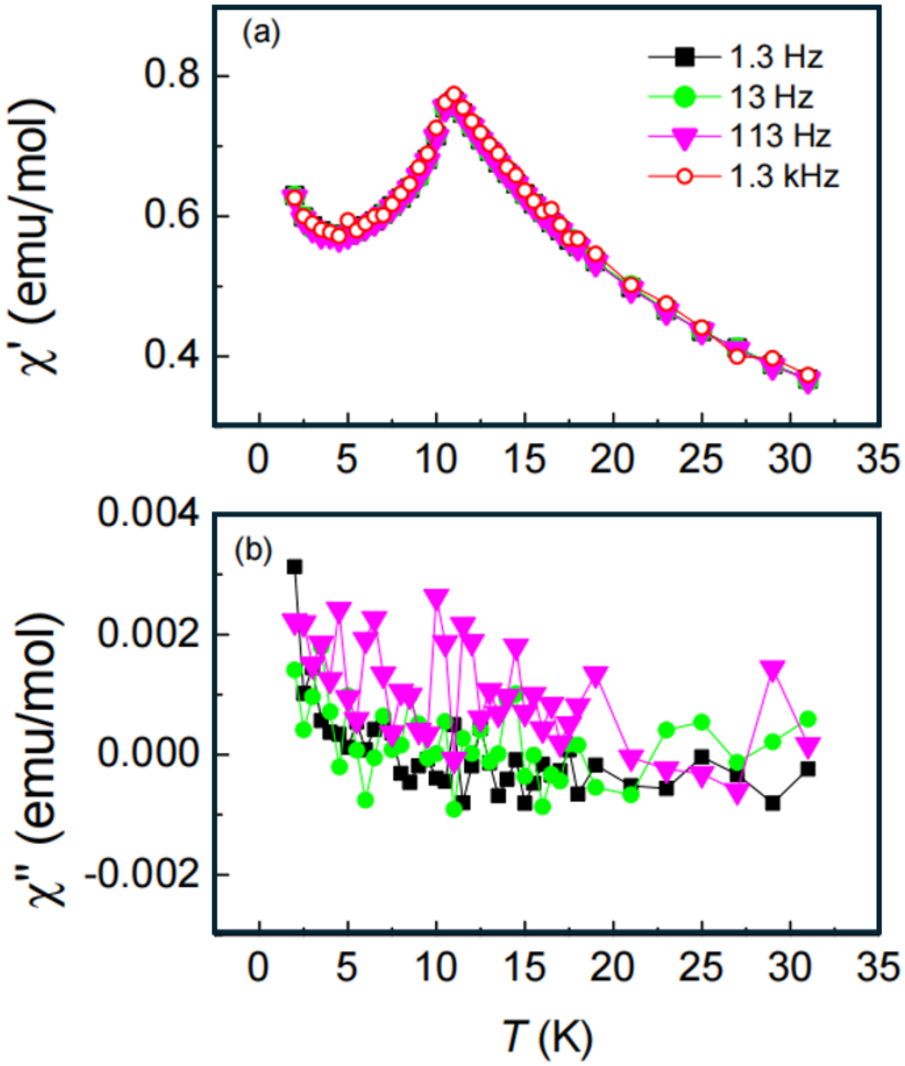

Figure 4.9: (a) The real part (χ') and (b) imaginary part (χ'') of ac magnetic susceptibility as a function of temperature for various frequencies from 1.3 Hz- 1.3 kHz.

representative peaks obtained from neutron diffraction in Fig. 4.6(b). We have considered the different peaks at T= 4 K; one is (1 0 1)-peak for the nuclear structure (only lattice Bragg peak), the other one is (-0.5 1 1) peak which is a magnetic peak related to K_1-spin structure (K_1= 0.5 0 0), and the third one is (-0.75 0.25 1) magnetic peak for K_2-spin structure (magnetic Bragg peak related to K_2= 0.25 0.25 0). The (0.5 1 1) magnetic peak related to the K_1-spin structure is well fitted with the (gaussian) peak shape parameters same as the (1 0 1) lattice peak used in the refinement (Fig. 4.6(b)). The (-0.75 0.25 1)-peak shape associated with the K_2-spin structure shows significant broadening when compared to that of the K_1-spin structure (Fig. 4.6(b)). One needs to introduce significant Lorentzian parameters to fit the peaks associated with K_2-spin structure. Therefore, we only observe the broadening of the magnetic peak related to K_2- spin structure, no broadening is observed for the magnetic peak associated to K_1-spin structure even at low temperature below T_{N2}. This shows that the K_2- spin structure has a shorter coherence length compared to that of K_1-spin structure and it arises through the development of smaller magnetic domains. This results together with our frequency dependence magnetic and dielectric results predict the ME domain dynamics.

4.5.4 Influence of External Pressure

The external parameters (e.g. field, pressure, etc.) have a strong effect on the magnetic (multiferroic) ordering of material. Earlier, we observed that the application of a magnetic field decreases the ordering temperature as observed from the shifting of T-dependence magnetic and dielectric peak towards low temperature with increasing magnetic field and a very high magnetic field (say, H=50 kOe) destroys the multiferroicity, consistent with our spin-driven ferroelectric model [92]. Here we investigate the effect of another parameter, that is, external pressure on the magnetic (multiferroic) ordering of this system. The dc magnetic susceptibility (M/H) under different magnetic fields is shown in Fig. 4.10(a). Temperature-dependent magnetization shows a peak at 10.2 K as reported in the literature [56, 92]. This peak shifts to a lower temperature and broadens with an increasing magnetic field, eventually being suppressed at 50 kOe, agreeing with the previous report [92] This result confirms the reproducibility of the magnetic feature where the pressure cell does not have any extrinsic effect on the measurements. We have plotted the dc magnetization under external pressure at a fixed magnetic field of 10 kOe in Fig. 4.10(b). Interestingly, the temperature of the magnetic peak increases with increasing external pressure. The magnetic peak at 10.2 K in the absence of external pressure shifts to 11, 11.5 and 12.2 K under the application of small pressure of 0.5, 0.8 and 1.2 GPa, respectively, corresponding to an enhancement of 1.6 K/GPa. These results suggest that external pressure and magnetic fields have opposing effects on the magnetic ordering temperature. The inset of Fig. 4.10(b) shows the isothermal magnetization plot as a function of the magnetic field for the absence and presence of external pressure of 1.2 GPa at T=2 K. We observe a small decrease in the magnetization value at 2 K in M(H) under external pressure which is consistent with M(T) behavior. In the well-known spin-driven ferroelectric system, $DyMn_2O_5$, the application of pressure enhances the ferroelectric polarization

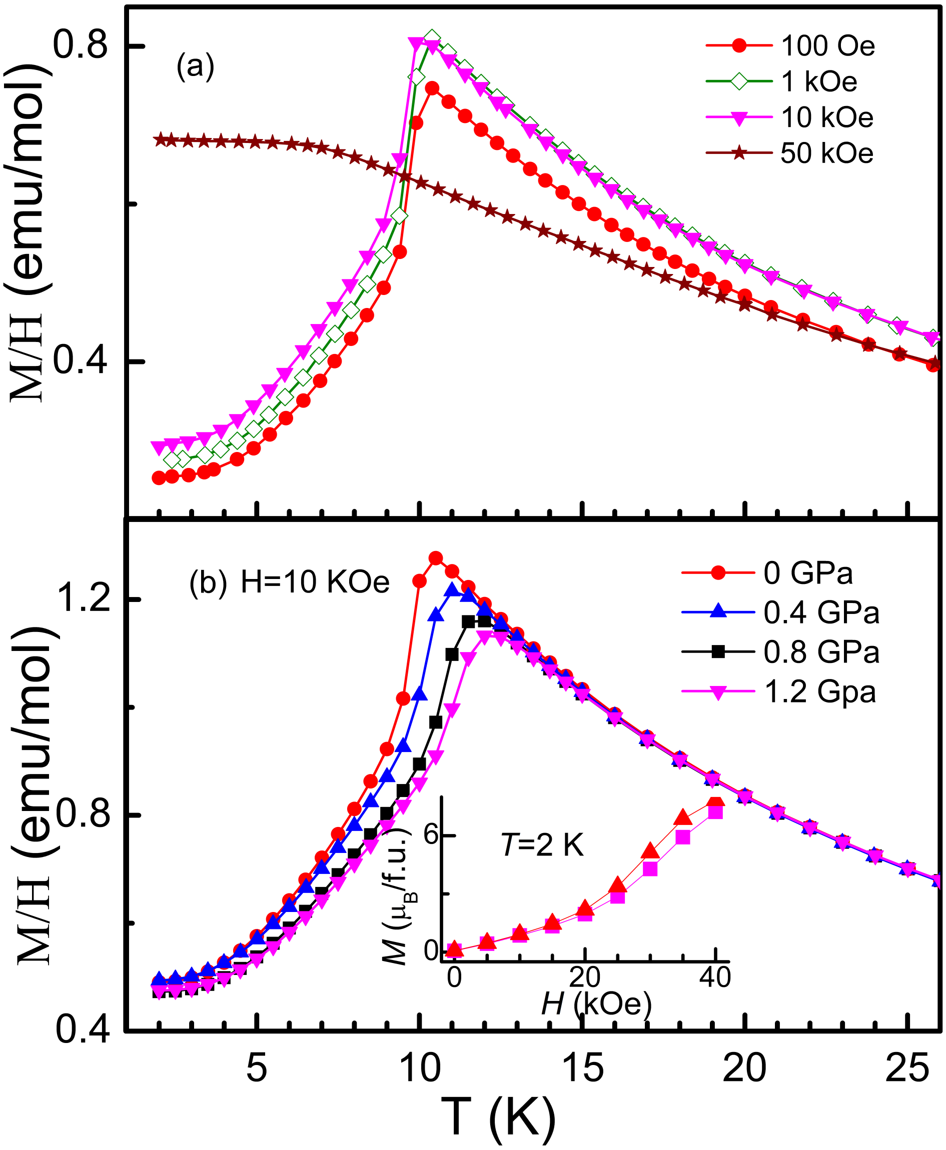

Figure 4.10: DC magnetic susceptibility as a function of temperature, (a) in different applied field for zero applied pressure, and (b) under different applied pressures (0,0.4, 0.8 and 1.2 GPa) in the presence of 10 kOe magnetic field. The inset of (b) shows the isothermal magnetization M(H) in the absence of pressure and the presence of 1.2 GPa pressure.

at low temperatures by stabilizing the commensurate Mn-spin order [96]. In $RMnO_3$ (R = Dy, Tb, and Gd), the system was found to show a pressure-induced phase transition into the phase with large spin-driven ferroelectric polarization along 'a'- axis [97]. Density functional simulations suggest that the enhancement of polarization by applying pressure in $TbMnO_3$ is due to the stabilization of a collinear up-up-down-down spin-ordered state [98]. Here we speculate that similarly to previous reports on other systems, pressure (mildly) stabilizes the up-up-down-down structure resulting in an enhancement of magnetic ordering competing with temperature fluctuations.

4.5.5 In-depth Structural study through Temperature dependence synchrotron XRD

We have analyzed the synchrotron high-resolution powder XRD data using Rietveld refinement in the temperature range of 4-300 K [63]. The Rietveld refinement fitting of HRXRD data at 8 K and 80 K are shown in Fig. 4.11. We observed that the crystal symmetry remains consistent in temperature fitting with $P6_3/mmc$ (194) space group. The T-dependence plot of lattice parameters (a, c) is represented in Fig. 4.12(a-b) from 4-40 K [99, 100]. A clear anomaly in the lattice parameters (a, c) around the transition temperature T_{N2} is observed. Cooling from the high temperature, the lattice constants (a, c) reduce with decreasing temperature due to thermal contraction. However, at the onset of the T_{N2}, the curve goes upward for lattice constant 'c' with the decreasing temperature, which is not usual. The lattice constant 'a' also shows a peak at T_{N2}. The change in the lattice volume (V) with temperature is shown in Fig. 4.12(c) which displays a clear anomaly around T_{N2} in the form of a peak. Considering that lattice volume is directly linked to the Gibbs free energy (G),

$$V = \left(\frac{\partial G}{\partial P}\right)_T ,$$

any discontinuity in volume implies a discontinuity in Gibbs free energy. This observation indicates a possible first-order type phase transition [101] A sharp change in T-dependence heat capacity is observed at T_{N2} predicting the first-order nature of the phase transition [62], consistent with this result. We have also checked some other non-centrosymmetric space groups related to this structure (where spatial inversion symmetry is broken), though, we do not find any further improvement in the goodness of fit with these related space groups. We have analyzed the XRD data with a non-centrosymmetric space group with a similar structure. The Rietveld refinement fitting at $T = 8$ K for the

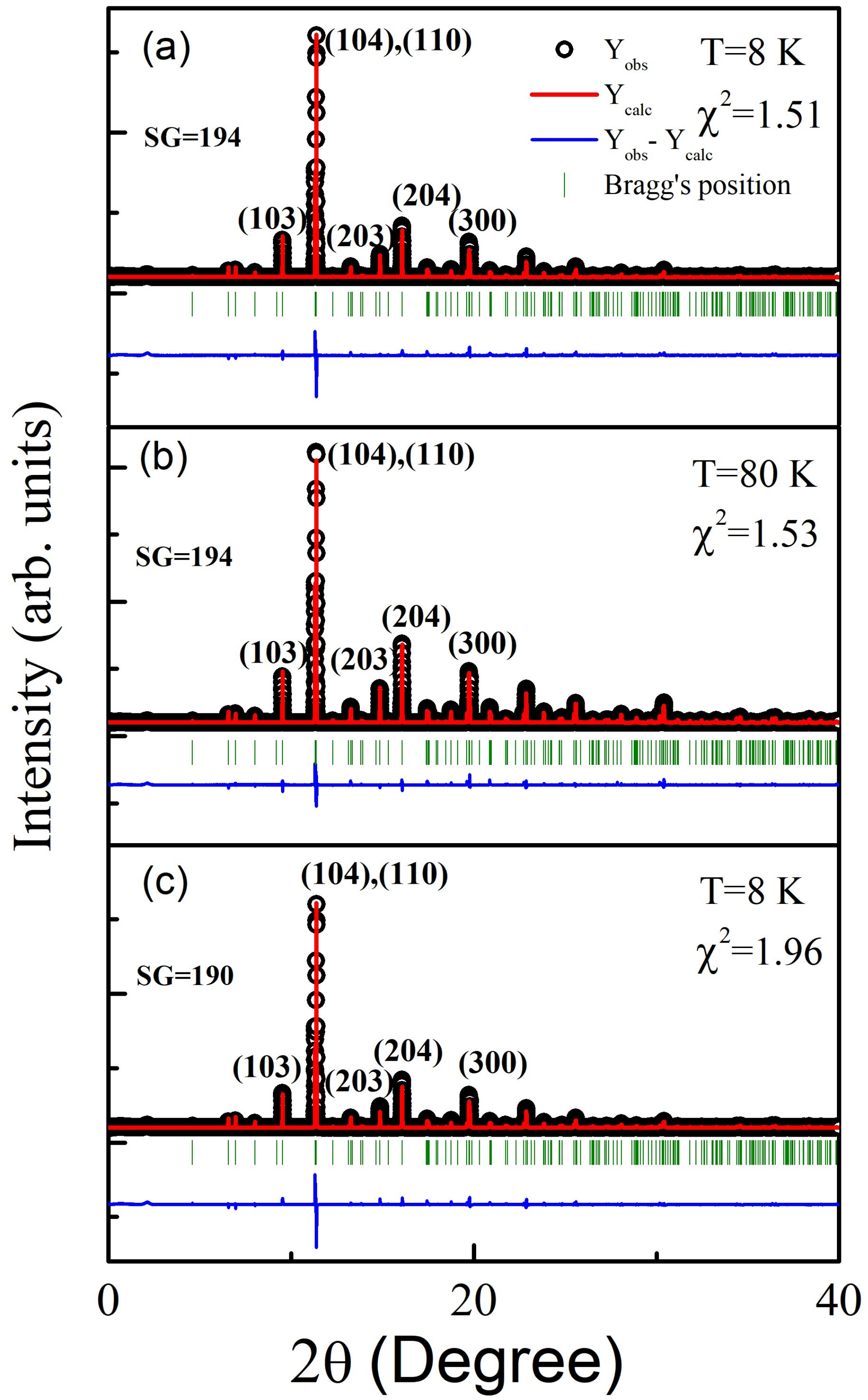

Figure 4.11: Synchrotron powder X-ray diffraction pattern of $Ba_3HoRu_2O_9$ (a) at 8 K and (b) 80 K for space group (SG) 194, and (c) Synchrotron powder X-ray diffraction pattern of $Ba_3HoRu_2O_9$ at 8 K for space group 190 in Rietveld refinement.

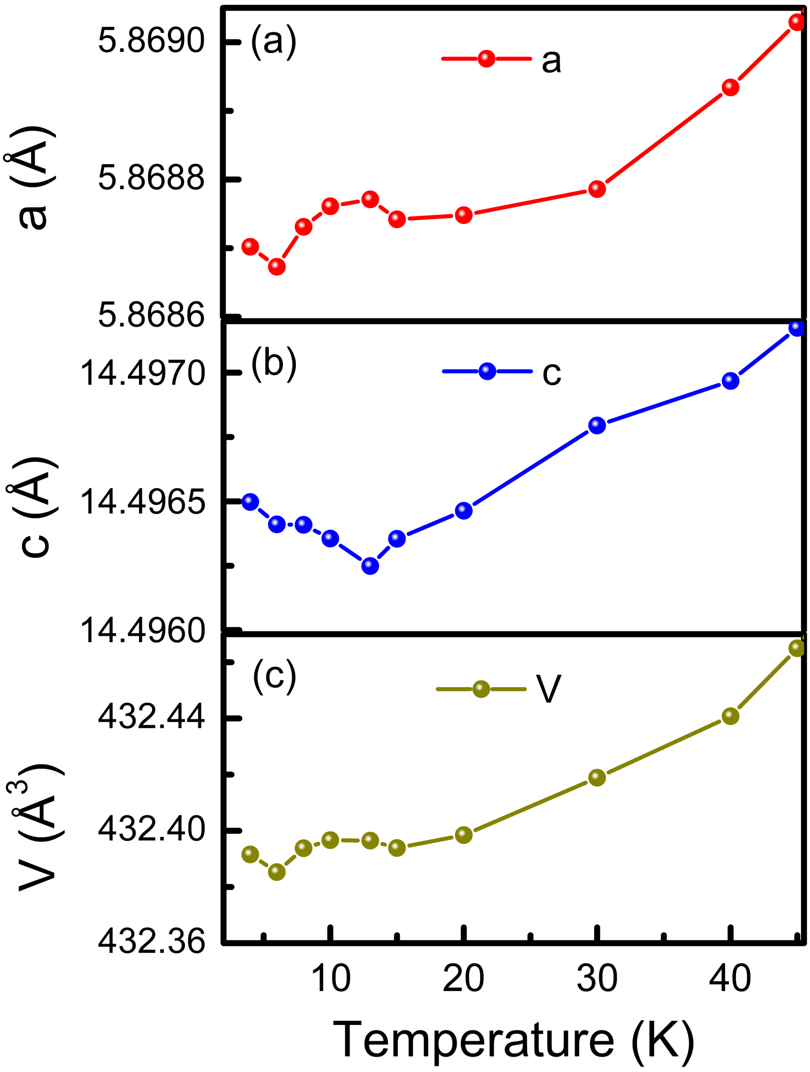

Figure 4.12: (a) and (b) Thermal variation of lattice parameters (a- and *c*-axis) respectively. (c) thermal variation of lattice volume. The symbol size represents the error of the data.

non-centrosymmetric space group, $P\overline{6}2c$, is shown in Fig. 4.11(c). We found equally good fitting for both the space groups at 8 K. It is to be noted that the displacement of atoms in multiferroic-II (spin-driven ferroelectric) is generally very small to be traced in the X-ray/neutron diffraction. Till now, for all the reported spin-driven ferroelectric systems, the breaking of spatial inversion symmetry is not traceable directly from the XRD analysis, rather an anomaly in the lattice parameters around multiferroic ordering is reported in the literature [62, 101, 102]. Friedel's law states that the intensities of the h, k, l and $-h, -k, -l$ reflections are equal. This is true if the crystal is centrosymmetric or if no resonant scattering is present. It is impossible to conclude by X-ray powder diffraction whether an inversion center is present unless significant structural change is there in general. Combining the results of synchrotron X-ray and bulk ferroelectric measurements, we propose the non-centrosymmetric space group $P\overline{6}2c$ for this title compound.

4.5.6 Inelastic Neutron Scattering as a Probe of Magnetic and Crystal Electric Field Excitations

To cover all the low and high energy excitations we have performed the INS on this system considering two incident energy 30 meV and 160 meV for temperatures 1.8 K, 30 K, 100 K, and 300 K.

Low-energy collective magnetic excitation

Fig. 4.13(a) Color-coded contour maps of the measured scattering intensity as a function of energy and momentum transfer ($|Q|$) of $Ba_3HoRu_2O_9$ using 30 meV incident energy neutrons at 1.8 K in which below 6.2 meV broad excitations is observed. This excitation is more clear in momentum-integrated INS intensity as a function of energy transfer for temperatures between 1.8 K and 300 K in the low-Q range (0.5-3.5 Å^{-1}) (see Fig. 4.13(b)). As temperature increase above T_{N2}, this excitation vanishes, and no comparable low-energy magnetic excitation is observed in the intermediate temperature range $T_{\mathrm{N2}} < T < T_{\mathrm{N1}}$ which suggest that the low-energy spin dynamics are qualitatively different in the two ordered phases. Although the higher-temperature K_1 phase exhibits static long-range magnetic order, no well-defined low-energy collective excitation is observed within the experimental resolution, indicating strongly damped spin dynamics in this regime. This suggests that the excitation below 6.2 meV is closely linked to the spin reorientation below T_{N2} and the simultaneous enhancement of short-range magnetic correlations. The observed excitation is therefore not a localized Ru_2O_9 dimer excitation,

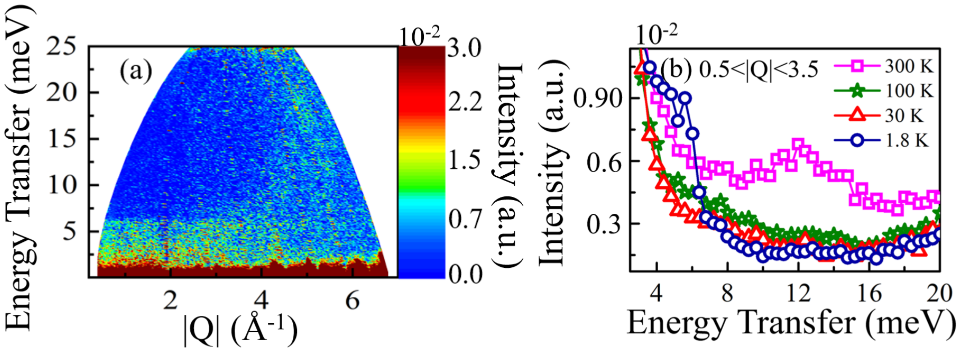

Figure 4.13: (a) Color-coded contour maps of the measured scattering intensity as a function of energy and momentum transfer ($|Q|$) of $Ba_3HoRu_2O_9$ using 30 meV incident energy neutrons at 1.8 K, (b) $|Q|$-integrated intensity versus energy transfer for temperatures between 1.8 and 300 K for the $|Q|$ range $0.5 < |Q|$ (Å^{-1}) < 3.5.

but a collective spin-wave excitation. This behaviour is completely different from other 6H perovskite where R is nonmagnetic such as $Ba_3RRu_2O_9$ ($R =$ Y, La, Ce) [59, 60]. In these systems INS reveals only localized Ru-dimer excitations or strongly suppressed collective excitation. At 300 K a new broad, non-dispersive excitation emerges near 12 meV at low momentum transfer, which is absent at lower temperatures. The appearance of this excitation in the paramagnetic regime together with the absence of the excitation present below 6.2 meV, indicates a non-magnetic origin. Its disappearance at low temperature suggests that static internal exchange fields suppress the mechanism responsible for its neutron-scattering intensity, while thermal fluctuations in the paramagnetic state activate it. The microscopic origin of this excitation is discussed further in Sec. 4.5.8 with Raman spectroscopy and lattice-dynamics calculations.

High-energy localized excitations

Fig. 4.14(a-d) shows the 2D color contour plots of the INS spectra collected with an incident energy of 160 meV. A clear excitation is observed near 40 meV at low momentum transfer ($1 < |Q| < 8$ Å^{-1}). The corresponding Q-integrated 1D cut shown in Fig. 4.14(e) reveal an additional excitation near 20 meV. The intensity of both the excitations remains nearly constant up to 100 K while at 300 K the intensity of 20 meV excitation increases and the 40 meV excitation moderately suppressed. The weak temperature dependence and the absence of noticeable dispersion suggest that these excitations do not arise from long-range magnons. Instead, it likely originates from local excitations associated with the correlated $4d$-$4f$ electronic states. In the high-Q region a broad intensity is observed

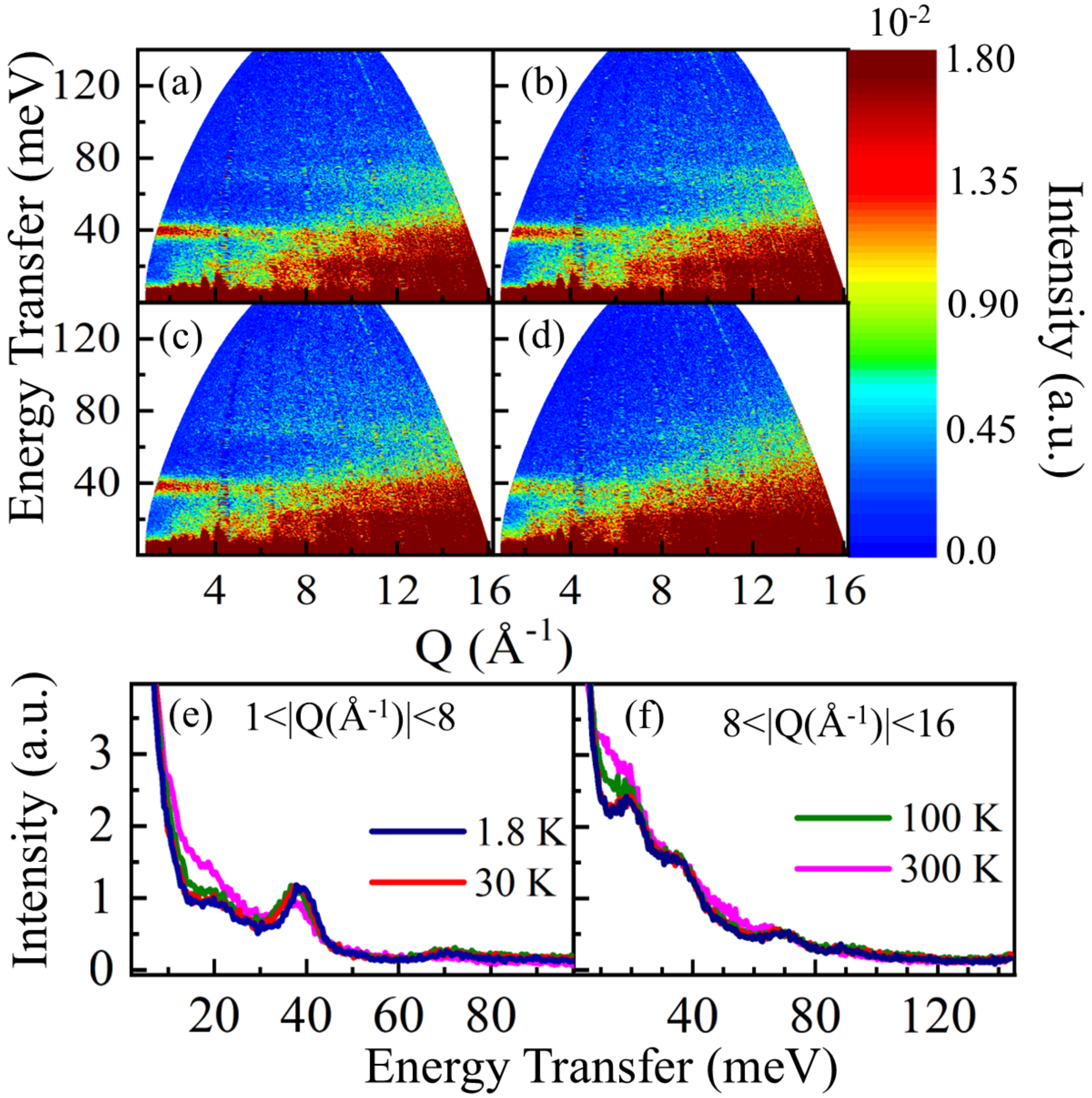

Figure 4.14: Color-coded contour maps of the measured scattering intensity as a function of energy and momentum transfer ($|Q|$) of $Ba_3HoRu_2O_9$ using 160 meV incident energy neutrons at (a) 1.8 K, (b) 30 K, (c) 100 K, and (d) 300 K. $|Q|$-integrated intensity versus energy transfer for temperatures between 1.8 K and 300 K (e) for $1 < |Q|$ (Å^{-1}) < 8 and (f) for $8 < |Q|$ (Å^{-1}) < 16.

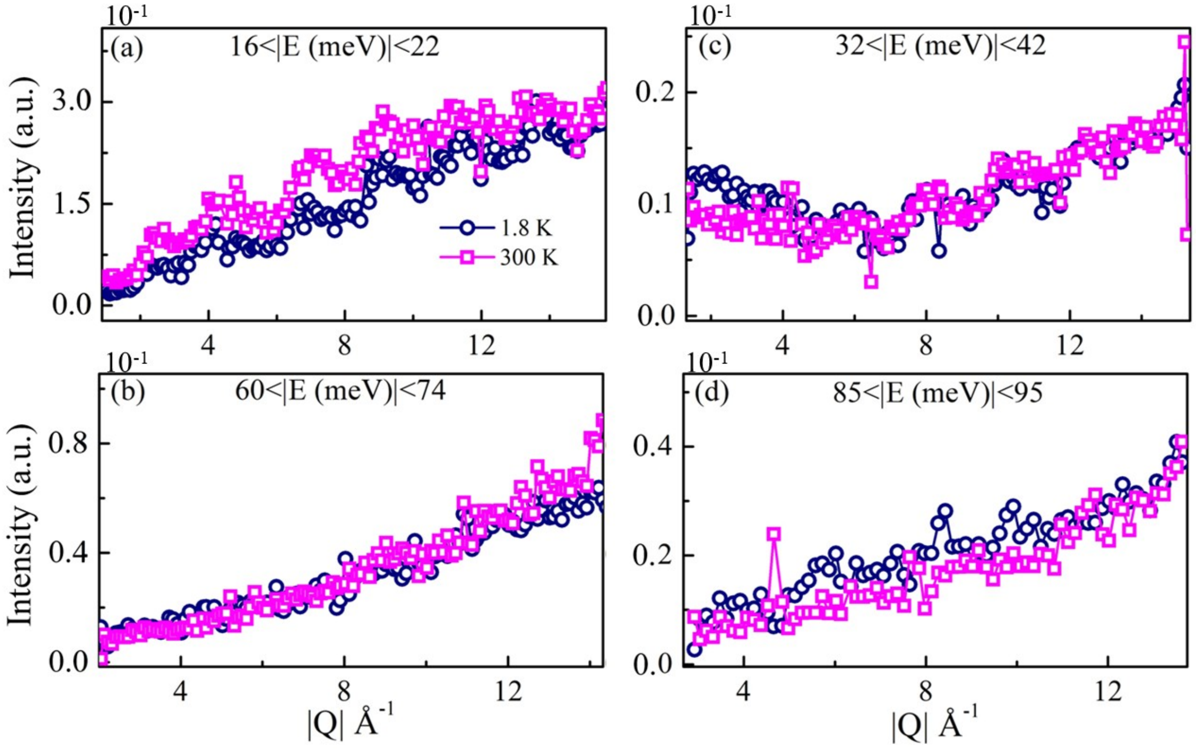

Figure 4.15: Intensity vs momentum transfer at fixed Energy (a) E= 16-22 meV, (b) E= 32-42 meV, (c) E= 60-74 meV and (d) E= 85-95 meV.

below 60 meV along with weak excitations near 70 and 90 meV. These excitations become clearer in the Q-integrated 1D cuts shown in Fig. 4.14(f), where four peaks are resolved between 18-20 meV, 36-40 meV, 70-72 meV, and 85-95 meV. These excitations are present predominantly in the high-|Q| cuts, indicating a lattice-dynamical origin. As temperature increases some of these peaks shift slightly to lower energies (16.4, 63.62 meV at 300 K), consistent with enharmonic phonon behaviour. Further the intensity of the excitation near 89.5 meV gradually decrease and vanish at 300 K, this behaviour is the characteristic of high-energy optical phonon which typically persist at higher temperatures. The absence of sharp, temperature-independent excitations at these energies suggest that these are the optical phonon which involve vibrations of the Ru-O network and the heavier atoms. We have plotted the intensity vs momentum transfer to understand the nature of these excitations for all the peak observed. Fig. 4.15(a), 4.15(b), and 4.15(d) show the momentum dependence of the INS intensity for the peaks around 18-20 meV, 65-70 meV, and 85-95 meV, respectively. In all three cases, the intensity increases gradually with increasing momentum transfer |Q|. Such behaviour is characteristic of phonon. The monotonic increase of intensity with |Q|, together with the dominance of these features at large momentum transfer also indicates that these excitations are phononic in nature. In contrast, Fig. 4.15(c), corresponding to the excitation in the 32-42 meV energy range that exhibits a different momentum dependence. In this case, the intensity initially decreases at low-|Q| and then increase again at high-|Q|. This behaviour cannot be explained by a simple phonon excitation alone or from purely magnetic or crystal-field excitation. Instead, it reflects the coexistence of magnetic and lattice contributions to the neutron cross section.

The decrease in intensity at low|Q| may arises from the magnetic form factor associated with Ho^{3+} crystal-electric-field (CEF) excitations, while the increase at high-|Q| suggest the contribution from lattice vibrations. Such a crossover in the momentum dependence is generally observed in case of CEF-phonon coupling, where localized $4f$ crystal-field states hybridize with phonon modes through spin-orbit-entangled spin-lattice interactions which is also observed in Sr_2DyRuO_6 [48].

4.5.7 SpinW Modeling of Exchange Interactions and Ground State

To interpret the magnetic excitation spectra of $Ba_3HoRu_2O_9$ and to determine the relevant exchange interactions, we have modelled the spin dynamics using linear spin-wave theory within SpinW package. For this initially we have provided the lattice constants, Wyckoff positions of Ho and Ru and then we have assigned the magnetic bonds through exchange interactions between magnetic ions. The spin-Hamiltonian for this system, considering all these factors, is expressed as:

$$\mathcal{H} = \sum_{ij} J_{ij}\, \vec{S}_i \cdot \vec{S}_j + \sum_i D_i\, (S_i^z)^2 \,, \tag{4.5.1}$$

where J_{ij} denotes the exchange interaction between the ith and jth magnetic ions, and $\vec{S}_i$ and $\vec{S}_j$ represent their corresponding spin moments. The second term accounts for the anisotropic contribution, with D_i describing the anisotropy parameter at site i. The model that best reproduces the low-temperature magnetic excitation spectrum requires four dominant exchange interactions, as summarized in Table 4.6.

In $Ba_3HoRu_2O_9$, the Ru-Ru bond is approximately 2.55 Å and the Ru-O-Ru bond angle is significantly smaller than 90°. Although such bond angles are often associated with ferromagnetic superexchange, the very short Ru-Ru distance and the spatially extended nature of the Ru $4d$ orbitals lead to substantial direct t_{2g}-t_{2g} overlap. In face-sharing oc-

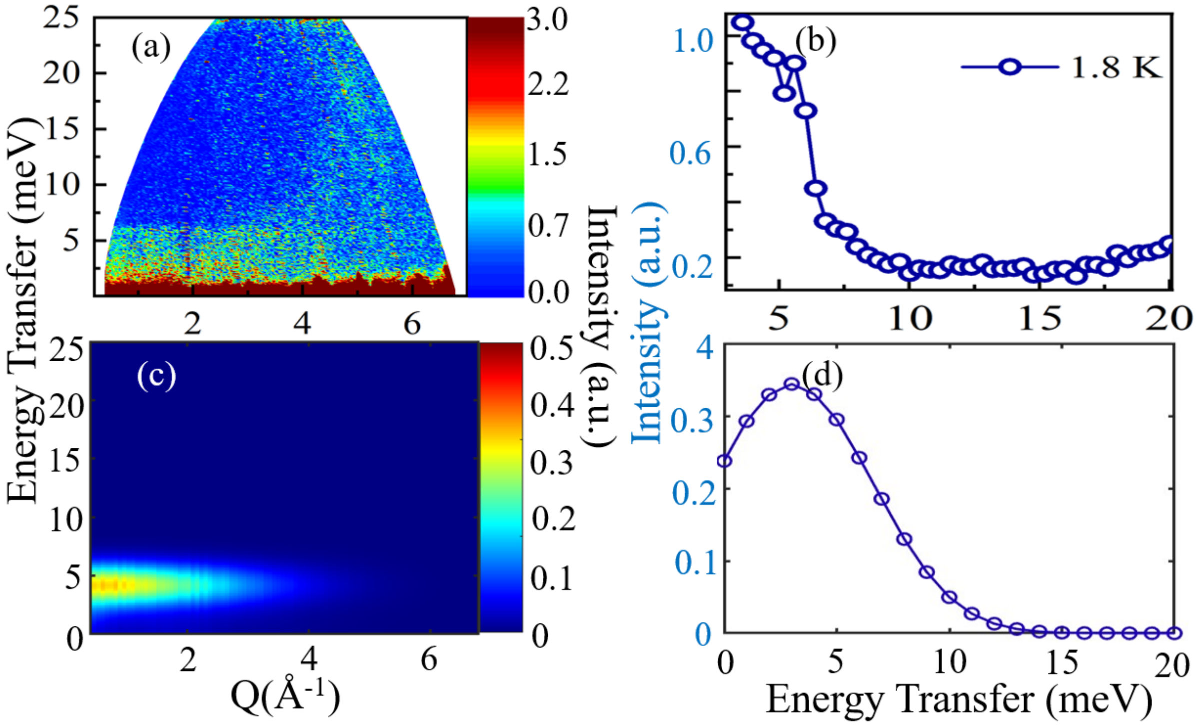

Figure 4.16: Color-coded contour maps of the measured scattering intensity as a function of energy and momentum transfer ($|Q|$) of $Ba_3HoRu_2O_9$ using 30 meV incident energy neutrons at (a) 1.8 K. (b) $|Q|$-integrated intensity versus energy transfer for temperature at 1.8 K. (c) Simulated color-coded contour map of the calculated spin-wave excitation spectrum as described in the text as a function of momentum transfer $|Q|$ and energy transfer, and (d) intensity versus energy transfer for the simulated data obtained from SpinW for $|Q| = 0.5$ to 3.5 Å^{-1}.

tahedra, the resulting direct exchange, particularly involving a_{1g} orbitals oriented along the Ru-Ru axis. This direct *d*-*d* hopping favors a strong antiferromagnetic exchange that dominates over the competing ferromagnetic contributions arising from the distorted Ru-O-Ru superexchange pathway. The net result of this competition stabilizes a strong AFM intradimer interaction (J_1) as commonly observed in 4*d* and 5*d* transition-metal compounds with face-sharing octahedra [19, 103].

This interaction locks the two Ru spins in an antiparallel state and forms the primary magnetic unit for low-energy excitation. Long-range ordering in $Ba_3HoRu_2O_9$ is instead stabilized through a strong Ru-Ho exchange interaction (J_2), which couples the Ru dimers to the localized Ho^{3+} moments via Ru-O-Ho superexchange pathways. The corresponding bond angles are close to 180°, that strongly favors antiferromagnetic coupling. The magnitude of J_2 is comparable to that of J_1 suggest the strong $4d$-$4f$ magnetic coupling in this system. While J_1 determines the internal antiferromagnetic configuration of the Ru dimers, J_2 plays the decisive role in propagating magnetic correlations through the lattice and stabilizing the simultaneous long-range ordering of Ru and Ho moments, consistent with neutron diffraction results [40].

In this system long-range magnetic order is further controlled by weaker interdimer Ru-Ru and exchange interactions J_3 that connect neighbouring Ru_2O_9 dimers through extended Ru-O-Ho-O-Ru exchange paths and Ho-Ho exchange interaction J_4. Due to the long exchange path, orthogonal bonding geometry, and multiple intermediate ions, these interactions are significantly weaker and frustrated in nature which also favors weak ferromagnetic coupling that competes with the dominant antiferromagnetic interactions and plays a crucial role in stabilizing the low-temperature magnetic structure without generating independent magnon excitation. Spin-wave results suggest that when these weak interdimer interactions are removed, the calculated broad excitation below approximately 6.2 meV becomes unstable.

To accurately model the magnetic ground state, we incorporated a 3×3 single-ion anisotropy tensor at the Ho^{3+} sites. Including easy axis term $D_{zz} = -0.25$, is important for stabilizing the magnetic structure and helps to reproduce the exact spin excitation as suggested by the experimental INS data. This behaviour confirms that the 6.2 meV excitation is not a localized oscillation of an isolated Ru dimer, but rather a collective spin-wave excitation that exists only when the full exchange-connected Ru-Ho-Ru lattice is magnetically ordered.Fig. 4.16(b-d) show the comparison between the powder-averaged spin-wave intensity calculated using SpinW with the experimental inelastic neutron scattering data collected at 1.8 K shown in Fig. 4.16(a-b). The close agreement between experiment and simulation confirms that the observed magnetic excitation spectrum arises from exchange-stabilized long-range magnetic order dominated by the strong Ru-Ru intradimer interaction (J_1) and the nearly comparable Ru-Ho antiferromagnetic exchange (J_2), with additional stabilization and frustration effects provided by the weaker interdimer Ru-Ru interactions (J_3 and J_4).

4.5.8 Raman Spectroscopy study to explore phonon modes

Room-temperature Raman spectroscopy was performed to probe the zone-center (Γ-point) optical phonons in $Ba_3HoRu_2O_9$. The Raman data shown in Fig. 4.17 exhibits several well-defined phonon modes at approximately 101, 164, 231, 325, 370, 574, and 774 cm^{-1}.

These observed modes correspond to (Γ-point)-point vibrational excitations, consistent with the symmetry-allowed Raman-active modes of the $P6_3/mmc$ (D_6h) space group, namely A_1g, E_1g, and E_2g representations. We have changed this Raman shift to energy using the formula:

$$E\ (\text{meV}) = 0.12398 \times \omega\ (\text{cm}^{-1}), \tag{4.5.2}$$

where ω is the Raman shift. These phonon modes correspond to energies around 12, 20, 29, 40, 46, 72, and 95 meV, respectively. The low-energy Raman-active modes around 20 meV and 29 meV fall within the optical phonon regime and are assigned primarily to E_2g-type vibrations associated with collective motions of Ba and Ho ions coupled to distortions of the surrounding RuO_6 octahedra. Similar low-energy Raman modes have been reported in ruthenates and rare-earth oxides and are generally attributed to relatively soft lattice vibrations rather than rigid Ru-O bond stretching. The 231 cm^{-1} Raman shift

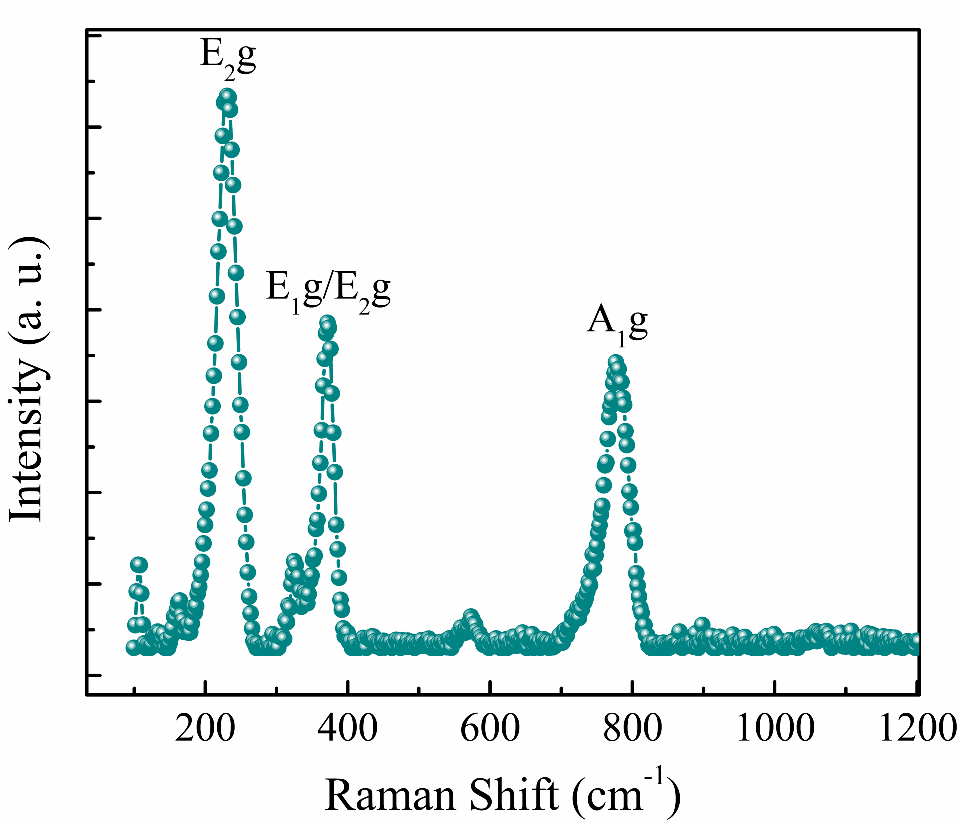

Figure 4.17: Raman Spectroscopy data at room temperature.

that corresponds to a 25 meV excitation is clearly observed in Raman spectroscopy but is absent in the INS spectra. This behavior is consistent with a Γ-point optical phonon whose neutron scattering intensity is suppressed due to a small neutron-weighted structure factor, arising from symmetry-restricted atomic displacement patterns and a dominant oxygen character, rather than from the absence of the vibrational mode itself. Such Raman-visible but INS-weak phonons are well documented in perovskite oxides.

The intermediate-energy modes at 325 cm^{-1} and 370 cm^{-1} (40-46 meV) can be attributed to E_1g/E_2g symmetry modes can be assigned distortions of the Ru-O network, involving RuO_6 octahedral bending vibrations and mixed bending-stretching motions, as established for structurally related ruthenates and orthorhombically distorted perovskites. These modes are known to be sensitive to Ru-O bond lengths and Ru-O-Ru bond angles, which play a crucial role in determining superexchange interactions within the Ru sublattice. As discussed in earlier Raman studies of transition-metal oxides, such phonons can indirectly reflect changes in magnetic exchange pathways without directly probing the magnetic interaction itself [104]. An excitation at a similar energy (40 meV) is also observed in the INS spectra over a broad range of momentum transfer, consistent with a lattice excitation. In contrast, the 46.2 meV excitation is observed only in Raman spectroscopy and is not detected in INS, indicating a strongly reduced neutron scattering cross-section for this particular mode rather than its absence. The coexistence of phonon excitations near 20 meV and 40 meV with Ho^{3+} crystal electric field (CEF) excitations at comparable energies suggests the possibility of phonon-CEF coupling, as reported previously in rare-earth oxides where lattice and $4f$ electronic excitations occur on similar energy scales [105]. A low-energy excitation observed around 12 meV at low $|Q|$ in the INS data is also weakly detected in Raman spectroscopy, indicating a lattice origin of this excitation. The appearance of this excitation only at high temperature suggests that it is associated with a thermally activated phonon mode, whose INS intensity is enhanced by the increased Bose population factor at high temperatures. At low temperatures, the intensity of this mode is strongly suppressed due to reduced phonon occupation and a small neutron scattering structure factor. The combined INS and Raman observations therefore indicate that this excitation arises from a phonon mode rather than from a magnetic crystal-field excitation. Phonons in this energy range are typically dominated by oxygen motions and strong metal-oxygen bonding, and their well-defined nature indicates that, despite the presence of low-energy lattice flexibility, the local Ru-O bonding remains robust. The high-energy Raman modes at 574 cm^{-1} and 774 cm^{-1} (72 and 95 meV) are assigned to A_1g symmetry modes corresponding to symmetric stretching vibrations of the RuO_6 octahedra. These modes are dominated by oxygen motion and reflect the intrinsic stiffness of Ru-O bonds. Similar high-energy stretching modes have been reported in

$SrRuO_3$, $CaRuO_3$, $Ca_3Ru_2O_7$, and related ruthenates [106, 107, 108]. Their well-defined nature indicates that, despite the presence of low-energy lattice flexibility, the local Ru-O bonding remains robust.

4.5.9 Calculation of Phonon excitation through MLFF

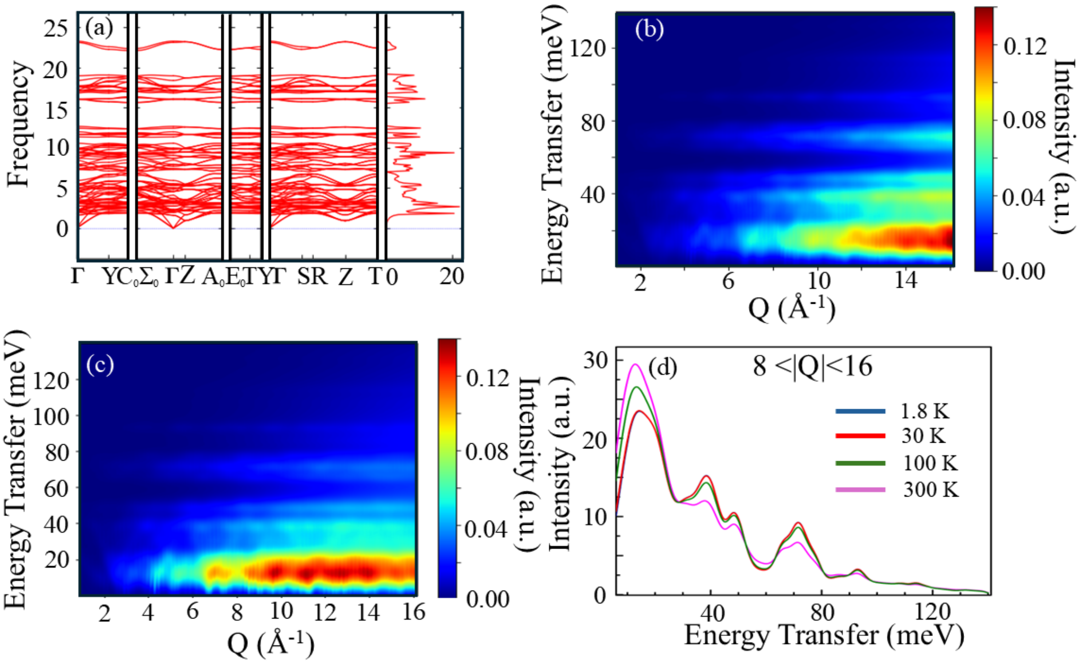

Figure 4.18: (a) Calculated phonon modes for $Ba_3HoRu_2O_9$ based upon pretrained MLFF. The vertical axis is the phonon energy in units of THz. Panels indicate wave-vector dependence in reciprocal space using standard reciprocal space. Calculated phonon scattering intensity (b) at 1.8 K, (c) at 300 K, and $|Q|$-integrated intensity versus energy transfer for temperatures between 1.8 and 300 K for $|Q| = 8$ to 16 $Å^{-1}$.

To distinguish lattice excitations from CEF excitations observed in the INS spectra of $Ba_3HoRu_2O_9$, we performed detailed phonon calculations using a MLFF approach. This methodology allows accurate modelling of lattice vibrations over the full Brillouin zone while retaining the accuracy of first principles calculations (e.g., *ab initio* DFT) that also reduce the computational cost [68]. The calculations were based on the experimentally determined low temperature crystal structure, which was first fully optimized to minimize residual forces. The resulting optimized structure exhibits no imaginary phonon frequencies, confirming its dynamical stability. Fig. 4.18(a) shows the calculated phonon dispersion relations plotted along standard high-symmetry directions in reciprocal space, with the phonon energies extending up to approximately 25 THz (∼100 meV). The dense distribution of excitation at low energies reflects the complex lattice dynamics arising from the coupled RuO_6 octahedra and the heavy Ba/Ho sublattices.

Using the MLFF we computed the powder-averaged dynamical structure factor, including one-phonon and multi phonon contributions, and convolved it with the instrumental energy and momentum resolution to allow direct comparison with the INS data. The simulated intensity map, shown in Fig.4.18(b-c), demonstrates that phonon scattering dominates the high-|Q| region ($8 \leq |Q| \leq 16$ Å^{-1}) [68]. The phonon calculations reveal several distinct phonon excitations that are closely spaced at low energies and therefore appear broad and unresolved below 50 meV in the experimental INS spectra, primarily due to the instrumental energy resolution and the dense phonon density of states. We have plotted the |Q|- integrated intensity vs temperature to indentify the energy of these excitation which is shown in Fig. 4.18(d). Well-resolved phonon excitations are identified at approximately 20 meV, 40 meV, 46 meV, 70-75 meV, and 90-95 meV, along with weaker features at intermediate energies. These calculated phonon energies are in good agreement with the experimentally observed INS excitations at high momentum transfer ($8 \leq |Q| \leq 16$ Å^{-1}). The simulated phonon intensity distribution shows that the excitation near 40 meV exhibits weak |Q| dependence at low-|Q| ($1 \leq |Q| \leq 8$ Å^{-1}), which cannot be explained by phonon scattering alone, suggesting an additional contribution from Ho^{3+} CEF excitations. In contrast, the emergence of multiple excitations at 20, 40, 46, 71, and 94 meV at high-|Q| has phononic origin. This clear separation of magnetic and lattice contributions provides a robust framework for interpreting the INS spectra of $Ba_3HoRu_2O_9$. The overlap between calculated phonon excitation and experimentally observed CEF energies provides strong evidence for CEF-phonon (vibronic) coupling near 40 mev in $Ba_3HoRu_2O_9$. Such coupling is expected when localized $4f$ excitations and lattice modes are present at similar energies and it can lead to renormalization of excitation energies, enhanced damping, and anomalous momentum dependence in INS spectra. The MLFF results therefore play a central role in establishing that the low-energy excitation spectrum of $Ba_3HoRu_2O_9$ cannot be understood by magnetic or lattice degrees of freedom alone but instead reflects a genuinely hybridized spin-lattice system.

4.5.10 Conclusion

Our study provides insights into the nature of magnetic ordering and spin dynamics around T_{N2} and, consequently, elucidate the mechanism of ME coupling and multiferroicity in this compound. We demonstrate that inverse D-M interaction between Ru($4d$) and Ho($4f$) spins related to the spin-structure of the 2nd magnetic phase transition breaks the inversion symmetry producing non-zero electric polarization. Additionally, we have explored the effect of external pressure, our results suggest that external pressure enhances the magnetic ordering, probably by reducing the magnetic phase competition. However, polarization measured through positive-up-negative-down (PUND) techniques was found to be very low [92]. To understand this behavior, we have investigated the spin and dipolar domain dynamics of $Ba_3HoRu_2O_9$ through a combination of dielectric characterization, AC magnetic susceptibility, and neutron time-of-flight measurements.

We have shown a comprehensive study of the magnetic and lattice excitations in the multiferroic 6H-perovskite $Ba_3HoRu_2O_9$ using inelastic neutron scattering, Raman spectroscopy, spin-wave simulations, and MLFF phonon calculations. Our INS measurements reveal a broad low-energy excitation below 6.2 meV that appears only below the lower magnetic transition temperature $T_{N2} \approx 10$ K. Spin-wave simulation results shows that this excitation is a collective excitation of the low-temperature K_2 magnetic phase, stabilized by strong Ru-Ru intradimer exchange together with Ru-Ho coupling, while no comparable low-energy mode exists in the higher-temperature K_1 phase. At higher energies, we identify multiple localized excitations below 90 meV persist over the entire temperature range and in which excitation observed near 40 meV is assigned to Ho^{3+} CEF transitions. Since Raman spectroscopy study and Machine-learned phonon calculations quantitatively reproduce the high-momentum INS spectra and confirm energy overlap between phonon branches and Ho^{3+} CEF levels, providing direct evidence for CEF-phonon coupling.

In contrast to other ruthenium compounds such as double perovskites (Sr_2DyRuO_6, Sr_2YbRuO_6, Ba_2DyRuO_6) or those 6H perovskite where R is non-magnetic ($Ba_3RRu_2O_9$, $R =$ La, Y, Ce) primarily either show conventional magnons or localized molecular excitations [59, 60, 61, 48, 49, 50]. $Ba_3HoRu_2O_9$ hosts a rare coexistence of collective $4d$-$4f$ coupled collective excitation, localized CEF excitations, and lattice vibrations that hybridize at same energy. These results establish $Ba_3HoRu_2O_9$ as a model platform for exploring emergent spin-lattice-orbital entanglement and hybrid excitations in correlated $4d$-$4f$ oxides, with direct relevance to multiferroicity and magnetoelastic phenomena.

Chapter 5

Magnetic structure, cooperative Ru($4d$)-Tb($4f$) spin-ordering and unconventional S-orbital state of Tb in $Ba_3TbRu_2O_9$

5.1 Motivation

This chapter focuses on the compound $Ba_3TbRu_2O_9$, which belongs to the $Ba_3RRu_2O_9$ family. It stands out within this family because Tb can stabilize an unusual +4 oxidation state, unlike most rare-earth ions that adopt a trivalent state. This leads to a single-valence Ru^{4+} ($4d^4$) configuration and fundamentally different $4d$-$4f$ exchange physics. Although Ce can also adopt a +4 oxidation state, recent neutron-scattering experiments have shown that Ce^{4+} has a non-magnetic ground state and that Ru does not magnetically order down to 2 K in $Ba_3CeRu_2O_9$. Earlier studies on $Ba_3TbRu_2O_9$ reported long-range antiferromagnetic ordering, but this ordering was attributed primarily to the Tb moments, and the spin state and magnetic moment of Ru^{4+} remain unresolved. Given that Ru^{4+} ($4d^4$) ions are highly sensitive to crystal-field effects, spin-orbit coupling, and local octahedral distortions, their magnetic ground state can range from a conventional spin-only state to a strongly spin-orbit-entangled one. The coexistence of tetravalent Tb, mixed $4d$-$4f$ interactions, and Ru dimers therefore raises the possibility of unconventional magnetism beyond a simple rare-earth-driven scenario. A detailed investigation of $Ba_3TbRu_2O_9$ is thus essential to clarify the role of Ru spin state, determine whether Ru participates in magnetic ordering, and understand how Tb^{4+} modifies the collective magnetic ground state in this strongly correlated 6H-perovskite system.

5.2 Introduction: A overview of $Ba_3TbRu_2O_9$

$Ba_3TbRu_2O_9$ crystallizes in the same hexagonal 6H-perovskite structure (space group $P6_3/mmc$), in which pairs of face-sharing RuO_6 octahedra form isolated Ru_2O_9 dimers that are connected through corner-sharing TbO_6 octahedra. The short Ru-Ru separation within each dimer (about 2.48 Å) leads to strong interactions between the two Ru ions, while the Ru-O-Tb-O-Ru superexchange pathway provides a natural route for coupling between the Ru $4d$ electrons and the Tb $4f$ moments. Because both Tb and Ru are magnetic in this compound, cooperative magnetism involving localized $4f$ moments and more extended $4d$ electrons has been anticipated, similar to what has been observed in $Ba_3HoRu_2O_9$.

Previous magnetic and thermodynamic studies have shown that $Ba_3TbRu_2O_9$ undergoes an antiferromagnetic transition at $T_N \approx 9.5$ K [57, 92]. Neutron diffraction experiments reported in the literature indicate that the Tb^{4+} moments form ferromagnetic layers within the ab plane that are stacked antiferromagnetically along the c axis, with the ordered moments pointing along c [57].

Earlier dielectric and magnetic measurements have also revealed that $Ba_3TbRu_2O_9$ exhibits pronounced MDE coupling. Both the real part of the dielectric constant $\varepsilon'(T)$ and the dielectric loss $\tan\delta(T)$ display clear anomalies at the magnetic ordering temperature, demonstrating that the magnetic and dielectric properties are strongly coupled. When a magnetic field is applied, these dielectric anomalies shift to lower temperatures, tracking the suppression of antiferromagnetic order and providing direct evidence that the dielectric response is controlled by the magnetic state [92].

Field-dependent dielectric studies further show a distinct anomaly in the excess dielectric constant $\Delta\varepsilon'(H)$ around 25-30 kOe at low temperatures. This field scale coincides with a hysteretic feature in the magnetization, indicating a magnetic-field-driven change in the spin configuration. The fact that this transition appears simultaneously in both magnetic and dielectric measurements demonstrates that changes in the magnetic ground state directly affect the lattice and the electronic polarizability. Even above T_N, a small but finite MD effect persists, pointing to the presence of short-range magnetic correlations that remain coupled to the lattice.

The MD coupling reported for $Ba_3TbRu_2O_9$ is unusually strong for a $4d$-electron system and is significantly larger than that found in related Nd-based compounds. This enhancement has been attributed to the large magnetic moment of Tb^{4+} and to strong $4d$-$4f$ exchange interactions mediated by the Ru-O-Tb-O-Ru superexchange pathway. Within this picture, magnetic ordering induces local lattice distortions and exchange-striction effects, which in turn generate changes in the dielectric response [92].

Taken together, earlier studies establish $Ba_3TbRu_2O_9$ as a particularly interesting 6H-perovskite in which tetravalent Tb magnetism, Ru^{4+} dimer physics, and strong MD coupling coexist. These results provide the essential background and motivation for the present neutron diffraction investigation, which aims to clarify the microscopic magnetic structure and the role of the Ru dimers in this unusual system. In this study, we have performed a detailed time-of-flight neutron diffraction experiment over a wide momentum transfer (Q-range¡ 1 $Å^{-1}$), which allows us to resolve the spin-structure and magnetic ground state of both Tb and Ru. The results reveal an unconventional spin-only ground state of Tb (orbital moment **L**=0, **J**=**S**=7/2) and spin-only moment of Ru (**S**=2, **L**=0).

5.3 Experimental details

The compound $Ba_3TbRu_2O_9$ was synthesized by solid-state-reaction using mixtures of high purity ($> 99.9\%$) precursors: $BaCO_3$, RuO_2, and Tb_4O_7 by mixing thoroughly using an agate mortar and pestle. The homogenized mixture was pressed into pellets and subjected to a series of calcination steps. The initial firing was carried out at 900 °C for 12 h, followed by successive heating at 1100 °C for 48 h, 1150 °C for 24 h, and a final sintering at 1180 °C for 12 h. After each heating cycle, the pellets were reground and repelletized to ensure phase homogeneity [57]. To check the phase purity X-ray diffraction was carried out using a lab-based Cu-Kα source from the Panalytical instrument. Magnetization (M) measurements were performed using a Superconducting Quantum Interference Device (SQUID, Quantum Design) as a function of temperature and magnetic field (H). Time-of-flight (TOF) Neutron diffraction data were collected at the SNAP beamline, a time-of-flight diffractometer at Spallation Neutron Source (SNS) in Oak Ridge National Laboratory (ORNL), USA. The magnetic structure was resolved using the FULLPROF and SARAH programs [63, 64]. X-ray Photoelectron Spectroscopy (XPS) measurements were carried out using a Thermo Fisher Scientific K-Alpha spectrometer equipped with a monochromatic Al Kα source (1486.6 eV, 10 kV, 10 mA). Scanning Electron Microscopy (SEM) imaging was conducted using a JEOL JXA-8230 electron probe micro-analyzer operated at an accelerating voltage of 20 kV. High-resolution high-angle annular dark-field scanning transmission electron microscopy (HAADF-STEM) was performed on the same JEM-ARM200F instrument operating at 200 kV. For sample preparation, a small amount of finely ground powder was dispersed in ethanol using ultrasonication for uniform mixing. A drop of the resulting suspension was then deposited onto a carbon-coated copper grid and allowed to dry at room temperature before imaging.

5.4 Results and discussion

5.4.1 Structural and Magnetic analysis

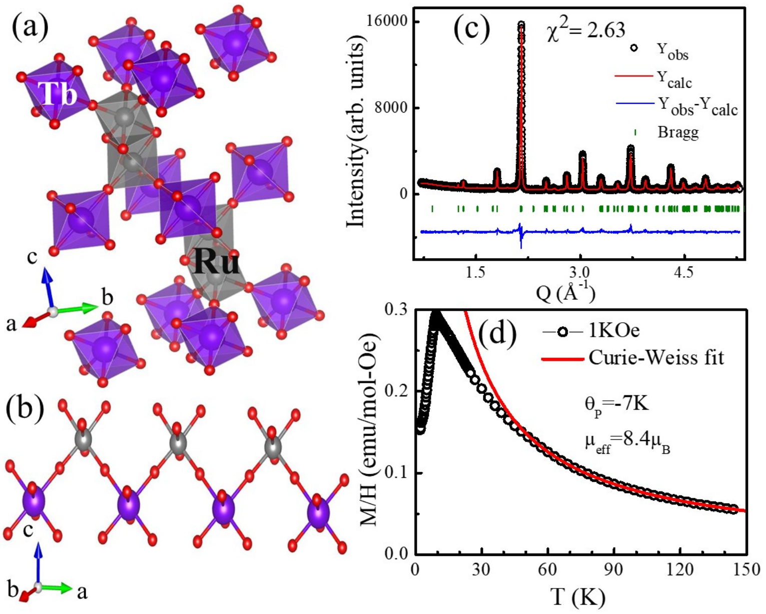

Figure 5.1: (a) Crystal structure of $Ba_3TbRu_2O_9$, (b) Tb–O–Ru–O–Tb exchange path, (c) Rietveld refinement of the room-temperature X-ray diffraction (XRD) data, and (d) DC magnetic susceptibility as a function of temperature measured under an applied magnetic field of 1 kOe.

The Rietveld refinement of the X-ray diffraction pattern is shown in Fig. 5.1(a), confirming a pure phase with space group $P6_3/mmc$. The Ru-Ru distance and Ru-O-Ru angle within the dimers are 2.56 Å and 79.26° respectively, indicating that Ru-Ru direct exchange interaction and Ru-O-Ru super-exchange interactions are competing within the Ru_2O_9-dimers. However, these dimers are connected via a magnetic Tb-atom in this compound. The Ru-O-Tb angle is 179.180°, implying a strong AFM super-exchange path, dominated over Ru-O-Ru exchange interaction. Therefore, the Ru-O-Tb-O-Ru superexchange path is responsible for magnetic ordering. To confirm the elemental composition and homogeneous distribution of constituent elements in the $Ba_3TbRu_2O_9$powder sample, we performed scanning electron microscopy (SEM) with energy- dispersive X-ray spectroscopy (EDS) and high-resolution high-angle annular dark-field scanning transmission electron microscopy (HAADF-STEM). The SEM-EDS and HAADF-STEM images are shown in Fig. 5.2 and 5.3. The SEM-EDS and HAADF-STEM elemental maps confirm a uniform spatial distribution of Ba, Ru, Tb, and O across the sample, confirming the

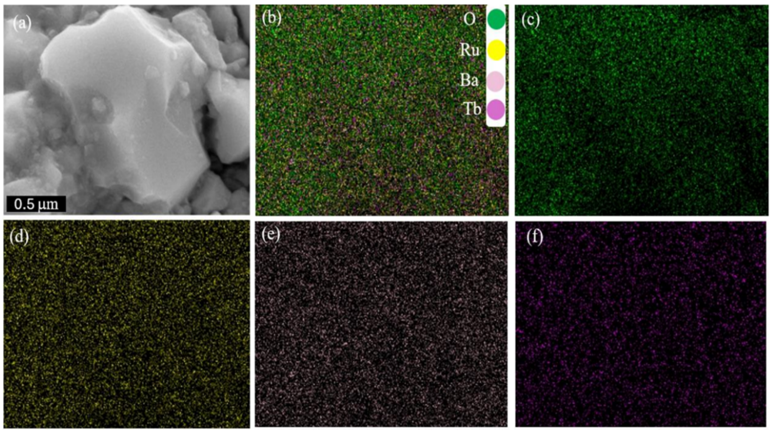

Figure 5.2: (a)Backscattered electron Backscattered electron image, and EDX maps display (b) the mixing of Ba, Tb, Ru and O, (c) O, (d) Ru, (e) Ba and (f) Tb of $Ba_3TbRu_2O_9$ powder sample.

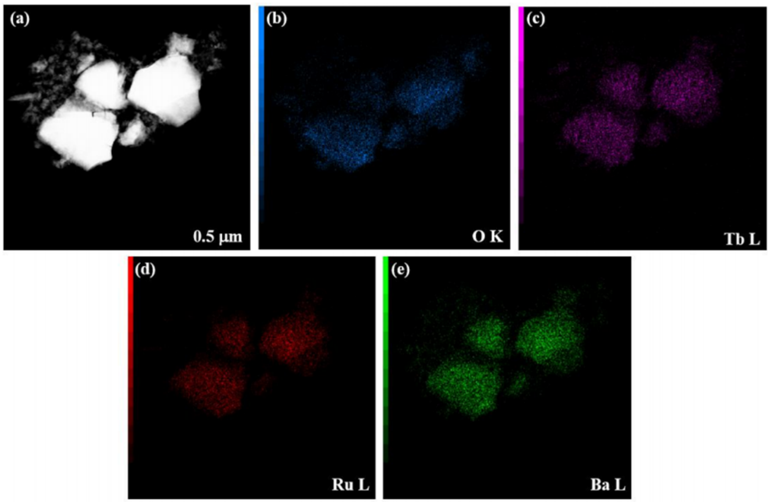

Figure 5.3: (a) HAADF-STEM image of polycrystalline $Ba_3TbRu_2O_9$, showing well-defined grains with sharp boundaries. Elemental mapping obtained from EDS analysis: (b) oxygen (O K), (c) terbium (Tb L), (d) ruthenium (Ru L), and (e) barium (Ba L).

homogeneity of the sample. The EDS results show that the atomic percentage ratio for Ba:Tb:Ru:O from EDS is 22.0 : 7.2 : 15.5 : 60.6 ($\approx$ 3.1 : 1 : 2.1 : 8.4) which agrees with the stoichiometry of the compound within the resolution limit of the instrument.

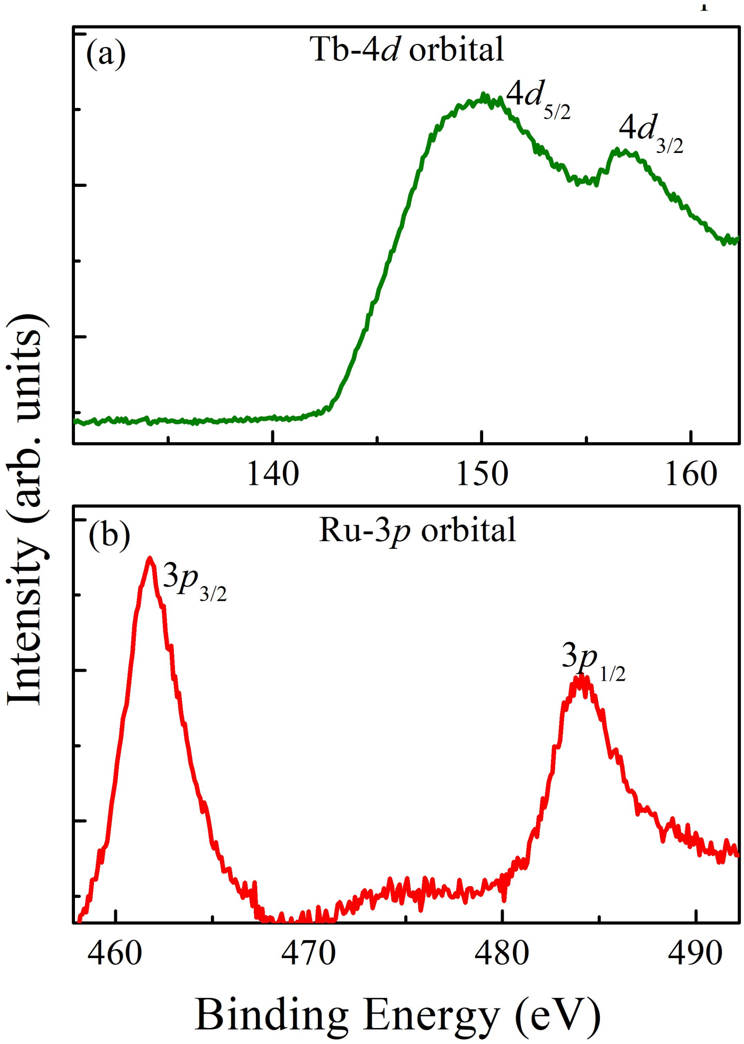

Figure 5.4: X-ray photoelectron spectroscopy (XPS) spectra of $Ba_3TbRu_2O_9$: (a) Tb $4d_{5/2}$ and $4d_{3/2}$ core-level peaks, and (b) Ru $3p_{3/2}$ and $3p_{1/2}$ core-level peaks.

The temperature-dependent magnetic susceptibility under a 1 kOe magnetic field in zero-field-cooled conditions is shown in Fig.5.1(b). The results reveal antiferromagnetic (AFM) ordering below 9.5 K (T_N), consistent with an earlier report [57]. The Curie-Weiss fitting in the paramagnetic region yields an effective moment (μ_{eff}) of approximately 8.4 μ_B. This low value of μ_{eff} not be satisfied with Tb^{3+} moment with effective quantum number $\mathbf{J} = 6$, which gives $\mu_{\text{eff}} \approx 9.72\ \mu_B$. These results suggest that Tb has a spin configuration of $\mathbf{S} = 7/2$, adopting Tb^{4+} valence state, where $\mathbf{S}$ is the principal spin quantum number and the orbital moment $\mathbf{L} = 0$ for a half-filled shell. The theoretical value of the effective moment for $\mathbf{S} = 7/2$ is 7.94 μ_B. The experimentally calculated effective magnetic moment per Ru atom is approximately 1.94 μ_B, based on the relation:

$$\mu_\mathrm{eff}^2 = \mu_\mathrm{Tb}^2 + 2\mu_\mathrm{Ru}^2$$

To check the oxidation states of Tb and Ru we have performed XPS of the sample (shown in Fig. 5.4). The binding energy values of Tb $4d_{\frac{5}{2}}$ is 150.3 eV and $4d_{\frac{3}{2}}$ is 157.8 eV and For Ru $3p_{\frac{3}{2}}$ is 461.7 eV and $3p_{\frac{1}{2}}$ is 484.2 eV which are close to the values reported in the literature [109, 110]. However, it should be noted that the binding energy difference between two oxidation states of Ru-atom is only nearly 1 eV, and such a small difference may also arise for the same oxidation state in different crystallographic environments [110, 111]. However, if the valence state is a mixture of +4 and +5, we would observe two separate nearby peaks or a very broad peak, whereas, here we observe a single peak due to single valence state as similarly observed in the literature [109, 110, 111, 112].

5.4.2 Magnetic Structure Resolved by TOF Neutron Diffraction

To solve the magnetic structure, we have performed temperature dependent (2, 4, 6, 7, 8, 9, 10, 12, 14, 16, 20, 50, and 100 K) time-of-flight neutron diffraction (ND) measurements and collected data over a wavelength band covering 3.7-6.5 Å, corresponding to a momentum transfer coverage between 1 Å^{-1} and 2 Å^{-1} (shown in Fig. 5.4(a)).A significant enhancement of the intensity of the (101) and (103) Bragg peaks (at $\mathbf{Q} = 1.44$ Å^{-1} and 1.86 Å^{-1} respectively) below $\mathrm{T_N}$. No change in diffraction intensity is observed above $\mathrm{T_N}$. The magnetic reflections of both Bragg peaks (101) and (103)) at various temperatures are shown in Fig. 5.4(b-c). The magnetic intensities are calculated by subtracting the data collected at 2-11 K from the 100 K data which contains the purely nuclear contribution. The temperature dependence of the integrated magnetic intensity is shown in Fig. 5.4(d), which represents the magnetic order parameter. The magnetic intensity increases with decreasing temperature below T_N due to saturation of magnetic moments with lowering the temperature as usual. We did not observe any additional magnetic Bragg reflections at low-T in this Q-range. Therefore, we have further performed the experiments over a broader **Q**-range (for wavelength range 0.5-3.65 Å) at a few selected temperatures (100, 50, 20, and 2 K). Interestingly, 2 K diffraction profile shows a few extra peak intensities at $\mathbf{Q} = 1.44, 1.86, 2.19, 2.52, 3.30$ and 3.53 Å^{-1} corresponding to reflections (101), (103), ($\bar{2}$11), (105), (213) and (210) respectively compared to the high temperature diffraction profile above $\mathrm{T_N}$, shown in Fig. 5.5(a). The neutron diffraction profile measured at 100 K in the paramagnetic region is well-fitted for the reported space group $P6_3$/mmc, confirming the sample phase (see Fig. 5.5(b)). All the additional magnetic reflections can be indexed using the propagation vector $\mathbf{k} = (0\ 0\ 0)$.

Table 5.1: Basis vectors for the space group $P6_3/mmc$ for $K = (0\,0\,0)$. The decomposition of the magnetic representation for the Tb site $(0, 0, 0)$. The atoms of the nonprimitive basis are defined as 1: $(0, 0, 0)$ and 2: $(0, 0, 0.5)$.

IR	BV	Atom	BV Components					
			$m_{\|a}$	$m_{\|b}$	$m_{\|c}$	$im_{\|a}$	$im_{\|b}$	$im_{\|c}$
Γ_1	ψ_1	1	0	0	12	0	0	0
		2	0	0	12	0	0	0
Γ_2	ψ_2	1	0	0	12	0	0	0
		2	0	0	−12	0	0	0
Γ_3	ψ_3	1	0	−3	0	0	0	0
		2	0	−3	0	0	0	0
Γ_4	ψ_4	1	−3.464	−1.732	0	0	0	0
		2	−3.464	−1.732	0	0	0	0
Γ_5	ψ_5	1	0	−3	0	0	0	0
		2	0	3	0	0	0	0
Γ_6	ψ_6	1	−3.464	−1.732	0	0	0	0
		2	3.464	1.732	0	0	0	0

Table 5.2: Basis vectors for the space group $P6_3/mmc$ for $K = (0\ 0\ 0)$. The decomposition of the magnetic representation for the Ru site $(.33333, .66667, .16223)$. he atoms of the nonprimitive basis are de- fined according to 1: $(.33333, .66667, .16223)$, 2: $(.66666, .33333, .66223)$, 3: $(.66667, .33334, .83777)$, 4: $(.33333, .66667, .33777)$.

IR	**BV**	**Atom**	**BV components**					
			$m \parallel a$	$m \parallel b$	$m \parallel c$	$im \parallel a$	$im \parallel b$	$im \parallel c$
Γ_2	ψ_1	1	0	0	6	0	0	0
		2	0	0	6	0	0	0
		3	0	0	-6	0	0	0

IR	**BV**	**Atom**	**BV components**					
			$m \parallel a$	$m \parallel b$	$m \parallel c$	$im \parallel a$	$im \parallel b$	$im \parallel c$
		4	0	0	-6	0	0	0
Γ_3	ψ_2	1	0	0	6	0	0	0
		2	0	0	6	0	0	0
		3	0	0	6	0	0	0
		4	0	0	6	0	0	0
Γ_6	ψ_3	1	0	0	6	0	0	0
		2	0	0	-6	0	0	0
		3	0	0	-6	0	0	0
		4	0	0	6	0	0	0
Γ_7	ψ_4	1	0	0	6	0	0	0
		2	0	0	-6	0	0	0
		3	0	0	6	0	0	0
		4	0	0	-6	0	0	0
Γ_9	ψ_5	1	0	-1.5	0	0	0	0
		2	0	-1.5	0	0	0	0
		3	0	-1.5	0	0	0	0
		4	0	-1.5	0	0	0	0
Γ_9	ψ_6	1	-1.732	-0.866	0	0	0	0
		2	-1.732	-0.866	0	0	0	0
		3	-1.732	-0.866	0	0	0	0
		4	-1.732	-0.866	0	0	0	0
Γ_{10}	ψ_7	1	3	1.5	0	0	0	0
		2	3	1.5	0	0	0	0
		3	-3	-1.5	0	0	0	0
		4	-3	-1.5	0	0	0	0
Γ_{10}	ψ_8	1	0	-2.598	0	0	0	0
		2	0	-2.598	0	0	0	0
		3	0	2.598	0	0	0	0

IR	**BV**	**Atom**	**BV components**					
			$m \parallel a$	$m \parallel b$	$m \parallel c$	$im \parallel a$	$im \parallel b$	$im \parallel c$
		4	0	2.598	0	0	0	0
Γ_{11}	ψ_9	1	0	-1.5	0	0	0	0
		2	0	1.5	0	0	0	0
		3	0	-1.5	0	0	0	0
		4	0	1.5	0	0	0	0
Γ_{11}	ψ_{10}	1	-1.732	-0.866	0	0	0	0
		2	1.732	0.866	0	0	0	0
		3	-1.732	-0.866	0	0	0	0
		4	1.732	0.866	0	0	0	0
Γ_{12}	ψ_{11}	1	3	1.5	0	0	0	0
		2	-3	-1.5	0	0	0	0
		3	-3	-1.5	0	0	0	0
		4	3	1.5	0	0	0	0
Γ_{12}	ψ_{12}	1	0	-2.598	0	0	0	0
		2	0	2.598	0	0	0	0
		3	0	2.598	0	0	0	0
		4	0	2.598	0	0	0	0

The Wyckoff positions of the magnetic Tb and Ru ions are 2a (0, 0, 0) and 4f (0.33333, 0.66667, 0.16223), respectively. To evaluate the possible magnetic structures consistent with the crystallographic symmetry, we performed an irreducible representational analysis using the SARAh program [64]. The resulting irreducible representations (IRs) and basis vectors (BVs) for the Ru and Tb sites are presented in Tables-5.1 and 5.2. There are four irreducible representations for Tb and eight for Ru. The magnetic representation is given by:

$$\Gamma_{\text{mag}}(\text{Tb}) = 1\Gamma_3^1 + 1\Gamma_7^1 + 1\Gamma_9^2 + 1\Gamma_{11}^2$$

$$\Gamma_{\text{mag}}(\text{Ru}) = 1\Gamma_2^1 + 1\Gamma_3^1 + 1\Gamma_6^1 + 1\Gamma_7^1 + 1\Gamma_9^2 + 1\Gamma_{10}^2 + 1\Gamma_{11}^2 + 1\Gamma_{12}^2$$

Since neutrons interact with the magnetic moment component perpendicular to the mo-

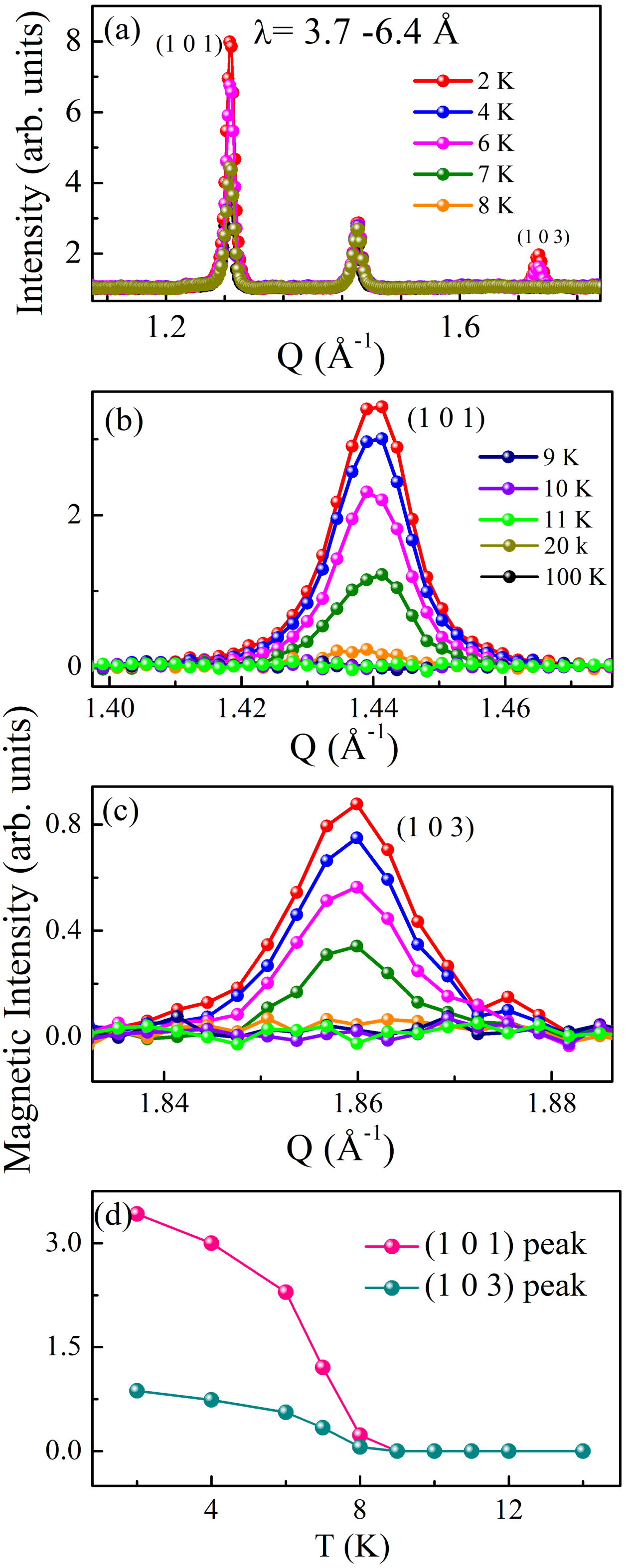

Figure 5.5: Time-of-flight (TOF) neutron diffraction data of $Ba_3TbRu_2O_9$ measured at various temperatures: (a) TOF pattern collected in the wavelength range $\lambda = 3.7–6.4$ Å. Temperature-dependent magnetic intensities of the (b) (101) and (c) (103) Bragg reflections, and (d) magnetic intensity as a function of temperature.

mentum transfer (**Q**), the significant difference in intensity of the (1 0 1), (1 0 3), (1 0 4), (1 1 0), (1 0 5), (2 1 0) Bragg peak between 2 K and 100 K suggests that the magnetic moment should have a dominant contribution along *b*-axis. However, the presence of strong magnetic reflection for (2 1 0) and (-2 1 1) indicates there should be magnetic component along *c*-axis as well.

We could not achieve a suitable refined structure considering Γ_2, Γ_6,Γ_{10} and, Γ_{12}, ruling out the possibilities of a non-magnetic terbium (because, only ruthenium contributes for these particular basis vectors). We have attempted to fit the data using Γ_3, Γ_7, Γ_9 and Γ_{11} where both Tb and Ru moments contributes. For terbium, $(\Gamma_9)(\Psi_4)$ and $(\Gamma_{11})(\Psi_6)$ have magnetic moment in ab- plane and $\Gamma_3(\Psi_1)$ and $\Gamma_7(\Psi_2)$ have magnetic moment in *c*- axis (Table 5.1). For ruthenium, $\Gamma_9(\Psi_5)$ and $\Gamma_{11}(\Psi_9)$ have a magnetic moment along *b*-axis, $\Gamma_9(\Psi_6)$ and Γ_{11} (Ψ_{10}) have a magnetic moment in ab- plane and $\Gamma_3(\Psi_2)$ and $\Gamma_7(\Psi_5)$ have a magnetic moment in *c*- axis(Table 5.2)The best fit to the data is achieved using a combination of $\Gamma_{11}(\Psi_9)$ for Ru and $\Gamma_7(\Psi_2)$, $\Gamma_{11}(\Psi_5)$ for Tb. The corresponding Shubnikov space group, which is the magnetic space group of the paramagnetic space group $P6_3/mmc$ with $\mathbf{k} = (0, 0, 0)$, is P$6_3'/m'm'c$. The Rietveld refinement of 2 K data is shown in Fig. 5.5(c). The enlarged view of selected nuclear and magnetic peaks are shown in the inset of Fig. 5.5(c). The fittings parameters are:$\chi^2 = 9.8$ $R_\mathrm{p} = 2.87$, $R_\mathrm{wp} = 4.27$, $R_\mathrm{exp} = 1.11$, and magnetic R-factor, $R_\mathrm{mag} = 5.14$. which indicate the good fitting of the data. The magnetic structure obtained from this refinement is shown in Fig. 5.7(a). The results reveal that the Ru moments are ordered along the b-direction with a magnetic moment of $1.96\mu_B$, and the Tb moments are ordered in the bc-plane (small canting of 15.9° with *c*-axis) with a magnetic moment of $6.18\mu_B$.The moment associated with terbium and ruthenium are tabulated in Table-5.3.The fit of the magnetic structure was further checked by setting the Ru moment to zero and refining the Tb moments allowing it to achieve its maximum value; this however, does not result in a good fit. The refined magnetic structure results in a terbium with $6.18 \pm (0.04)$ μ_B (close to **S**=7/2) and a spin-only moment of ruthenium (**S**=1).

In most of the $4d$-$4f$ the transition metal ion first orders at higher temperature, followed by the rare-earth ordering at lower temperature[38, 42].Interestingly, here, we observe the rare cooperative ordering of Ru($4d$) and Tb($4f$) moments below T_N, which is attributed to strong $4d$-$4f$ coupling in this system. The Ru-moments are collinearly arranged antiferromagnetically along the *b*-axis for the title compound (Fig. 5.7(a)). For

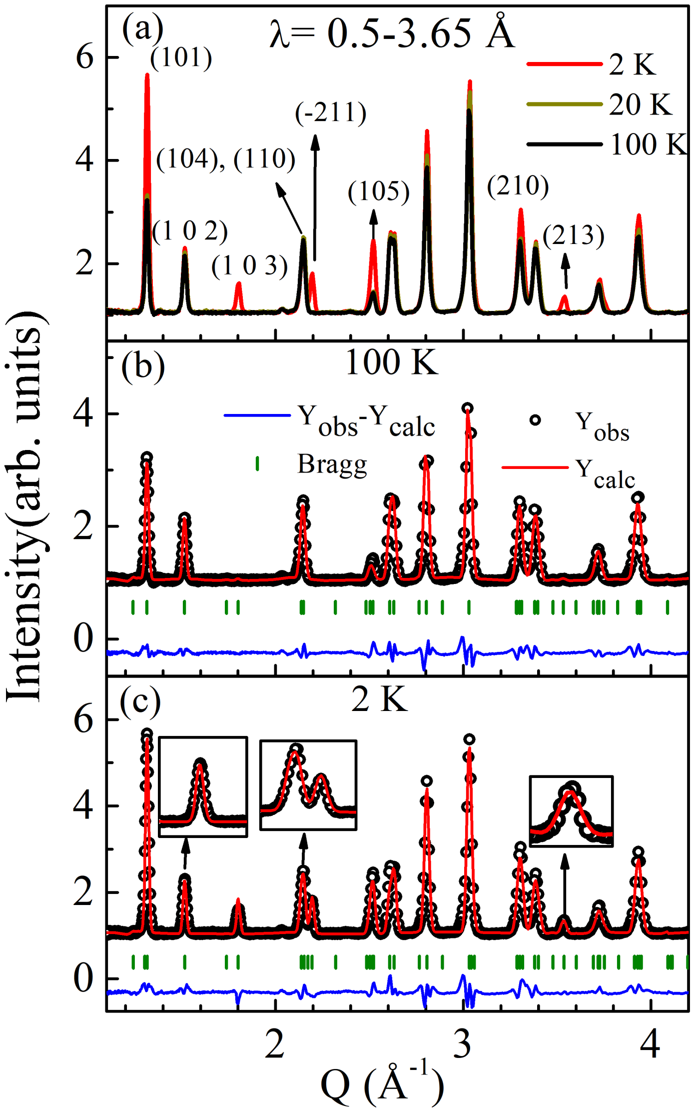

Figure 5.6: Time-of-flight (TOF) neutron diffraction data of $Ba_3TbRu_2O_9$ measured at various temperatures: (a) TOF pattern collected over the wavelength range $\lambda = 0.5$–6.5 Å, (b) Rietveld refinement of the TOF data at 100 K, and (c) Rietveld refinement at 2 K. The inset in (c) shows an enlarged view of the profile fitting. The magnetic and nuclear Bragg reflections appear at the same positions due to the propagation vector $\mathbf{k} = (0\,0\,0)$.

$Ba_3HoRu_2O_9$ compound, the ruthenium network exhibits a canted AFM spin-structure within Ru_2O_9 dimers below magnetic ordering [62].The Ru-spins are arranged ferromagnetically within Ru_2O_9 dimers for Nd-members, and ferromagnetic dimers are arranged antiferromagnetically [58]. The strong spin-orbit coupling and strong $4d$-$4f$ correlation is reported in heavy-rare-earth member $Ba_3HoRu_2O_9$. Surprisingly, being a heavy rare-earth member, the Tb possesses an **S**=7/2 ground state (f^7) with zero orbital moment, adopting an unusual +4 valence state, which is characterized as an *s*-state. more commonly observed for Gd^{3+} ions, which have f^7electronic configurations.

The Tb possesses a +4-valence state, contrary to the usual +3 valence state of R-ions in this whole family. Most likely, the energy is minimized by adopting this spin-configuration similar to the related Gd^{3+}. The spin configurations for Tb and Ru spins are shown in Fig. 5.6(b-c). The slightly smaller value of the refined Tb moment compared to its theoretical spin-only value of 7/2 could be due to two reasons: i) the Landé g-factor might be slightly lower than 2 (the ideal value for a free electron's spin-only moment) in this strongly correlated electron system with complex magnetic interaction; and/or ii) the moments may not be fully saturated even at 2 K, although this is unlikely. Interestingly, unlike other R-members in this series where a reduced Ru-moment is generally observed, our results yield an almost full moment for Ru (1.96 μ_B) [58, 62]. We did not observe any molecular-like magnetic state as observed in $Ba_3YRu_2O_9$or a selective-orbital state similar to $Ba_3LaRu_2O_9$ [59, 60].

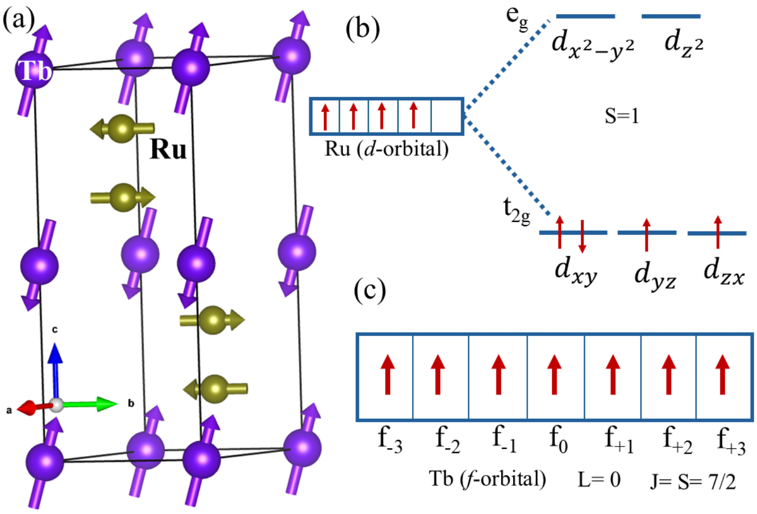

Figure 5.7: (a) Magnetic Structure of $Ba_3TbRu_2O_9$, Spin-configuration for (b) Ru and (c) Tb spins in $Ba_3TbRu_2O_9$

Table 5.3: Refined magnetic moment components m_a, m_b, and m_c along crystallographic a, b, c directions and total magnetic moment (m_{total}) for Tb and Ru atoms in $Ba_3TbRu_2O_9$, obtained from FullProf magnetic structure refinement.

Atom	m_a	m_b	m_c	$m_{\textbf{total}}$
Tb	0	±1.69200	±5.9520	6.18782
Ru	0	±1.96050	0	1.96050

5.5 Conclusion

In summary, we resolve the spin-structure of the $Ba_3TbRu_2O_9$ compound and observe a unique magnetic ground state for both terbium and ruthenium in $Ba_3TbRu_2O_9$, distinct from all other lanthanide members in this series. The $4f$ orbitals of Tb behave like those of an s-state ion, exhibiting zero orbital moment ($\mathbf{L}$=0). Our neutron diffraction results reveal that the magnetic moment of Ru-atom is almost 2 μ_B manifesting a $\mathbf{S}$=1 magnetic ground state, in contrast to a reduced moment of ruthenium in all other members in this family. We also report a cooperative spin-ordering of both Ru and Tb, not commonly observed in d-f coupled systems.

Chapter 6

Investigation of temperature dependent crystal and magnetic structure of $Ba_3SmRu_2O_9$

6.1 Motivation and Introduction

In the series of $Ba_3RRu_2O_9$ compounds, the ionic radius of the rare-earth element, its magnetic moment and the strength of 4d-4f coupling plays a crucial role on deciding the magnetic ground state. Systematic studies on this series of compounds reveal that heavy rare-earth members such as Ho and Tb exhibit strong MD coupling and cooperative magnetic ordering whereas the light rare-earth compound Nd shows ferromagnetic ordering [57, 58, 62]. Interestingly, Ce stabilizes in a +4 oxidation state and exhibit nonmagnetic ground state. Another notable feature in this family is the presence of a broad hump in magnetic susceptibility for nonmagnetic rare-earth compounds such as La, Y, and Lu, which is generally attributed to short-range magnetic correlations within the Ru_2O_9 dimers [59, 60]. Moreover, this broad feature is absent in compounds containing magnetic rare-earth ions such as Nd, Tb, and Ho, where long-range magnetic ordering dominates the low-temperature behavior. In $Ba_3SmRu_2O_9$, despite Sm is magnetic, a broad hump similar to La, Y, and Lu is observed [59, 60]. The present study aims to understand the magnetic ground state evolves in $Ba_3SmRu_2O_9$ being intermediate member of this rare earth series. In particular, we investigate the role of weak $4f$ magnetism in $4d$-$4f$ coupling and magnetic ordering. Previous bulk measurements performed on this compound reveal a clear magnetic transition around 12.5 K that indicate the onset of long-range antiferromagnetic order [92].

6.2 Experimental details

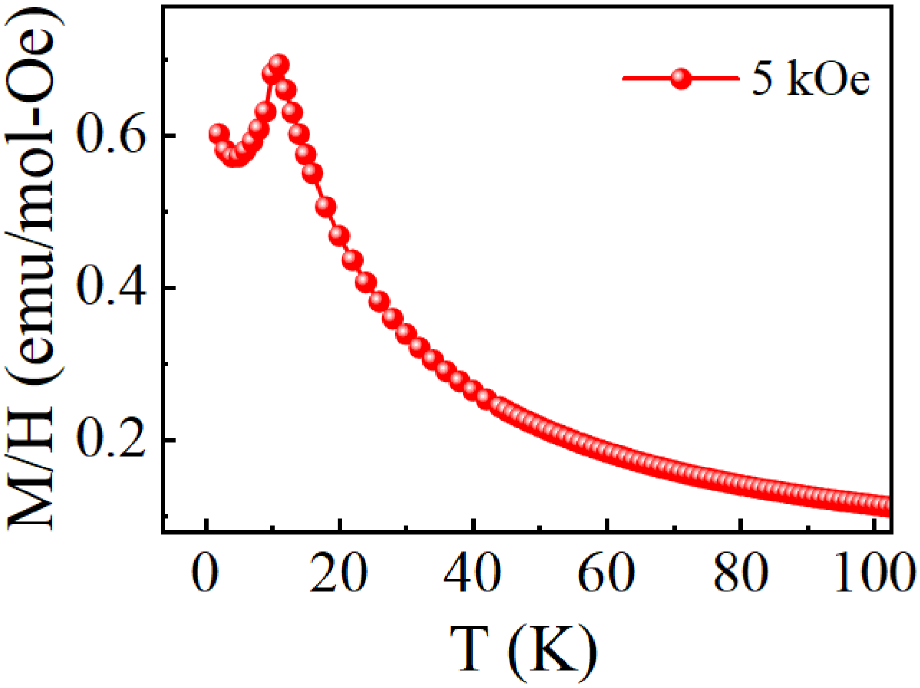

Figure 6.1: DC magnetic susceptibility as a function of temperature measured under an applied magnetic field of 5 kOe

Studying neutron scattering involving naturally occurring elements like Sm, Eu, and Gd poses significant challenges due to their exceptionally high absorption cross sections. These elements exhibit large thermal neutron absorption coefficients, with values reaching 5922, 4530, and 49,700 barns respectively at a wavelength of 1.798 Å. Despite this obstacle, some isotopes of these elements have relatively small absorption cross sections. To overcome this issue, we employ powder samples that are prepared using ^{152}Sm isotope, which is sensitive to Neutron. We obtained the sample $Ba_3SmRu_2O_9$ (with ^{152}Sm isotope) from CRISMAT Laboratory, CNRS, France through collaborations. The basic characterization through preliminary XRD and Magnetic measurements confirms the phase purity of the samples, as described in Ref[57, 92]. Fig. 6.1 shows that temperature dependent DC magnetization, which documents the expected magnetic ordering around 12 K. Initially, neutron powder diffraction measurements were carried out on the two-axis diffractometer G4.1 at the Laboratoire Léon Brillouin (LLB), France, with an incident neutron wavelength of 2.425 Å. The same sample has been used ton perform temperature-dependent high-resolution X-ray diffraction (HRXRD) measurements at the CRISTAL beamline of the SOLEIL synchrotron (France), using an X-ray source with a wavelength of $\lambda = 0.58182$ Å. The magnetic structure was determined using the FullProf and Sarah programs[63, 64].

6.3 Results and Discussions

6.3.1 Synchrotron X ray Diffraction

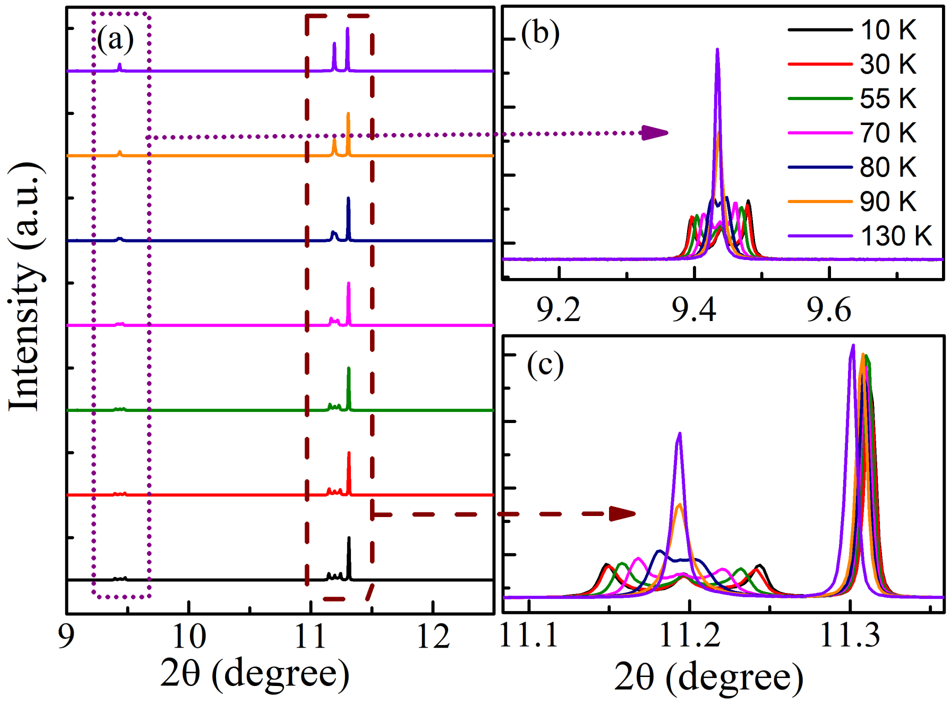

Figure 6.2: Synchrotron XRD data at different temperature

We have performed high-resolution, temperature-dependent synchrotron X-ray diffraction (HRXRD) measurements on $Ba_3SmRu_2O_9$ over a temperature range from 6 to 130 K. Fig. 6.2(a) shows the comparison of diffraction patterns collected between 10 and 130 K which suggest that below 90 K some of the Bragg peaks split into three distinct peaks, indicating a structural distortion. Fig. 6.2(b-c) show enlarged views of the (0 2 3) and (0 2 4) Bragg peaks, which split into the pairs $(-1\ 1\ 3)/(1\ 1\ 3)$ and $(-1\ 1\ 4)/(1\ 1\ 4)$, respectively. We have performed the Rietveld refinement on 90 K data using the reported hexagonal space group $P6_3/mmc$ which is shown in Fig. 6.3(c) [63]. However, below this temperature, refinement using the same space group does not provide satisfactory results suggesting lower-symmetry model. Initially, we use a monoclinic C2/c space group similar

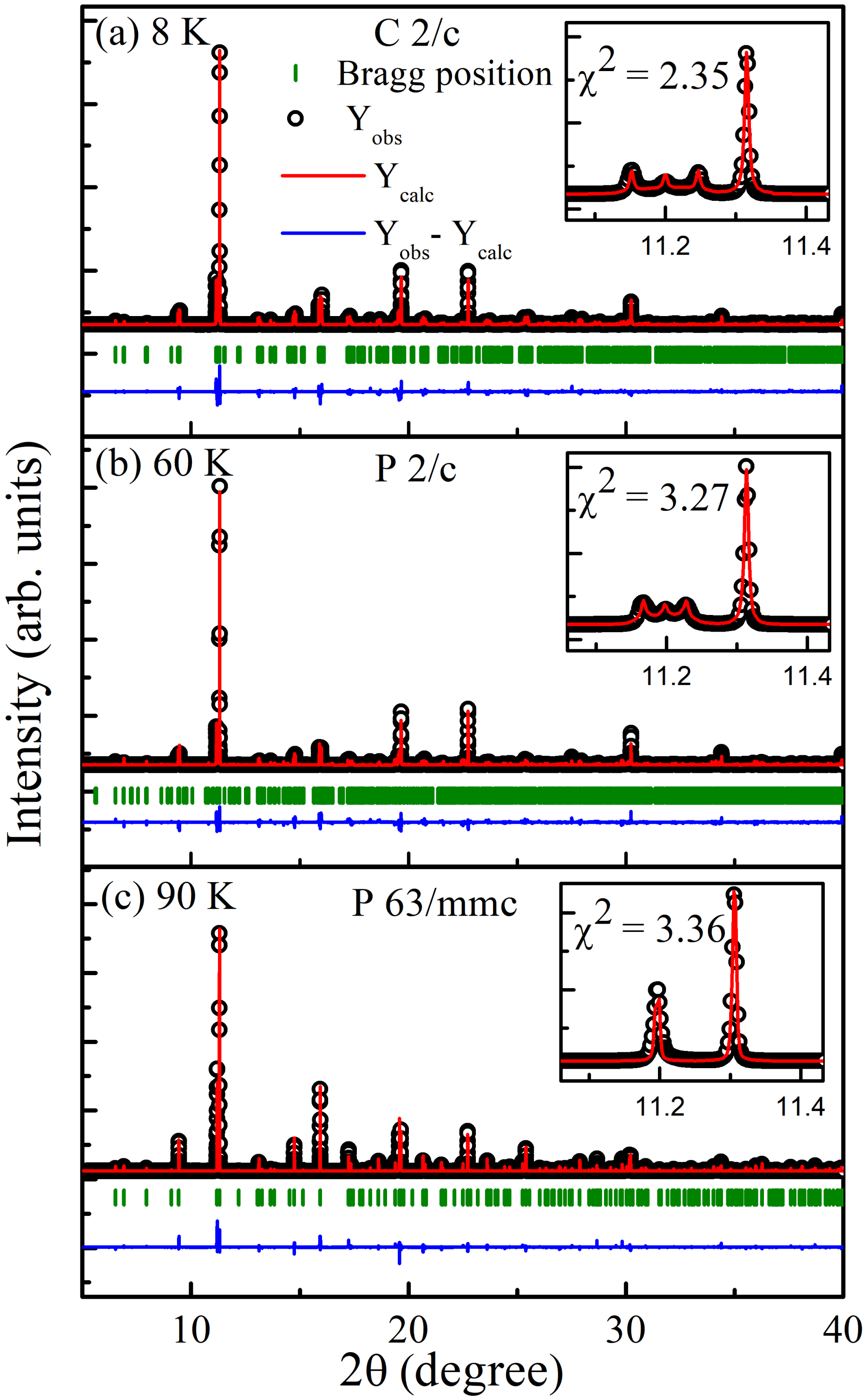

Figure 6.3: Reitvield Refinement of HRXRD data $Ba_3SmRu_2O_9$ (a) 8 K (C2/c space group), (b) at 60 K (P2/c space group) and (c) at 90 K ($P6_3/mmc$ space group)

to that observed in $Ba_3NdRu_2O_9$, that yield good fitting at low temperatures (8 K) [58]. While for the intermediate temperatures (65-85 K), a better fit was obtained using the P2/c space group analogous to $Ba_3NaRu_2O_9$ [113]. These refinements confirm a structural transition from $P6_3/mmc$ to monoclinic symmetry (P2/c and C2/c) below 90 K (See Fig. 6.3(a-b). The difference between P2/c and C2/c is the presence of two crystalograficially inequivalent Ru sites (Ru1 and Ru2) in P2/c.The crystal structure obtained after the refining the data using both space group is shown in Fig. 6.4(a-b). Fig. 6.4 and Fig. 6.5 shows the two distinct $(Ru1)_2O_9$ and $(Ru2)_2O_9$ dimers in the P2/c structure, in which the $(Ru2)_2O_9$ dimer exhibits significantly more distortion compared to the $(Ru1)_2O_9$ dimer. This asymmetric distortion of the Ru dimers can be understood in terms of spin-lattice coupling and electronic instability within the Ru-Ru dimers. In mixed-valence or correlated dimer systems, lowering of symmetry can lifts the degeneracy of Ru-Ru bonding and anti-bonding states, leading to unequal Ru-O bond lengths and enhanced octahedral distortion in one of the dimers [18, 113]. Such behavior has been reported in $Ba_3BiRu_2O_9$, $Sr_3CaRu_2O_9$ ruthenate dimer system, where structural distortions act to stabilize specific magnetic or orbital configurations through magneto-elastic coupling [93, 114]. In the intermediate P2/c phase, the pronounced distortion of the $(Ru2)_2O_9$ dimer indicates that the two $(Ru2)_2O_9$ dimers behave differently, leading to unequal electronic and magnetic responses. In both monoclinic phases, the structure consists of four face-sharing RuO_6 octahedra forming Ru_2O_9 dimers that are connected to a central SmO_6 octahedron. In

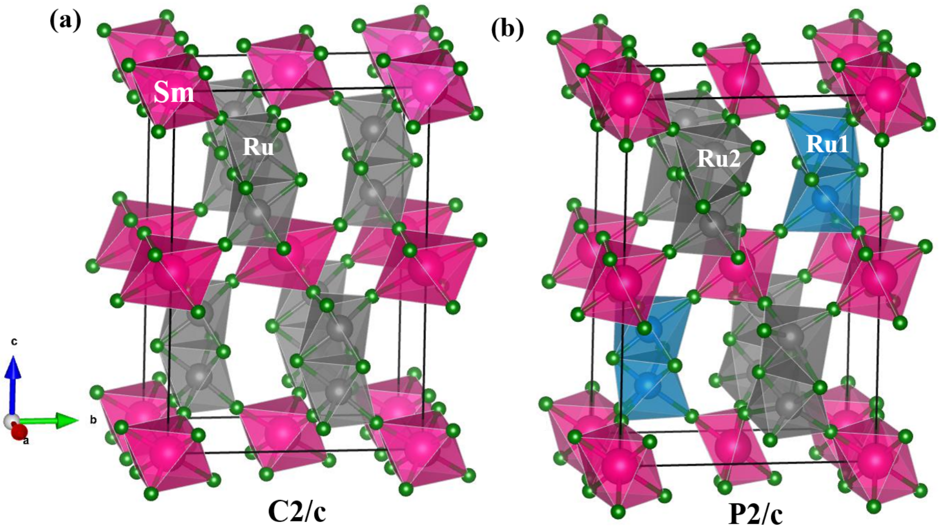

Figure 6.4: Crystal structure of $Ba_3SmRu_2O_9$ obtained after refining the HRXRD for (a) C2/c and (b) P2/c space group

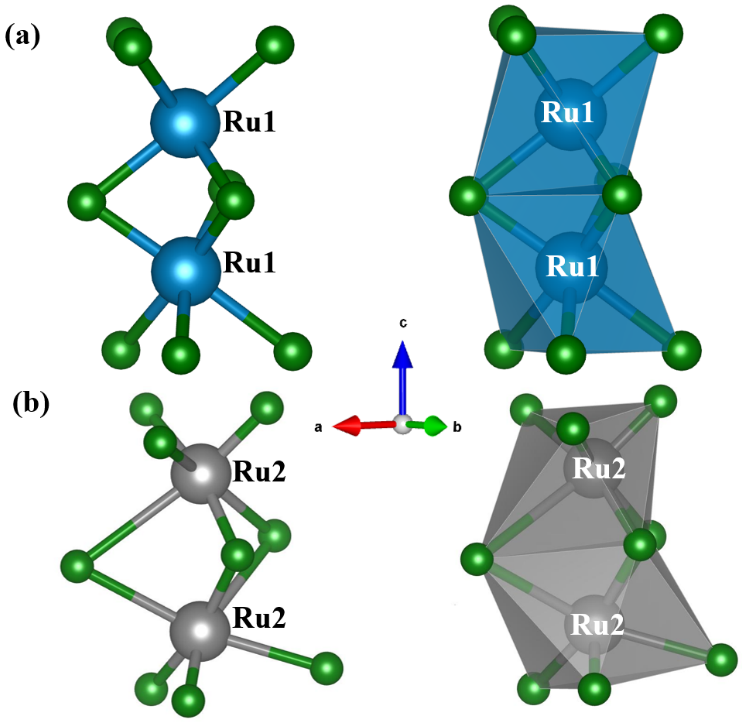

Figure 6.5: (a) $(Ru1)_2O_9$ and (b) $(Ru2)_2O_9$ dimers

the C2/c phase, the RuO_6 octahedra are coordinated by oxygen atoms occupying five distinct crystallographic sites that results relatively weak and uniform octahedral distortions. In contrast to this the P2/c phase has ten crystallographically distinct oxygen positions, which lead to enhanced local distortions and bond-length asymmetry, within the $(Ru2)_2O_9$ dimer. This increased distortion suggests that the P2/c phase represents a structurally unstable intermediate state between the high-symmetry hexagonal phase and the fully stabilized low-temperature C2/c phase. The temperature dependence of the lattice parameters a, b, and c, along with the unit cell volume V, in the range of 6-60 K, is shown in Fig. 6.6(a-d). As the temperature decreases from 60 K to 6 K, all three lattice parameters exhibit a gradual reduction, which is a typical signature of thermal contraction. This behavior arises due to the reduced atomic vibrational energy at lower temperatures, that leads to a decrease in interatomic spacing and a more compact crystal lattice. Around 12 K, a noticeable deviation from this smooth contraction behavior is observed in all lattice parameters and in the unit cell volume. This anomaly coincides with the known antiferromagnetic (AFM) to paramagnetic transition of the material. Below 12 K, the spins are aligned in an ordered AFM arrangement, while above this temperature, thermal vibrations disrupts the magnetic ordering, giving rise to a disordered

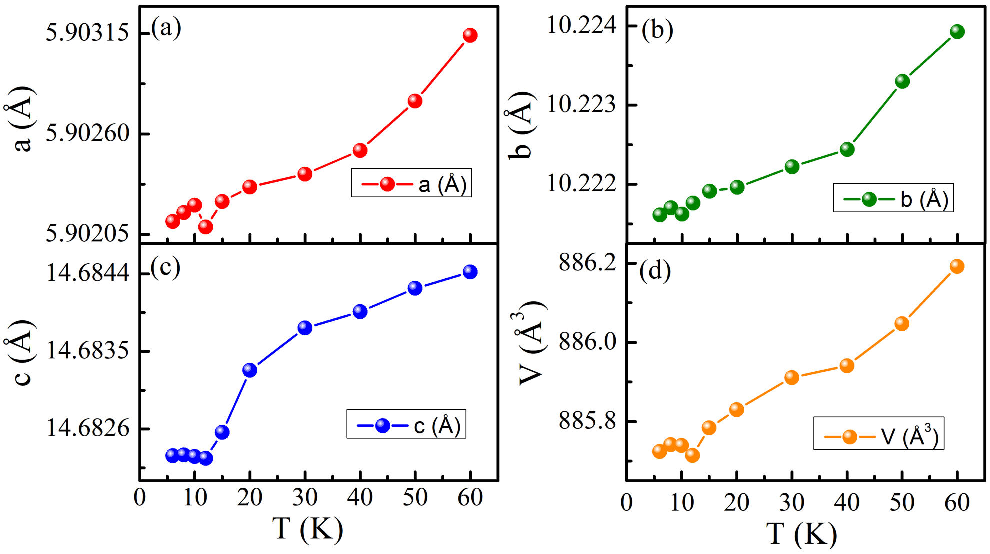

Figure 6.6: Ritveild Refinement data of $Ba_3SmRu_2O_9$ at (a) 300K and (b) 1.5 K

paramagnetic phase.

6.3.2 Powder Neutron Diffraction

We have performed the powder neutron diffraction on $Ba_3SmRu_2O_9$ system at 300 K and 1.5 K. shown in Fig. 6.7 to resolve the magnetic structure. The neutron diffraction profile measured at 300 K (above T_N) is well fitted with the reported space group P63/mmc, as shown in Fig. 6.8(a)). In this system there are two magnetic atoms Sm and Ru having wyckoff position 2a (0 0 0) and 8F (0.99189, 0.33132, 0.83671) respectively.The difference between the NPD data at 1.5 and 300 K (below and above T_N, respectively) reveals an increase of the intensity of two nuclear peaks [(002) and (110)] [see Fig. 6.7]. The additional intensities are observed only at a low angle pointing to their magnetic origin. We have observed the structural phase change in HRXRD data considering that we have fitted the low temperature(1.5 K) data using C2/c space group.All the magnetic reflections can be indexed using the k = (0 0 0) propagation vector. The Sm has same 2a whycoff position and Ru has the same 8f whycoff position. We did the irreducible representational analysis through SARAh program. The irreducible representations (I.R.) and basis vectors (B.V.) of the Ru and Sm spins for the C_2/c space group associated with the propagation vector are shown in Tables 6.1 and 6.2.

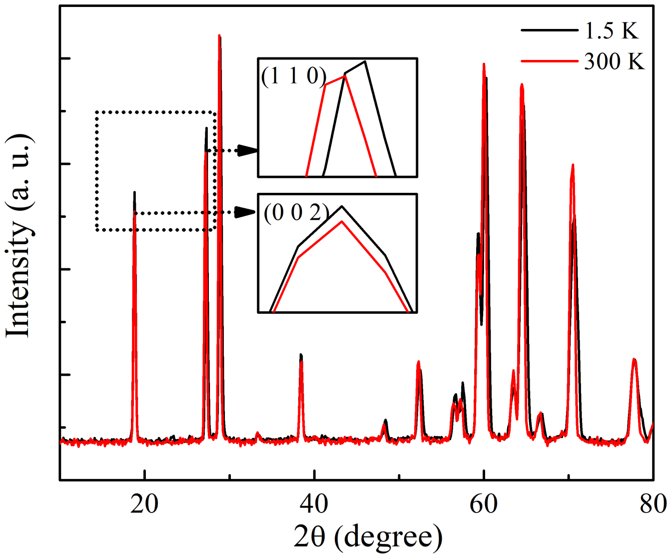

Figure 6.7: Comparison of Neutron data at 1.5K and 300 K

Table 6.1: Basis vectors (BV) for the space group C_2/c with propagation vector $\mathbf{K}$ = (0 0 0). Irreducible representations for the magnetic Sm site (0 0 0), obtained using the SARAH program.

IR	**BV**	**Atom**	**BV components**					
			$m \parallel a$	$m \parallel b$	$m \parallel c$	$im \parallel a$	$im \parallel b$	$im \parallel c$
Γ_1	ψ_1	1	2	0	0	0	0	0
		2	-2	0	0	0	0	0
	ψ_2	1	0	2	0	0	0	0
		2	0	2	0	0	0	0
	ψ_3	1	0	0	2	0	0	0
		2	0	0	-2	0	0	0
Γ_3	ψ_4	1	2	0	0	0	0	0
		2	2	0	0	0	0	0
	ψ_5	1	0	2	0	0	0	0
		2	0	-2	0	0	0	0
	ψ_6	1	0	0	2	0	0	0
		2	0	0	2	0	0	0

Table 6.2: Basis vector for the space group C2/c for **K** = (0 0 0). The irreducible representation for magnetic site Ru (0.33333, 0.66667, 0.16223), as obtained from SARAh program.

IR	**BV**	**Atom**	**BV components**					
			$m \parallel a$	$m \parallel b$	$m \parallel c$	$im \parallel a$	$im \parallel b$	$im \parallel c$
Γ_1	ψ_1	1	1	0	0	0	0	0
		2	-1	0	0	0	0	0
		3	1	0	0	0	0	0
		4	-1	0	0	0	0	0
	ψ_2	1	0	1	0	0	0	0
		2	0	1	0	0	0	0
		3	0	1	0	0	0	0
		4	0	1	0	0	0	0
	ψ_3	1	0	0	1	0	0	0
		2	0	0	-1	0	0	0
		3	0	0	1	0	0	0
		4	0	0	-1	0	0	0
Γ_2	ψ_4	1	1	0	0	0	0	0
		2	-1	0	0	0	0	0
		3	-1	0	0	0	0	0
		4	1	0	0	0	0	0
	ψ_5	1	0	1	0	0	0	0
		2	0	1	0	0	0	0
		3	0	-1	0	0	0	0
		4	0	-1	0	0	0	0
	ψ_6	1	0	0	1	0	0	0
		2	0	0	-1	0	0	0
		3	0	0	-1	0	0	0
		4	0	0	1	0	0	0

IR	**BV**	**Atom**	**BV components**					
			$m \parallel a$	$m \parallel b$	$m \parallel c$	$im \parallel a$	$im \parallel b$	$im \parallel c$
Γ_3	ψ_7	1	1	0	0	0	0	0
		2	1	0	0	0	0	0
		3	1	0	0	0	0	0
		4	1	0	0	0	0	0
	ψ_8	1	0	1	0	0	0	0
		2	0	-1	0	0	0	0
		3	0	1	0	0	0	0
		4	0	-1	0	0	0	0
	ψ_9	1	0	0	1	0	0	0
		2	0	0	1	0	0	0
		3	0	0	1	0	0	0
		4	0	0	1	0	0	0
Γ_4	ψ_{10}	1	1	0	0	0	0	0
		2	1	0	0	0	0	0
		3	-1	0	0	0	0	0
		4	-1	0	0	0	0	0
	ψ_{11}	1	0	1	0	0	0	0
		2	0	-1	0	0	0	0
		3	0	-1	0	0	0	0
		4	0	1	0	0	0	0
	ψ_{12}	1	0	0	1	0	0	0
		2	0	0	1	0	0	0
		3	0	0	-1	0	0	0
		4	0	0	-1	0	0	0

There are four irreducible representation for Ru and two irreducible representation For Sm.The magnetic representation is expressed as:

$$\Gamma_{\mathrm{mag}}(\mathrm{Ru}) = 3\Gamma_1^1 + 3\Gamma_2^1 + 3\Gamma_3^1 + 3\Gamma_4^1$$

$$\Gamma_{\text{mag}}(\text{Sm}) = 3\Gamma_1^1 + 0\Gamma_2^1 + 3\Gamma_3^1 + 0\Gamma_4^1$$

Since neutrons interact with the magnetic moment component perpendicular to the scattering angle (2θ), the significant difference in intensity of the (002) and (110) Bragg peaks at 1.5 K compared to 300 K suggests that the magnetic moment lies within either the *ab*-plane or the *c*-plane. Initially, we attempted to refine the magnetic structure by considering an ordered moment on the Ru sublattice only. However, the refinement did not converge, indicating that both Sm and Ru ions possess ordered magnetic moments at low temperatures (1.5 K). Therefore, we explored models based on the irreducible representations Γ_1 and Γ_3, which are common to both magnetic sites. Among all the models,The best refinements were obtained for two (i) the Γ_1 representation with basis vector Ψ_3, and (ii) a mixed representation given by $\Gamma_1\Psi_1 + \Gamma_3\Psi_5$. These correspond to an antiferromagnetic arrangement of Sm (↓↑↓) and Ru (↑↓) moments, either aligned along the *c*-axis or within the *a*-axis. For the magnetic structure along *c*-axis, the refined magnetic moments

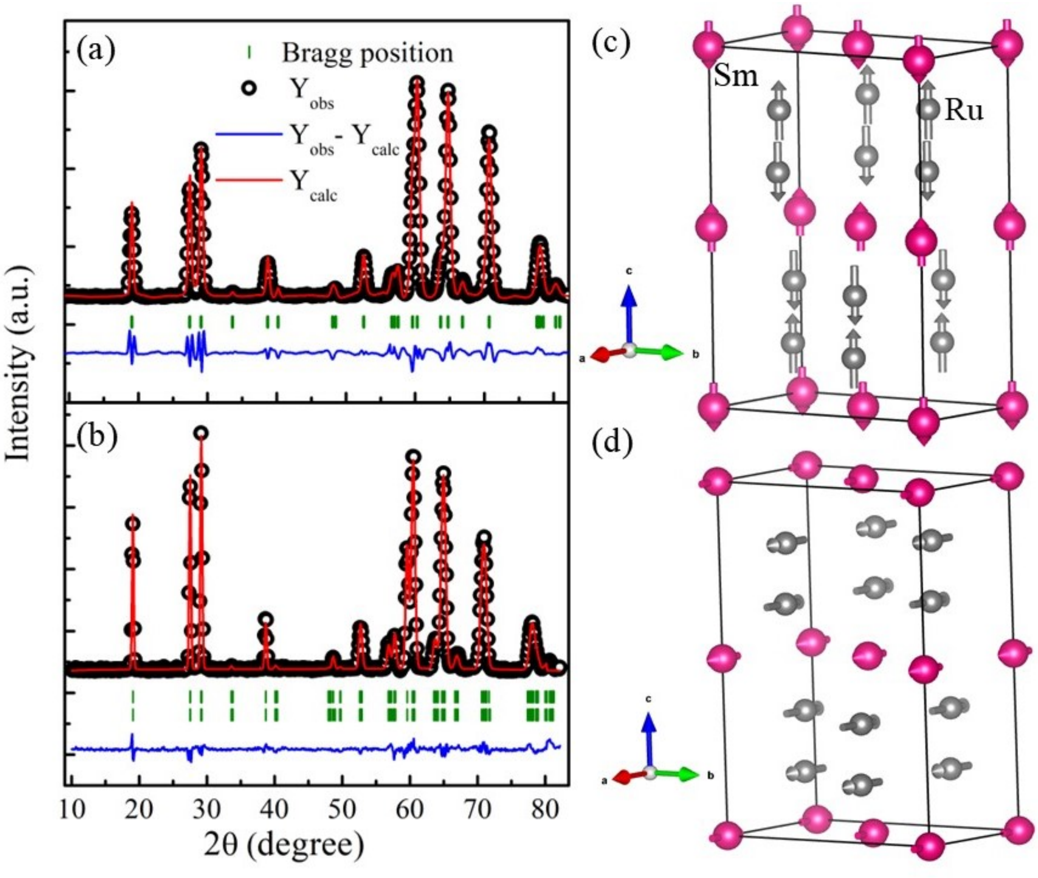

Figure 6.8: Ritveild Refinement data of $Ba_3SmRu_2O_9$ at (a) 300K and (b) 1.5 K (c) Magnetic Structure along *a*- axis, and (d) Magnetic Structure along *c*- axis, and

are approximately 0.41 μ_B for Ru and 0.3 μ_B for Sm while for other case, the moments are 0.57 μ_B for Ru and 0.41 μ_B for Sm along a-direction.The reitvield refinement of 1.5 K data is shown in Fig. 6.8 (b) and both the magnetic structures are shown in Fig 6.7(c-d). Within our experimental resolution both the structures are equally probable.

6.4 Conclusion

We have investigated the $Ba_3SmRu_2O_9$ compound through neutron diffraction and High resolution XRD. The HRXRD results suggest a temperature-driven structural transition from hexagonal $P6_3/mmc$ symmetry to monoclinic $P2/c$ and $C2/c$ phases below 90 K. The emergence of two inequivalent Ru sites in the intermediate $P2/c$ phase leads to asymmetric Ru_2O_9 dimers,in which one dimer exhibiting pronounced distortion that may suggest the possible involvement of charge ordering between inequivalent Ru sites or Jahn-Teller-type distortions associated with the RuO_6 octahedra, which could contribute to the observed symmetry lowering. However, the present structural analysis alone is not sufficient to confirm the charge ordering or Jahn-Teller effects. Further experimental investigations, such as resonant X-ray diffraction, X-ray absorption spectroscopy, bond-valence analysis, or complementary theoretical calculations, are required to clarify the microscopic origin of the dimer distortion and to conclusively identify the role of charge or orbital ordering, which is beyond the scope of this thesis. We have resolved the low-temperature magnetic structure of $Ba_3SmRu_2O_9$. Refinement of the neutron diffraction data yields two possible magnetic structures: one with the ordered magnetic moments aligned along the c-axis, and another with the moments oriented along the a-axis. Due to the relatively weak magnetic scattering intensity, it is not possible to distinguish between these two magnetic structures using the present neutron data. Both magnetic structures should therefore be considered equally possible structure. A similar ambiguity of magnetic structures has been reported in many other compound [115].

These results suggest that the phase evolution in $Ba_3SmRu_2O_9$ arises from a complex interplay of lattice dynamics, electronic instability, and magnetic interactions within a multi-well energy landscape.

Summary and Future Work

This thesis presents a comprehensive microscopic investigation Barium ruthenate dimers and trimers. We have used elastic and inelastic neutron scattering as the primary experimental tools. This work shows how crystal structure and local symmetry can modify the magnetic exchange interactions and give rise to unconventional magnetic ground states. In the $Ba_5Ru_3O_{12}$ compound, inelastic neutron scattering reveals short-range magnetic correlations that persist far above the long range ordering temperature, highlighting the intrinsic nature of trimer-based magnetism. Our combined INS and SpinW simulation result suggest that the competing exchange interactions and octahedral distortions stabilize a non-collinear magnetic structure in which each Ru ion hosts a distinct magnetic ground state from other barium ruthenate trimers.The INS and MLFFs study further suggest the possibility of magnon phonon coupling in this compound. The thesis further establishes the importance of cooperative $4d$-$4f$ magnetism in the 6H-perovskite $Ba_3RRu_2O_9$ family. In $Ba_3HoRu_2O_9$, this work reports the first experimental demonstration of spin-driven ferroelectricity in $4d$-$4f$ coupled system originating from inverse Dzyaloshinskii-Moriya interactions that explicitly involve both transition metal oxide and rare earth magnetic moments. These results provide an unambiguous evidence that cooperative Ru-Ho interactions can generate spin-driven ferroelectric polarization which establish $Ba_3HoRu_2O_9$ as a rare example. Our combined investigation of inelastic neutron scattering, Raman spectroscopy, and machine-learned force-field calculations reveals the presence of CEF-phonon coupling in this compound that highlight the strong interplay between spin, lattice, and electronic degrees of freedom . On the other hand, $Ba_3TbRu_2O_9$ exhibits a distinctly different magnetic ground state. In this compound, Tb stabilizes a tetravalent electronic configuration, and the experimentally observed magnetic moments indicate nearly full ordering of the Ru moment, while generally reduced Ru moment is observed across the $Ba_3RRu_2O_9$ family. Clear evidence of cooperative Ru-Tb magnetic ordering is observed, demonstrating how rare-earth valence and electronic character can fundamentally alter

$4d$-$4f$ exchange interactions. $Ba_3SmRu_2O_9$ represents an intermediate and distinct regime within the $Ba_3RRu_2O_9$ family. A structural transition at higher temperatures is observed for this compound that leads to symmetry lowering and the formation of inequivalent Ru_2O_9 dimers. Our neutron diffraction suggest that magnetic moment oriented either along the crystallographic c axis or a axis. However , due to low magnetic moment of Sm and weak scattering cross section we cannot pin point the exact magnetic structure. In Table 7.1 we have shown the magnetic moments obtained from Neutron difftraction Results for different R ions.

Table 6.3: Comparison of magnetic moments of Ru (m_{Ru}) and rare-earth ions (m_R) in $Ba_3RRu_2O_9$ (R = Ho, Tb, Sm).

Compound	**k-vector**	m_{Ru}	m_R
$Ba_3HoRu_2O_9$	(0.25 0.25 0)	0.995	4.920
	(0.5 0 0)	0.574	5.856
$Ba_3TbRu_2O_9$	(0 0 0)	1.96050	6.18782
$Ba_3SmRu_2O_9$	(0 0 0)	0.41 (c-axis) / 0.57 (a-axis)	0.3 (c-axis) / 0.41 (a-axis)

The comparative analysis of various member of this family, reveals that rare-earth elements play a decisive role in deciding the magnetic ground state and collective behavior in these systems. The results of all the experiments establish barium ruthenates as a versatile platform for exploring the interplay between structure, magnetism, and lattice dynamics, and provide a foundation for future studies combining neutron spectroscopy with data-driven theoretical approaches.

While this thesis addresses several important questions, it also highlights a number of promising directions for future research.

1. We discussed previously that the magnetic ground states of ruthenate dimers and trimers are highly sensitive to small structural changes. Further high-pressure study would be extremely useful for further understanding these systems. In Ba_3HoRu_2O9 we have show that pressure can enhance magnetic ordering temperatures and suppress competing phases. Extending such experiments to other ruthenate compound may uncover pressure-induced phase transitions and new magnetic states.

2. Even small changes in the local structure or chemical composition such as partial substitution at the transition-metal or non magnetic site can strongly modify

magnetic exchange interactions and the electronic bandwidth. The Ru posses an octahedral position, It is theoretically predicted the large d orbital can enhance MD coupling and multiferrocity [12]. Our study on $Ba_3HoRu_2O_9$ open up the possibility of spin driven ferroelectricity in 4d based system. Our experimental study further boost the research to replace 3d counterpart (in octahedral position) by Ru in many well known multiferroic systems. Hence, this work provide valuable insight into the tuning of magnetic interactions, multiferroic behavior, and metal-insulator transitions within closely related crystal structures.

3. The application of machine learning to the study of correlated magnetic materials is still at an early stage. Future work could focus on the development of machine-learning models capable of fast and accurate prediction of phonon and magnon spectra with near first-principles accuracy, while achieving close quantitative agreement with experimentally measured data. Such approaches would significantly accelerate the interpretation of spectroscopic measurements and enable efficient exploration of complex magnetic and lattice dynamics in strongly correlated systems.

List of Publications

Publication in Peer-Reviewed journals

(1) E. Kushwaha, G. Roy, M. Kumar, A. M. dos Santos, S. Ghosh, D. T. Adroja, V. Caignaert, O. Perez, A. Pautrat, and T. Basu*. Origin of spin-driven ferroelectricity and effect of external pressure on the complex magnetism of the 6H perovskite $Ba_3HoRu_2O_9$. *Physical Review B* **109**, 224418 (2024).

(2) E. Kushwaha, G. Roy, A. M. dos Santos, M. Kumar, S. Ghosh, T. Heitmann, and T. Basu*. Unconventional s-orbital state of Tb and cooperative Ru($4d$)–Tb($4f$) spin ordering in the strongly correlated $4d$–$4f$ system $Ba_3TbRu_2O_9$. *Journal of Materials Chemistry C* **13**, 15384–15389 (2025).

(3) E. Kushwaha, S. Ghosh, J. Sannigrahi, G. Roy, M. Kumar, S. Cottrell, M. B. Stone *et al.* Interplay between trimer structure and magnetic ground state in $Ba_5Ru_3O_{12}$ probed by neutron and μSR techniques. *Physical Review B* **112**, 094410 (2025).

Manuscript under review/submitted

(4) E. Kushwaha, S. Ghosh, G. Roy, M. Kumar, M. D. Le, J. Sannigrahi, S. D. Kaushik, D. T. Adroja, and T. Basu*. Understanding exchange interactions and CEF-phonon coupling in multiferroic $Ba_3HoRu_2O_9$ probed by inelastic neutron scattering and machine-learning methods. **Manuscript under review.**

(5) E. Kushwaha *et al.* Investigation of structural transitions in the $4d$–$4f$ system $Ba_3SmRu_2O_9$. **Manuscript submitted.**

Bibliography

[1] L. D. Landau, "The theory of a fermi liquid," *Soviet Physics Jetp-Ussr*, vol. 3, no. 6, pp. 920–925, 1957.

[2] M. Imada, A. Fujimori, and Y. Tokura, "Metal-insulator transitions," *Reviews of modern physics*, vol. 70, no. 4, p. 1039, 1998.

[3] A. Georges, L. d. Medici, and J. Mravlje, "Strong correlations from hund's coupling," *Annu. Rev. Condens. Matter Phys.*, vol. 4, no. 1, pp. 137–178, 2013.

[4] N. F. Mott, "The basis of the electron theory of metals, with special reference to the transition metals," *Proceedings of the Physical Society. Section A*, vol. 62, no. 7, p. 416, 1949.

[5] N. F. Mott, "Metal-insulator transition," *Reviews of Modern Physics*, vol. 40, no. 4, p. 677, 1968.

[6] J. Hubbard, "Electron correlations in narrow energy bands," *Proceedings of the Royal Society of London. Series A. Mathematical and Physical Sciences*, vol. 276, no. 1365, pp. 238–257, 1963.

[7] J. Kondo, "Resistance minimum in dilute magnetic alloys," *Progress of theoretical physics*, vol. 32, no. 1, pp. 37–49, 1964.

[8] A. C. Hewson, *The Kondo problem to heavy fermions.* No. 2, Cambridge university press, 1997.

[9] P. Coleman, "Heavy fermions: Electrons at the edge of magnetism," *Handbook of Magnetism and Advanced Magnetic Materials*, 2007.

[10] J. G. Bednorz and K. A. Müller, “Possible high t c superconductivity in the ba- la- cu- o system,” *Zeitschrift für Physik B Condensed Matter*, vol. 64, no. 2, pp. 189–193, 1986.

[11] T. Kimura, T. Goto, H. Shintani, K. Ishizaka, T.-h. Arima, and Y. Tokura, “Magnetic control of ferroelectric polarization,” *nature*, vol. 426, no. 6962, pp. 55–58, 2003.

[12] N. A. Spaldin and M. Fiebig, “The renaissance of magnetoelectric multiferroics,” *Physical Review B*, vol. 78, no. 10, p. 104416, 2008.

[13] Y. Tokura, S. Seki, and N. Nagaosa, “Multiferroics of spin origin,” *Reports on Progress in Physics*, vol. 77, no. 7, p. 076501, 2014.

[14] Y. Maeno, H. Hashimoto, K. Yoshida, S. Nishizaki, T. Fujita, J. Bednorz, and F. Lichtenberg, “Superconductivity in a layered perovskite without copper,” *nature*, vol. 372, no. 6506, pp. 532–534, 1994.

[15] Y. Maeno, A. Ikeda, and G. Mattoni, “Thirty years of puzzling superconductivity in sr2ruo4,” *Nature Physics*, vol. 20, no. 11, pp. 1712–1718, 2024.

[16] A. B. Christian, *Magnetic and Thermal Properties of Low-Dimensional Single-Crystalline Transition-Metal Antimonates and Tantalates.* Montana State University, 2017.

[17] J. B. Goodenough, “Magnetism and the chemical bond,” *(No Title)*, 1963.

[18] D. I. Khomskii, *Transition metal compounds.* Cambridge University Press, 2014.

[19] S. V. Streltsov and D. I. Khomskii, “Orbital physics in transition metal compounds: new trends,” *Physics-Uspekhi*, vol. 60, no. 11, pp. 1121–1140, 2017.

[20] P. W. Anderson, “Antiferromagnetism. theory of superexchange interaction,” *Physical Review*, vol. 79, no. 2, p. 350, 1950.

[21] N. Mott, *Metal-insulator transitions.* CRC Press, 2004.

[22] S. Mishra, M. Gupta, R. Mittal, A. I. Kolesnikov, and S. Chaplot, “Spin-phonon coupling and high-pressure phase transitions of r mn o 3 (r= ca and pr): An inelastic neutron scattering and first-principles study,” *Physical Review B*, vol. 93, no. 21, p. 214306, 2016.

[23] S. Petit, F. Moussa, M. Hennion, S. Pailhès, L. Pinsard-Gaudart, and A. Ivanov, "Spin phonon coupling in hexagonal multiferroic y mno 3," *Physical review letters*, vol. 99, no. 26, p. 266604, 2007.

[24] H. Lewtas, T. Lancaster, P. Baker, S. Blundell, D. Prabhakaran, and F. Pratt, "Local magnetism and magnetoelectric effect in homno 3 studied with muon-spin relaxation," *Physical Review B—Condensed Matter and Materials Physics*, vol. 81, no. 1, p. 014402, 2010.

[25] G. R. Blake, L. C. Chapon, P. G. Radaelli, S. Park, N. Hur, S.-W. Cheong, and J. Rodríguez-Carvajal, "Spin structure and magnetic frustration in multiferroic rmn2o5 (r = tb, ho, dy)," *Physical Review B*, vol. 71, no. 21, p. 214402, 2005.

[26] A. M. Kadomtseva, S. S. Krotov, Y. F. Popov, and G. P. Vorob'ev, "Features of the magnetoelectric behavior of the family of multiferroics rmn2o5 at high magnetic fields," *Low Temperature Physics*, vol. 32, pp. 709–714, 2006.

[27] V. Balédent, S. Chattopadhyay, P. Fertey, M. B. Lepetit, M. Greenblatt, B. Wanklyn, F. O. Saouma, J. I. Jang, and P. Foury-Leylekian, "Evidence for room temperature electric polarization in rmn2o5 multiferroics," *Physical Review Letters*, vol. 114, no. 11, p. 117601, 2015.

[28] N. Lee, C. Vecchini, Y. J. Choi, L. C. Chapon, A. Bombardi, P. G. Radaelli, and S.-W. Cheong, "Giant tunability of ferroelectric polarization in gdmn2o5," *Physical Review Letters*, vol. 110, no. 13, p. 137203, 2013.

[29] L. H. Yin, D. H. Jang, C. B. Park, K. W. Shin, and K. H. Kim, "Pressure-induced ferroelectricity and enhancement of mn–mn exchange striction in gdmn2o5," *Journal of Applied Physics*, vol. 119, p. 104101, 2016.

[30] W. Peng *et al.*, "Toward pressure-induced multiferroicity in prmn2o5," *Physical Review B*, vol. 96, no. 5, p. 054418, 2017.

[31] L. C. Chapon, G. R. Blake, M. J. Gutmann, S. Park, N. Hur, P. G. Radaelli, and S.-W. Cheong, "Structural anomalies and multiferroic behavior in magnetically frustrated tbmn2o5," *Physical Review Letters*, vol. 93, no. 17, p. 177402, 2004.

[32] Y. J. Choi, H. T. Yi, S. Lee, Q. Huang, V. Kiryukhin, and S.-W. Cheong, "Ferroelectricity in an ising chain magnet," *Physical Review Letters*, vol. 100, no. 4, p. 047601, 2008.

[33] A. Maignan *et al.*, "Fe2co2nb2o9: A magnetoelectric honeycomb antiferromagnet," *Journal of Materials Chemistry C*, vol. 9, pp. 14236–14243, 2021.

[34] K. Maiti and R. S. Singh, "Evidence against strong correlation in 4d transition-metal oxides caruo 3 and srruo 3," *Physical Review B: Condensed Matter and Materials Physics*, vol. 71, no. 16, pp. 161102_1–161102_4, 2005.

[35] B. Kim, H. Jin, S. Moon, J.-Y. Kim, B.-G. Park, C. Leem, J. Yu, T. Noh, C. Kim, S.-J. Oh, *et al.*, "Novel j eff= 1/2 mott state induced by relativistic spin-orbit coupling in sr 2 iro 4," *Physical review letters*, vol. 101, no. 7, p. 076402, 2008.

[36] M. Braden, G. André, S. Nakatsuji, and Y. Maeno, "Crystal and magnetic structure of ca 2 ruo 4: Magnetoelastic coupling and the metal-insulator transition," *Physical Review B*, vol. 58, no. 2, p. 847, 1998.

[37] S. Nakatsuji and Y. Maeno, "Quasi-two-dimensional mott transition system ca 2- x sr x ruo 4," *Physical Review Letters*, vol. 84, no. 12, p. 2666, 2000.

[38] C. R. Wiebe, J. S. Gardner, S. J. Kim, G. M. Luke, A. S. Wills, B. D. Gaulin, I. Swainson, Y. Qiu, and C. Y. Jones, "Magnetic ordering in the spin-ice candidate ho2ru2o7," *Physical Review Letters*, vol. 93, no. 7, p. 076403, 2004.

[39] J. S. Gardner, A. L. Cornelius, L. J. Chang, M. Prager, T. Brückel, and G. Ehlers, "Spin dynamics in ho2ru2o7," *Journal of Physics: Condensed Matter*, vol. 17, no. 44, pp. 7089–7102, 2005.

[40] F. Museur, J. Robert, F. Morineau, V. Simonet, E. Pachoud, A. Hadj-Azzem, C. Colin, P. Manuel, J. R. Stewart, P. C. W. Holdsworth, and E. Lhotel, "Ferromagnetic fragmented ground state in the pyrochlore ho2ru2o7," *arXiv*, p. arXiv:2411.10078, 2024.

[41] M. Rams, A. Zarzycki, A. Pikul, and K. Tomala, "Magnetic order and crystal field in dy2ru2o7 and yb2ru2o7," *Journal of Magnetism and Magnetic Materials*, vol. 323, no. 11, pp. 1490–1494, 2011.

[42] L. J. Chang, M. Prager, J. Persson, J. Walter, E. Jansen, Y. Y. Chen, and J. S. Gardner, "Magnetic order in the double pyrochlore tb2ru2o7," *Journal of Physics: Condensed Matter*, vol. 22, no. 7, p. 076003, 2010.

[43] J. S. Lee, T. W. Noh, J. S. Bae, I. S. Yang, T. Takeda, and R. Kanno, “Strong spin–phonon coupling in the geometrically frustrated pyrochlore y2ru2o7,” *Physical Review B*, vol. 69, no. 21, p. 214428, 2004.

[44] N. Taira, M. Wakeshima, and Y. Hinatsu, “Magnetic susceptibility and specific heat studies on heavy rare earth ruthenate pyrochlores r 2 ru 2 o 7 (r= gd–yb),” *Journal of Materials Chemistry*, vol. 12, no. 5, pp. 1475–1479, 2002.

[45] Y. Doi, Y. Hinatsu, A. Nakamura, Y. Ishii, and Y. Morii, “Magnetic and neutron diffraction studies on double perovskites a 2 lnruo 6 (a= sr, ba; ln= tm, yb),” *Journal of Materials Chemistry*, vol. 13, no. 7, pp. 1758–1763, 2003.

[46] Y. Hinatsu and Y. Doi, “Structures and magnetic properties of double perovskites a2lnmo6 and 6h-perovskites ba3lnru2o9 (a= sr, ba; ln= y, lanthanides; m= nb, ta, ru),” *Bulletin of the Chemical Society of Japan*, vol. 76, no. 6, pp. 1093–1113, 2003.

[47] P. Mohanty, S. Marik, D. Singh, and R. P. Singh, “Exchange bias properties in sr2lnruo6 (ln= dy, ho and er),” *Materials Research Express*, vol. 4, no. 12, p. 126103, 2017.

[48] D. T. Adroja, S. Sharma, C. Ritter, A. D. Hillier, D. Le, C. V. Tomy, R. Singh, R. I. Smith, M. Koza, A. Sundaresan, and S. Langridge, “Muon spin rotation and neutron scattering investigations of the b-site ordered double perovskite sr2dyruo6,” *Physical Review B*, vol. 101, no. 9, p. 094413, 2020.

[49] S. Sharma, D. T. Adroja, C. Ritter, D. Khalyavin, P. Manuel, G. B. Stenning, A. Sundaresan, A. D. Hillier, P. P. Deen, D. I. Khomskii, and S. Langridge, “Magnetic ground state of the ordered double-perovskite sr2ybruo6: Two magnetic transitions,” *Physical Review B*, vol. 102, no. 13, p. 134412, 2020.

[50] G. Roy, E. Kushwaha, M. Kumar, S. Ghosh, F. Orlandi, D. Le, M. B. Stone, J. Sannigrahi, D. T. Adroja, and T. Basu, “Quasiparticle dynamics in the 4d–4f ising-like double perovskite ba2dyruo6 probed by neutron scattering and machine-learning framework,” *arXiv*, p. arXiv:2512.24778, 2025.

[51] Y. Doi, Y. Hinatsu, K.-i. Oikawa, Y. Shimojo, and Y. Morii, “Magnetic and neutron diffraction study on the ordered perovskite sr2horuo6,” *Journal of Materials Chemistry*, vol. 10, no. 3, pp. 797–800, 2000.

[52] E. Granado, J. W. Lynn, R. F. Jardim, and M. S. Torikachvili, “Two-dimensional magnetic correlations and partial long-range order¡? format?¿ in geometrically frustrated sr 2 yruo 6,” *Physical review letters*, vol. 110, no. 1, p. 017202, 2013.

[53] J. Rijssenbeek, R. Jin, Y. Zadorozhny, Y. Liu, B. Batlogg, and R. Cava, “Electrical and magnetic properties of the two crystallographic forms of baruo 3,” *Physical Review B*, vol. 59, no. 7, p. 4561, 1999.

[54] J. Wang, X.-L. Xu, and X. Li, “Recent progress of multiferroicity and magnetoelectric effects in abx3-type perovskite metal–organic frameworks,” *Advanced Materials Interfaces*, vol. 10, no. 25, p. 2300123, 2023.

[55] C. Felser and R. Cava, “Electronic structure of two crystallographic forms of baruo 3,” *Physical Review B*, vol. 61, no. 15, p. 10005, 2000.

[56] Y. Doi and Y. Hinatsu, “Magnetic and calorimetric studies on ba3lnru2o9 (ln = gd, ho–yb) with 6h-perovskite structure,” *Journal of Materials Chemistry*, vol. 12, no. 6, pp. 1792–1798, 2002.

[57] Y. Doi, M. Wakeshima, Y. Hinatsu, A. Tobo, K. Ohoyama, and Y. Yamaguchi, “Crystal structures and magnetic properties of the 6h-perovskites ba3lnru2o9 (ln= ce, pr and tb),” *Journal of Materials Chemistry*, vol. 11, no. 12, pp. 3135–3140, 2001.

[58] M. S. Senn, S. A. J. Kimber, A. M. Arevalo Lopez, A. H. Hill, and J. P. Attfield, “Spin orders and lattice distortions of geometrically frustrated 6h-perovskites ba3b’ru2o9 (b’ = la3+, nd3+, and y3+),” *Physical Review B*, vol. 87, no. 13, p. 134402, 2013.

[59] D. Ziat, A. A. Aczel, R. Sinclair, Q. Chen, H. Zhou, T. J. Williams, M. B. Stone, A. Verrier, and J. Quilliam, “Frustrated spin-1 2 molecular magnetism in the mixed-valence antiferromagnets ba 3 m ru 2 o 9 (m= in, y, lu),” *Physical Review B*, vol. 95, no. 18, p. 184424, 2017.

[60] Q. Chen, A. Verrier, D. Ziat, A. J. Clune, R. Rouane, X. Bazier-Matte, G. Wang, S. Calder, K. M. Taddei, C. D. Cruz, and A. I. Kolesnikov, “Realization of the orbital-selective mott state at the molecular level in ba3laru2o9,” *Physical Review Materials*, vol. 4, no. 6, p. 064409, 2020.

[61] Q. Chen, S. Fan, K. M. Taddei, M. B. Stone, A. I. Kolesnikov, J. Cheng, J. L. Musfeldt, H. Zhou, and A. A. Aczel, "Large positive zero-field splitting in the cluster magnet ba3ceru2o9," *Journal of the American Chemical Society*, vol. 141, no. 25, pp. 9928–9936, 2019.

[62] T. Basu, V. Caignaert, F. Damay, T. W. Heitmann, B. Raveau, and X. Ke, "Cooperative ru(4d)–ho(4f) magnetic ordering and phase coexistence in the 6h-perovskite multiferroic ba3horu2o9," *Physical Review B*, vol. 102, no. 2, p. 020409, 2020.

[63] J. Rodríguez-Carvajal, "Recent advances in magnetic structure determination by neutron powder diffraction," *Physica B: Condensed Matter*, vol. 192, no. 1-2, pp. 55–69, 1993.

[64] A. Wills, "A new protocol for the determination of magnetic structures using simulated annealing and representational analysis (sarah)," *Physica B: Condensed Matter*, vol. 276, pp. 680–681, 2000.

[65] O. Arnold, J.-C. Bilheux, J. Borreguero, A. Buts, S. I. Campbell, L. Chapon, M. Doucet, N. Draper, R. F. Leal, M. Gigg, *et al.*, "Mantid—data analysis and visualization package for neutron scattering and μ sr experiments," *Nuclear instruments and methods in physics research section a: accelerators, spectrometers, detectors and associated equipment*, vol. 764, pp. 156–166, 2014.

[66] R. T. Azuah, L. R. Kneller, Y. Qiu, P. L. Tregenna-Piggott, C. M. Brown, J. R. Copley, and R. M. Dimeo, "Dave: A comprehensive software suite for the reduction, visualization, and analysis of low energy neutron spectroscopic data," *Journal of Research of the National Institute of Standards and Technology*, vol. 114, no. 6, pp. 341–358, 2009.

[67] S. Toth and B. Lake, "Linear spin wave theory for single-q incommensurate magnetic structures," *Journal of Physics: Condensed Matter*, vol. 27, no. 16, p. 166002, 2015.

[68] H. Yang, C. Hu, Y. Zhou, X. Liu, Y. Shi, J. Li, G. Li, Z. Chen, S. Chen, C. Zeni, and M. Horton, "Mattersim: A deep learning atomistic model across elements, temperatures and pressures," *arXiv*, p. arXiv:2405.04967, 2024.

[69] Y. Cheng, G. Wu, D. M. Pajerowski, M. B. Stone, A. T. Savici, M. Li, and A. J. Ramirez-Cuesta, "Direct prediction of inelastic neutron scattering spectra from

the crystal structure," *Machine Learning: Science and Technology*, vol. 4, no. 1, p. 015010, 2023.

[70] G. L. Squires, *Introduction to the theory of thermal neutron scattering.* Courier Corporation, 1996.

[71] R. Dronskowski, T. Brückel, H. Kohlmann, M. Avdeev, A. Houben, M. Meven, M. Hofmann, T. Kamiyama, M. Zobel, W. Schweika, *et al.*, "Neutron diffraction: a primer," *Zeitschrift für Kristallographie-Crystalline Materials*, vol. 239, no. 5-6, pp. 139–166, 2024.

[72] T. Egami and S. J. Billinge, *Underneath the Bragg peaks: structural analysis of complex materials*, vol. 16. Newnes, 2012.

[73] D. L. Price and F. Fernandez-Alonso, "An introduction to neutron scattering," in *Experimental Methods in the Physical Sciences*, vol. 44, pp. 1–136, Elsevier, 2013.

[74] R. Scherm, "Fundamentals of neutron scattering by condensed matter," *Annales de Physique*, vol. 7, no. 5, pp. 349–370, 1972. Lecture notes, Institut Laue–Langevin, Grenoble.

[75] Y. Klein, G. Rousse, F. Damay, F. Porcher, G. André, and I. Terasaki, "Antiferromagnetic order and consequences on the transport properties of ba4ru3o10," *Physical Review B*, vol. 84, no. 5, p. 054439, 2011.

[76] J. Sannigrahi, A. Paul, A. Banerjee, D. Khalyavin, A. D. Hillier, K. Yokoyama, A. K. Bera, M. R. Lees, I. Dasgupta, S. Majumdar, and D. T. Adroja, "Orbital effects and affleck–haldane-type spin dimerization in ba4ru3o10," *Physical Review B*, vol. 103, no. 14, p. 144431, 2021.

[77] T. Basu, F. Wei, Q. Zhang, Y. Fang, and X. Ke, "Complex magnetic structure in ba 5 ru 3 o 12 with isolated ru 3 o 12 trimer," *Physical Review Materials*, vol. 4, no. 11, p. 114401, 2020.

[78] L. T. Nguyen, T. Halloran, W. Xie, T. Kong, C. L. Broholm, and R. J. Cava, "Geometrically frustrated trimer-based mott insulator," *Physical Review Materials*, vol. 2, no. 5, p. 054414, 2018.

[79] P. Khalifah, R. Osborn, Q. Huang, H. Zandbergen, R. Jin, Y. Liu, D. Mandrus, and R. Cava, "Orbital ordering transition in la4ru2o10," *Science*, vol. 297, no. 5590, pp. 2237–2240, 2002.

[80] R. J. Cava, "Schizophrenic electrons in ruthenium-based oxides," *Dalton Transactions*, vol. 2004, no. 19, pp. 2979–2987, 2004.

[81] B. Rahaman, S. Kar, A. Vasiliev, and T. Saha-Dasgupta, "Interplay of alternation and further neighbor interaction in s= 1 2 spin chains: A case study of cs 2 cual 4 o 8," *Physical Review B*, vol. 98, no. 14, p. 144412, 2018.

[82] K. Bernot, J. Luzon, A. Caneschi, D. Gatteschi, R. Sessoli, L. Bogani, A. Vindigni, A. Rettori, and M. Pini, "Spin canting in a dy-based single-chain magnet with dominant next-nearest-neighbor antiferromagnetic interactions," *Physical Review B—Condensed Matter and Materials Physics*, vol. 79, no. 13, p. 134419, 2009.

[83] S. Keshavarz, J. Schött, A. J. Millis, and Y. O. Kvashnin, "Electronic structure, magnetism, and exchange integrals in transition-metal oxides: Role of the spin polarization of the functional in dft+ u calculations," *Physical Review B*, vol. 97, no. 18, p. 184404, 2018.

[84] J. Sannigrahi, S. Bhowal, S. Giri, S. Majumdar, and I. Dasgupta, "Exchange-striction induced giant ferroelectric polarization in copper-based multiferroic material α-cu 2 v 2 o 7," *Physical Review B*, vol. 91, no. 22, p. 220407, 2015.

[85] E. McCabe, C. Stock, E. Rodriguez, A. Wills, J. Taylor, and J. Evans, "Weak spin interactions in mott insulating la 2 o 2 fe 2 ose 2," *Physical Review B*, vol. 89, no. 10, p. 100402, 2014.

[86] A. Podlesnyak, V. Pomjakushin, E. Pomjakushina, K. Conder, and A. Furrer, "Magnetic excitations in the spin-trimer compounds ca 3 cu 3- x ni x (po 4) 4 (x= 0, 1, 2)," *Physical Review B—Condensed Matter and Materials Physics*, vol. 76, no. 6, p. 064420, 2007.

[87] M. Hase, M. Matsuda, K. Kaneko, N. Metoki, K. Kakurai, T. Yang, R. Cong, J. Lin, K. Ozawa, and H. Kitazawa, "Magnetic excitations in the spin-5 2 antiferromagnetic trimer substance srmn 3 p 4 o 14," *Physical Review B—Condensed Matter and Materials Physics*, vol. 84, no. 21, p. 214402, 2011.

[88] X. Chen, D. Bansal, S. Sullivan, D. L. Abernathy, A. A. Aczel, J. Zhou, O. Delaire, and L. Shi, "Weak coupling of pseudoacoustic phonons and magnon dynamics in the incommensurate spin-ladder compound s r 14 c u 24 o 41," *Physical Review B*, vol. 94, no. 13, p. 134309, 2016.

[89] J. Sannigrahi, M. S. Khan, M. Numan, M. Das, A. Banerjee, M. D. Le, G. Cibin, D. Adroja, and S. Majumdar, "Role of crystal and magnetic structures in the magnetoelectric coupling in camn 7 o 12," *Physical Review B*, vol. 109, no. 5, p. 054417, 2024.

[90] E. Prince, *International Tables for Crystallography, Volume C: Mathematical, physical and chemical tables.* Springer Science & Business Media, 2004.

[91] T. Basu, A. Pautrat, V. Hardy, A. Loidl, and S. Krohns, "Magnetodielectric coupling in a ru-based 6h-perovskite ba3ndru2o9," *Applied Physics Letters*, vol. 113, no. 4, p. 042902, 2018.

[92] T. Basu, V. Caignaert, S. Ghara, X. Ke, A. Pautrat, S. Krohns, A. Loidl, and B. Raveau, "Enhancement of magnetodielectric coupling in 6h-perovskites ba3rru2o9 for heavier rare-earth cations (r = ho, tb)," *Physical Review Materials*, vol. 3, no. 11, p. 114401, 2019.

[93] W. Müller, M. Avdeev, Q. Zhou, A. J. Studer, B. J. Kennedy, G. J. Kearley, and C. D. Ling, "Spin-gap opening accompanied by a strong magnetoelastic response in the s = 1 magnetic dimer system ba3biru2o9," *Physical Review B*, vol. 84, no. 22, p. 220406, 2011.

[94] M. D. Le, T. Guidi, R. Bewley, J. R. Stewart, E. M. Schooneveld, D. Raspino, D. E. Pooley, J. Boxall, K. F. Gascoyne, N. J. Rhodes, and S. R. Moorby, "Upgrade of the mari spectrometer at isis," *Nuclear Instruments and Methods in Physics Research Section A*, vol. 1056, p. 168646, 2023.

[95] T. Basu, P. L. Paulose, K. K. Iyer, K. Singh, N. Mohapatra, S. Chowki, B. Gonde, and E. V. Sampathkumaran, "A reentrant phenomenon in magnetic and dielectric properties of dy2banio5 and an intriguing influence of external magnetic field," *Journal of Physics: Condensed Matter*, vol. 26, no. 17, p. 172202, 2014.

[96] Y. Tian, S. Shen, J. Cong, L. Yan, S. Wang, and Y. Sun, “Observation of resonant quantum magnetoelectric effect in a multiferroic metal–organic framework,” *Journal of the American Chemical Society*, vol. 138, pp. 782–785, 2016.

[97] T. Basu *et al.*, “Magnetodielectric coupling in a non-perovskite metal–organic framework,” *Materials Horizons*, vol. 4, pp. 1178–1185, 2017.

[98] T. Basu, A. Jesche, B. Bredenkötter, M. Grzywa, D. Denysenko, D. Volkmer, A. Loidl, and S. Krohns, “Magnetodielectric coupling in a non-perovskite metal–organic framework,” *Materials Horizons*, vol. 4, no. 6, pp. 1178–1184, 2017.

[99] K. Sun, Y. Zhu, S. Wu, J. Xia, P. Zhou, Q. Zhao, C. Cao, and H.-F. Li, “Temperature-dependent structure of an intermetallic erpd2si2 single crystal: a combined synchrotron and in-house x-ray diffraction study,” *Powder Diffraction*, vol. 37, no. 2, pp. 91–97, 2022.

[100] S. Mathew, A. R. Abraham, S. Chintalapati, S. Sarkar, B. Joseph, and T. Venkatesan, “Temperature dependent structural evolution of wse2: A synchrotron x-ray diffraction study,” *Condensed Matter*, vol. 5, no. 4, p. 76, 2020.

[101] M. Numan, G. Das, M. S. Khan, G. Manna, A. Banerjee, S. Giri, G. Aquilanti, and S. Majumdar, “Evidence of exchange striction and charge disproportionation in the magnetoelectric material ni 3 teo 6,” *Physical Review B*, vol. 106, no. 21, p. 214437, 2022.

[102] T. Basu, V. R. Kishore, S. Gohil, K. Singh, N. Mohapatra, S. Bhattacharjee, B. Gonde, N. Lalla, P. Mahadevan, S. Ghosh, *et al.*, “Displacive-type ferroelectricity from magnetic correlations within spin-chain,” *Scientific Reports*, vol. 4, no. 1, p. 5636, 2014.

[103] K. I. Kugel, D. I. Khomskii, A. O. Sboychakov, and S. V. Streltsov, “Spin–orbital interaction for face-sharing octahedra: Realization of a highly symmetric su(4) model,” *Physical Review B*, vol. 91, no. 15, p. 155125, 2015.

[104] E. Granado, A. García, J. A. Sanjurjo, C. Rettori, I. Torriani, F. Prado, R. D. Sánchez, A. Caneiro, and S. B. Oseroff, “Magnetic ordering effects in the raman spectra of la1-xmn1-xo3,” *Physical Review B*, vol. 60, no. 17, p. 11879, 1999.

[105] T. T. A. Lummen, I. P. Handayani, M. C. Donker, D. Fausti, G. Dhalenne, P. Berthet, A. Revcolevschi, and P. H. M. Van Loosdrecht, “Phonon and crystal field excitations in geometrically frustrated rare earth titanates,” *Physical Review B*, vol. 77, no. 21, p. 214310, 2008.

[106] N. Kolev, C. L. Chen, M. Gospodinov, R. P. Bontchev, V. N. Popov, A. P. Litvinchuk, M. V. Abrashev, V. G. Hadjiev, and M. N. Iliev, “Raman spectroscopy of caruo3,” *Physical Review B*, vol. 66, no. 1, p. 014101, 2002.

[107] M. N. Iliev, A. P. Litvinchuk, H. G. Lee, C. L. Chen, M. L. Dezaneti, C. W. Chu, V. G. Ivanov, M. V. Abrashev, and V. N. Popov, “Raman spectroscopy of srruo3 near the paramagnetic-to-ferromagnetic phase transition,” *Physical Review B*, vol. 59, no. 1, p. 364, 1999.

[108] H. L. Liu, S. Yoon, S. L. Cooper, G. Cao, and J. E. Crow, “Raman-scattering study of the charge and spin dynamics of the layered ruthenium oxide ca3ru2o7,” *Physical Review B*, vol. 60, no. 10, p. R6980, 1999.

[109] L. Jozwiak, J. Balcerzak, and J. Tyczkowski, “Plasma-deposited ru-based thin films for photoelectrochemical water splitting,” *Catalysts*, vol. 10, no. 3, p. 278, 2020.

[110] E. G. Sogut, H. Acidereli, E. Kuyuldar, Y. Karatas, M. Gulcan, and F. Sen, “Single-walled carbon nanotube supported pt-ru bimetallic superb nanocatalyst for the hydrogen generation from the methanolysis of methylamine-borane at mild conditions,” *Scientific reports*, vol. 9, no. 1, p. 15724, 2019.

[111] Z. Cao, C. Wang, Y. Sun, M. Liu, W. Li, J. Zhang, and Y. Fu, “A ru/ruo 2 heterostructure boosting electrochemistry-assisted selective benzoic acid hydrogenation,” *Chemical Science*, vol. 15, no. 4, pp. 1384–1392, 2024.

[112] X. Mao, Z. Liu, C. Lin, J. Li, and P. K. Shen, “Bimetallic ruthenium–nickel alloy nanostructure supported on nickel foam for efficient alkaline hydrogen evolution at large current density,” *Inorganic Chemistry Frontiers*, vol. 10, no. 2, pp. 558–566, 2023.

[113] S. A. Kimber, M. S. Senn, S. Fratini, H. Wu, A. H. Hill, P. Manuel, J. P. Attfield, D. N. Argyriou, and P. F. Henry, “Charge order at the frontier between the molecular and solid states in ba 3 naru 2 o 9,” *Physical Review Letters*, vol. 108, no. 21, p. 217205, 2012.

[114] S. V. Streltsov and D. I. Khomskii, “Orbital-dependent singlet dimers and orbital-selective peierls transitions in transition-metal compounds,” *Physical Review B*, vol. 89, no. 16, p. 161112, 2014.

[115] T. Basu, T. Zou, Z. Dun, C. Xu, C. Dela Cruz, T. Hong, H. Cao, K. Taddei, H. Zhou, and X. Ke, “Magnetic field induced phase transition in spinel geni 2 o 4,” *Physical Review B*, vol. 102, no. 13, p. 134421, 2020.

[116] A. Kumar, P. Manuel, and S. Nair, “Successive magnetic phase transitions with magnetoelastic and magnetodielectric coupling in the ordered triple perovskite sr 3 ca ru 2 o 9,” *Physical Review Materials*, vol. 8, no. 2, p. 024405, 2024.